

**Republic of Iraq
Ministry of Higher Education
and Scientific Research
University of Baghdad
College of Science**



**Microstructure and Optoelectronics
Characterizations of $Ga_xSb_{1-x}/GaAs$
Heterojunction**

A Thesis
Submitted to the College of Science
University of Baghdad
In Partial Fulfillment of the Requirements
for the Degree of Ph. D. in Physics

By
Ali Hussain Abdalrazzaq Jalaukhan
M.Sc.1991

Supervised by

Prof.Dr. Maysoon F.A. Alias
Asst. Prof.Dr. Hussein Kh. Al-Lamy

2012

1433

بِسْمِ اللَّهِ الرَّحْمَنِ الرَّحِيمِ

بِسْمِ اللَّهِ الرَّحْمَنِ الرَّحِيمِ

(قَالُوا سُبْحَانَكَ لَا عِلْمَ لَنَا إِلَّا مَا
عَلَّمْتَنَا إِنَّكَ أَنْتَ الْعَلِيمُ الْحَكِيمُ)


صدق الله العظيم

سورة البقرة (الآية 32)

بِسْمِ اللَّهِ الرَّحْمَنِ الرَّحِيمِ

Certification

We certify that we have read this thesis and as examination committee we examined the student (Ali Hussain Abdalrazzaq Jalaukhan) in its content and in our opinion it is adequate with standard as thesis for the degree of Doctor of Philosophy (Ph.D.) in Physics.

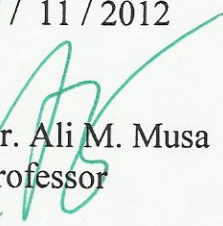
Signature: 

Name : Dr. Raad A. Radhi

Title : Professor

(Chairman)

Date : 14 / 11 / 2012

Signature: 

Name : Dr. Ali M. Musa

Title : Professor

(Member)

Date : 18 / 11 / 2012

Signature: 

Name : Dr. Fatima Y. Mohammed

Title : Asst. Professor

(Member)

Date : 20 / 11 / 2012

Signature: 

Name : Dr. Eman M. Nasir

Title : Asst. Professor

(Member)

Date : 14 / 11 / 2012

Signature: 

Name : Dr. Iqbal S. Naji

Title : Asst. Professor

(Member)

Date : 14 / 11 / 2012

Signature: 

Name : Dr. Maysoon F.A. Alias

Title: Professor

Address : Collège of Science

Date : 14 / 11 / 2012

Signature: 

Name: Dr. Hussain Kh. Al- Lamy

Title: Asst. Professor

Address : College of Science

Date : 14 / 11 / 2012

Approved by the University committee on graduate studies

Signature:

Name : Dr. Saleh M. Ali

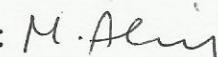
Title : Professor


Address: The Dean of College of Science/ University of Baghdad.

Date : / / 2012

Supervisors Certification

We certify that the preparation of this thesis was made under our supervision at the Department of Physics, College of Science in the University of Baghdad in partial fulfillment of the requirements for the degree of Doctor of Philosophy (Ph.D.) in Physics.

Signature : 
Name : Dr. Maysoon F.A. Alias
Title: Professor
Address : College of Science
Date : 14 / 11 / 2012

Signature : 
Name: Dr. Hussain Kh. Al- Lamy
Title: Asst. Professor
Address : College of Science
Date : 14 / 11 / 2012

In view of the available recommendation, I forward this thesis for debate by the examination committee.

Signature:


Name: Dr. Raad M. S. Al-Haddad

Title: Professor

Address: Chairman of the Dept. of Physics

Date: 14 / 11 / 2012

Acknowledgments

Praise is to Allah lord of the world, and best prayers and peace on his best messenger Mohammed, and his pure descendant.

I would like to express my deep thanks and gratitude to my supervisors Prof. Dr. Maysoon F. Alias and Asst. Prof. Dr. Hussein Kh. Al-lamy for their suggestion of this project and their encouragement through this work also for providing necessary facilities and help.

Thanks to the head and staff of the physics department Prof. Dr. Raad M. S. Al-haddad, for his assistance during this study.

I would like to thank some of the staff of thin film laboratory Dr. Issam M. Ibrahim and Dr. Kadhim A. Adem.

I would like to thank Mr. Ahmad Al-Shakery from geology department for his assistance (x-ray diffraction), Asst. Prof. Dr. Ahmed Aysh from department of physics University of Almirates Alain-UAE (D.C measurements), Prof. Dr. Rasul Ajian with the staff of thin film laboratory of faculty of physics University of Science and Technology Tehran for their assistance (I-V measurements), Prof. Dr. Mohajerzad with the staff of SEM laboratory(SEM micrographs) from faculty of electrical engineering, Mr. H. Sabaru from faculty of metallurgy engineering University of Tehran(EDXS), the staff of electronic library at the holly shrines of Al-Abbas and Imam Hussein peace upon them for their assistance (Internet), Ministry of Sciences and Technology Iraq for helping me in my work and my generous friends Abdulhussein Abbas, Salahaddeen Masur, Muhannad Mehdy, Emad Abdalrazzaq, Mohammed Ouda and Hyder Redha.

Finally, I must not forget to express my deep gratitude to my family who have stood by my side in every possible way and my thanks to all my friends.

To
My motherland IRAQ
My Family
My Teachers
and My Friends
for their Kindness,
Attention and encouragement.

Abstract

The stoichiometric amount of the alloys $\text{Ga}_x\text{Sb}_{1-x}$ with ($x=0.4, 0.5$ and 0.6) were sealed in quartz ampoule under pressure of 5×10^{-2} mbar. The ampoule containing the charge was placed in furnace at temperature of 1173 K for one hour. The $\text{Ga}_x\text{Sb}_{1-x}$ bulk and thin films have a zinc blend structure. $\text{Ga}_x\text{Sb}_{1-x}$ thin films have been prepared by depositing the alloys on soda lime glass substrate and (111) GaAs wafers the $\text{Ga}_x\text{Sb}_{1-x}$ films prepared at different temperatures (348, 398, 448 and 473K), thicknesses of (200, 300 and 400 nm) and x by using flash evaporation technique under pressure of about 10^{-5} mbar with deposition rate equal to 100 nm /min. The structure of $\text{Ga}_x\text{Sb}_{1-x}$ bulk and thin films were studied by x-ray diffraction analysis. Its found that they were polycrystalline and crystallizing as Zinc blend structure. The percentage of Ga and Sb in $\text{Ga}_x\text{Sb}_{1-x}$ alloys and films has been determined by using energy dispersive X-ray spectroscopy (EDXS).

The grain size and grain boundary of the $\text{Ga}_x\text{Sb}_{1-x}$ films have been measured by using the scanning electron microscope (SEM) micrographs. The grain size was increased with increasing of both film thickness and substrate temperatures. Also it was found that increase of the grain boundary when gallium concentration increased while the grain boundary decreased with increase of substrate temperatures for films $\text{Ga}_{0.4}\text{Sb}_{0.6}$ with thickness 200 nm whereas the grain boundary increased with increasing of substrate temperatures for films $\text{Ga}_{0.6}\text{Sb}_{0.4}$ with thickness 400 nm. This may be interpreted in term that Ga ratio which increase the liquid phase of $\text{Ga}_{0.6}\text{Sb}_{0.4}$.

The results of the electrical properties for $\text{Ga}_{0.5}\text{Sb}_{0.5}$ films deposited on glass at 400 nm thickness, showed that D.C conductivity at R.T increased from 1.5×10^{-3} to $5.3 \times 10^{-3} (\Omega \cdot \text{cm})^{-1}$ with increasing the substrate temperatures 348 to 473 K and increased from (6.9×10^{-5}) to $(8.7 \times 10^{-2}) (\Omega \cdot \text{cm})^{-1}$ with increasing of gallium percentage (0.4 – 0.6) at substrate temperature 348 K for $\text{Ga}_x\text{Sb}_{1-x}$ films deposited on glass at 200 nm thickness. We found two activation energies for D.C conductivity. The activation energy for $\text{Ga}_{0.5}\text{Sb}_{0.5}$ films deposited on glass at 400 nm thickness increased from 0.195 to 0.38 eV with increasing substrate temperature form 348 to 473 K. It decreased from 0.22 to 0.12 eV at 348 K and thickness 200 nm, with increasing of gallium percentage from (0.4-0.6). Thin films I-V measurements showed the Aluminum electrodes which deposited on $\text{Ga}_x\text{Sb}_{1-x}$ made ohmic contacts.

It was found that most of $\text{Ga}_{0.4}\text{Sb}_{0.6}$ films exhibited a negative Hall coefficient (n-type) while most of $\text{Ga}_{0.6}\text{Sb}_{0.4}$ films exhibited positive Hall coefficient (p-type). The carrier concentration (n_H) increased with increasing of substrate temperature for films

$\text{Ga}_x\text{Sb}_{1-x}$ with thickness 200 nm, while it decreasing for films with 400 nm and vice versa for mobility (μ).

The optical measurements indicated that $\text{Ga}_x\text{Sb}_{1-x}$ films have direct optical energy gap (E_g), and it increased with increasing of substrate temperatures (348– 473)K which is due to structure enhancement . It decreased with increasing of thickness (200 – 400) nm due to increasing of defects for all gallium percentages (0.4,0.5,0.6) respectively. The optical constants refractive index (n), extinction coefficient (k) and dielectric constants (ϵ_r and ϵ_i) were also studied.

The I-V and C-V calculations for $\text{Ga}_x\text{Sb}_{1-x}$ / GaAs Heterojunction were investigated. The current-voltage characteristics of $\text{Ga}_{0.6}\text{Sb}_{0.4}$ / GaAs heterojunction showed that the dark forward current varied approximately exponentially with applied voltage. The efficiency of prepared heterojunction was increased with increasing of T_s from 348 to 473K and it increased with increasing of thickness from 200 to 300 nm, then decreased with increasing thickness from 300 to 400nm.

The capacitance of $\text{Ga}_x\text{Sb}_{1-x}$ / GaAs heterojunction was measured as a function of the reverse bias voltage at 1 kHz. It was indicated that these junctions were abrupt. The values of built-in potential are increases with increasing of T_s and gallium percentage but it decreased with increasing of film thickness (t).

The values of identity factor of $\text{Ga}_{0.6}\text{Sb}_{0.4}$ / GaAs heterojunction decreased with increasing thickness from 200 to 300 nm whereas it increased with increasing thickness from 300 to 400nm.

List of Symbols and Abbreviations

α	Absorption Coefficient
β	Ideality Factor
τ	Carrier's Lifetime
ρ	Resistivity
σ	Electrical Conductivity
θ	Diffraction Angle
χ	Electron Affinity
λ	Wavelength
σ_0	Minimum Electrical Conductivity
$\sigma_{d.c}$	D.C. Conductivity
ΔE	Width of Localized Levels into Energy Gap
μ_H	Hall Mobility
ϵ_i	Imaginary Part of Dielectric Constant
ρ_m	Material Density
μ_n	Electron Mobility
μ_p	Hole Mobility
ϵ_r	Real Part of Dielectric Constant
ΔE_c	Discontinuity in the Conduction Band
ΔE_v	Discontinuity in the Valence Band
A	Absorbance
a_0	Lattice Constant
B	Magnetic Field
C	Capacitance
C.B	Conduction Band
C-V	Capacitance-Voltage
CVD	Chemical Vapor Deposition
CVE	Conventional Vacuum Evaporation
D	Diffusion Constant
DOS	Density of State
E	Electric Field
E_a	Electrical Activation Energy
E_c	Conduction Band Edge Energy
EDXS	Energy Dispersive X-ray Spectroscopy
E_f	Fermi level Energy
E_i	Ionization Energy
E_v	Valence Band Edge Energy
FTIR	Fourier Transform Infrared
h	Plank Constant
h ν	Photon Energy

ICs	Integrate Circuits
I_d	Dark Current
I_f	Forward Current
I_{ph}	Photocurrent
IR	Infrared
I_s	Saturation Current
I_{sc}	Short Circuit Current
J	Current Density
f	Lattice Mismatch
J_{ph}	Photocurrent Density
J_{sc}	Short-Circuit Current density
k	Extinction Coefficient
k_B	Boltzmann's Constant
l_1	Grain Size
l_2	Grain Boundary Width
LIC	Laser Interference Crystallization
LPCVD	Low-Pressure Chemical Vapor Deposition
m^*	Effective Mass of the Charge Carrier
MBE	Molecular Beam Epitaxy
MIR	Mid-infrared
MOCVD	Metalorganic Chemical Vapor Deposition
MOVPE	Metalorganic Vapor Phase Epitaxy
n	Electrons Concentration
n	Refractive Index
N_A	Acceptors Concentration
N_D	Donors Concentration
n_i	Intrinsic Carrier Concentration
NIR	Near-Infrared
p	Holes Concentration
P	Radiation Power
ϕ_b	Barrier Height
PV	photovoltaic
q	Charge of Electron
R	Reflectance
R_H	Hall Coefficient
RHEED	Reflection High-Energy Electron Diffraction
SEM	Scanning Electron Microscope
T	Transmission
t	Thickness
TEM	Transmission Electron Microscope
T_s	Substrate Temperature
UHV	Ultrahigh Vacuum
V_{bi}	Built-in Potential

v_d	Drift Velocity
V_f	Forward Voltage
V_H	Hall Voltage
V_{oc}	Open Circuit Voltage
V_R	Reverse Voltage
W_f	Work Function
XRD	X-Ray Diffraction

List of Contents

Contents	Page
Chapter One Theoretical Part	
1.1 Introduction	1
1.2 III-V Binary Compounds	5
1.3 Thin Film Growth Process	7
1.4 Thin Film preparation	10
1.4.1 Molecular Beam Epitaxy	10
1.4.2 Metalorganic Vapor Phase Epitaxy	12
1.4.3 Thermal Evaporation	14
1.5 Structural properties	15
1.5.1 Phase Diagram of Gallium – Antimony	15
1.5.2 GaSb Crystallization	15
1.6 Morphology, crystal structure and element composition characterizations	18
1.6.1 Scanning electron microscope	18
1.6.2 Energy dispersive X-ray spectroscopy	18
1.7 Band Diagrams of Heterostructures	19
1.8 The Electron Affinity Model	21
1.9 Electrical Properties of Semiconductors	23
1.9.1 D.C. Conductivity	23
1.9.2 Hall Effect	25
1.10 Optical properties	27
1.10.1 Fundamental Absorption Edge	27
1.10.2 Direct Transition	29
1.10.3 Indirect Transition	29
1.10.4 Optical constants	30
1.11 Literature Survey	31
1.12 The Aim of The Work	44
Chapter Two: Experimental Procedure and Measurements	
2.1 Introduction	45
2.2 GaSb Compound Preparation	47
2.3 Substrate Cleaning	48
2.4 Masks Preparation	48
2.5 Flash Evaporation Method	49
2.5.1 Evaporation Source	49
2.5.2 Substrate holder modification	50
2.6 Assembly Processes	52
2.7 Thickness Measurements	52
2.7.1 The Weighting Method	52
2.7.2 Scanning Electron Microscope Method	52

Contents	Page
2.8 Energy Dispersive X-Ray Measurements	53
2.9 X-Ray Diffraction	53
2.10 Electrical Measurements	53
2.10.1 The D.C Conductivity Measurement	54
2.10.2 Hall Effect Measurements	55
2.11 Optical Properties Measurements	55
2.11.1 Optical Energy Gap	56
2.11.2 Optical Constants	56
2.12 Electrical Properties of Ga _x Sb _{1-x} Films	56
2.12.1 Current-Voltage Measurements in the Dark	56
2.12.2 Capacitance-Voltage Measurements in the Dark	57
2.13 Photoelectric Measurements of Heterojunction	58
2.13.1 Current-Voltage Measurements under Illumination	58
2.13.2 The short Circuit Current and Open Circuit Voltage Measurements	58
Chapter Three: Results and Discussion	
3.1 Introduction	60
3.2 composition of Ga _x Sb _{1-x} alloys and Films	60
3.2.1 Energy Dispersive X-ray Spectroscopy analysis	60
3.3 Structural preparation of Ga _x Sb _{1-x} alloys and Films	63
3.3.1 X-ray diffraction analysis	63
3.3.2 SEM analysis	71
3.4 Electrical Properties of Ga _x Sb _{1-x} Films	75
3.4.1 Ohmic Contact	75
3.4.2 D.C Electrical Conductivity	75
3.5 Hall Effect	79
3.6 The Optical Properties	82
3.6.1 Transmittance Spectrum	83
3.6.2 The Absorption Coefficient	85
3.6.3 The Optical Energy Gap	87
3.6.4 Extinction Coefficient	89
3.6.5 Refractive Index	91
3.6.6 The Dielectric Constant	94
3.7 Electrical characteristics of Heterojunction	99
3.7.1 Current-Voltage Characteristics Measurements at Dark and illumination	99
3.8 Capacitance-Voltage Measurement	102
Chapter Four : Conclusions and Suggestions	109

Contents	Page
References	112

C h a p t e r O n e

Theoretical Part

1.1. Introduction

The physics of narrow band gap semiconductors is an important branch of semiconductors science. Research into this branch focuses on a specific class of semiconductor materials which have narrow forbidden band gaps. Historically, developments of narrow gap semiconductor physics have been closely related to the development of the science and technology of infrared optical electronics in which narrow gap semiconductors have played a vital role in detectors and emitters, and other high speed devices.

For the narrow band gap semiconductor materials, we need to know which kind of impurities and defects exist in the material, their chemical composition and electrical activity, whether they are p-type or n-type, the magnitude of the impurity concentration, the ionization energies of these defects, their impact on electrical and optical properties, how to experimentally observe their properties, and how to theoretically analyze their properties [1].

Antimony-based semiconducting materials are of great interest to the research and technology development communities for mid- and long-infrared applications. In particular, the antimony-based detector is a key component in advanced high-speed and low-noise optical receiver systems. In 2004, Herbert Kroemer, the Nobel laureate who pioneered the molecular beam epitaxy of antimonides in mid-1980's, expressed the vision about the emerging field of a new sub-family among the III–V compound semiconductors as follows: “The three semiconductors InAs, GaSb, and AlSb form an approximately lattice-matched set around 6.1\AA , at room temperature energy gaps ranging from 0.36 eV (InAs) to 1.61 eV (AlSb). Like other compound semiconductors, they are of interest principally for their heterostructures, especially heterostructures

combining InAs with the two antimonides and their alloys. This combination offers band lineups that are drastically different from those of the more widely studied AlAs, GaAs system, and the lineups are one of the principal reasons for interest in the 6.1Å family”. The 6.1Å family members are shown in Fig.1.1 with their associated bandgap and lattice constant with respect to other III–V semiconductors [2].

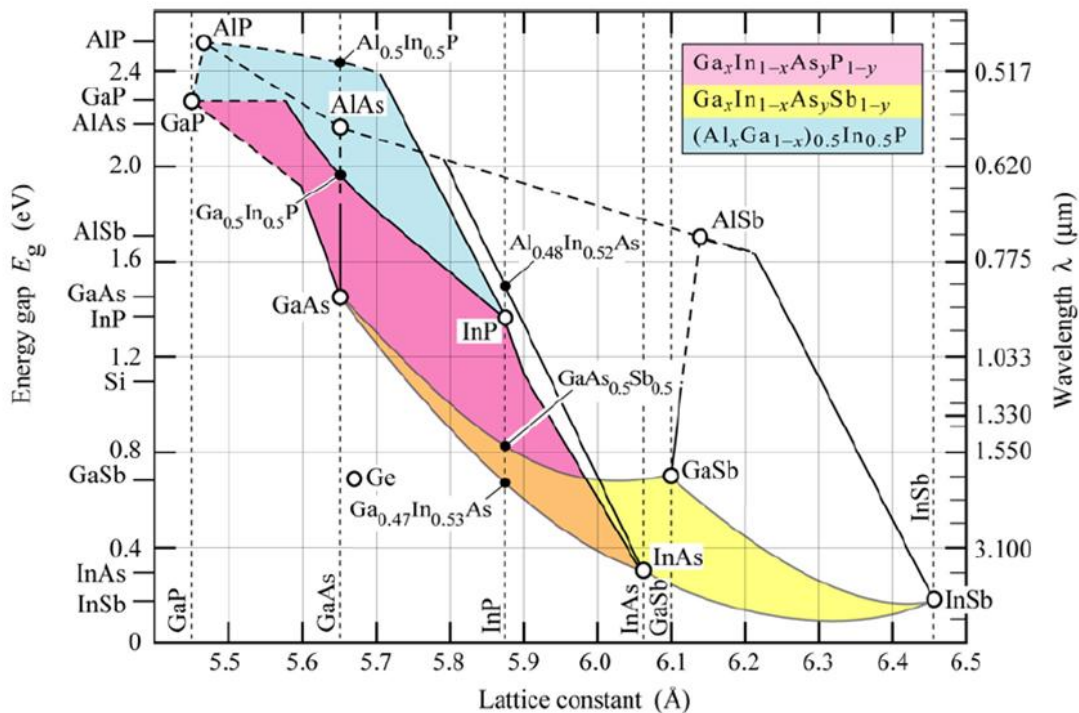


Fig. 1.1. Energy gap versus lattice constant at room temperature for various III-V semiconductors and their alloys. [2]

Antimony-based technology is very promising for low voltage millimeter-wave (mm-wave) integrated circuits (ICs), as well as very high-speed, low-power digital ICs. Among the many potential applications are digitally beam-steered phased array receivers, particularly those deployed in space; 80–160 Gbit/s optical communication systems; unmanned reconnaissance vehicles; and mobile, battery-powered systems. Powerful and easy-to-use lasers operating in the mid-infrared (MIR) range are important for

a variety of industrial and military applications, including IR countermeasures, light detection and ranging, remote trace-gas sensing, and secure free-space communications. [3]

Most of the references available [4-9] agree in attributing the origin of concept of generating electricity thermo photovoltaic to Pierre Aigrain, and place in decade of the 50's of the last century.

One of the most beneficial consequences of the energy crisis of 70's was undoubtedly the growth of global interest in renewable energy sources, led by photovoltaic solar energy. Therefore, during the 80's increased significant research projects in this field and returned to the interest by applications based this time in a more efficient use solar spectrum. This second phase began with the work of Bracewell and Swanson [10], followed by several researchers Demichelis, Swanson and Wurfel [11-13]. The above mentioned researchers explored the efficiency limits related to what is called the photovoltaics solar energy conversion. This approach is based on using concentrated solar radiation to heat a body, radiation reemitted absorbed with a more appropriate range, theoretically, to be converted photovoltaics. The correct choice of absorber / radiator, or use of spectral control elements would get only radiation with wavelengths wave near the semiconductor band gap, which can be converted by the latter of very efficiently. Thus, the reuse of the photons from the solar spectrum unsuitable energies can achieve efficiencies very close to theoretical system (the thermodynamic limit). However, the main drawback of this approach is practical source, because admitting the real limitations of the components of system efficiencies are lower. In addition to this approach, at this stage of the projects research focused on the development of other high-PV efficiency, also based on the use of a greater part of the spectrum available solar radiation. There was a growing interest in

cell manufacturing PV III-V semiconductors, especially GaAs, for their abilities to achieve conversion yields higher than silicon cells which developed spectral systems division concentrated solar radiation, whose beams were made falling on two solar cells of Si and GaAs. At the Institute of Solar Energy built a system based on this philosophy that efficiencies were achieved 29% [14]. Another group of workers bet by mechanical stacking of these cells, by which achieved efficiencies of 31% [15].

In this line, one of the most critical to the resurgence of third thermophotovoltaics stage techniques was undoubtedly that undertaken by the department Engineering and Research of the U.S. company Boeing, which later the 80's were designed and fabricated GaSb photovoltaic cells, using broadcasts Zn in n-type substrates, for use in mechanical stacks of GaAs cells [16]. GaSb devices fabricated showed good quantum efficiencies, low dark currents and high performance under concentrated light. These good results obtained in a semiconductor device III-V low width forbidden band enabled the resurgence of systems and applications thermophotovoltaic in the 1990's. This renewed interest was led by National Renewable Energy Laboratory, U.S. (NREL), which since 1994-1998 stimulated research in this field by organizing a series of four monographic lectures on thermophotovoltaic generation of electricity. Thus, in last decade a significant progress in all fields thermophotovoltaic specific techniques: radiators have been developed optimized spectral characteristics, spectral control elements based on diverse approaches and photovoltaic devices III-V semiconductors ternary and quaternary, with widths smaller band gap.

1.2 III-V Binary Compounds

Binary compounds are formed by the chemical combination of an element from column IIIA of the periodic Table and an element from column VA. In these compounds, each atom from column III is tetrahedrally bonded in a zincblende structure to four atoms from column V, and vice-versa. When considering III-V compounds, it should be noted that the binding energy of the orbital electrons shrinks as we form progressively heavier materials by descending column III or column V of the periodic Table. The reduced binding energy for the heavier materials is reflected by a shrinkage of the energy bandgap, E_g , as illustrated by the values for AlP (2.45 eV), GaP (2.26 eV), and InP (1.35 eV) or by the values for AlP (2.45 eV), AlAs (2.16 eV), and AlSb (1.65 eV). The same trend exists for the melting temperature of the compounds as shown in Table (1.1) since binding energies play a strong role in this process as well [17].

Table (1.1) Properties of some III-V semiconductors [17].

	a_0 Å Lattice constant	T_m (°C) Melting point	E_g (eV) Energy gap	λ_c (μm) Operating wavelength	Band structure
AlP	5.463	>2000	2.45	0.51	Indirect
AlAs	5.661	1740	2.16	0.57	Indirect
AlSb	6.138	1050	1.65	0.75	Indirect
GaP	5.449	1467	2.26	0.55	Indirect
GaAs	5.653	1238	1.42	0.87	Direct
GaSb	6.095	706	0.72	1.85	Direct
InP	5.868	1058	1.35	0.92	Direct
InAs	6.058	942	0.36	3.44	Direct
InSb	6.479	530	0.17	7.33	Direct

The main point of our discussion, however, is that the selection of elements from these two columns of the periodic table provides a spectrum of energy bandgap values between 0.17 eV (for InSb) and 2.45 eV (for AlP) at room temperature. Since optoelectronic devices rely on bandgap processes (emission for electroluminescent sources, absorption for optical detectors), the operating wavelength ($\lambda = 1.24/E_g$) of devices formed from the nine compounds of Table 1.1 have discrete values between 0.51 μm (for AlP) and 7.3 μm (for InSb) [17]. Table (1.2) shows some physical properties of GaSb and GaAs.

Table (1.2) Some physical properties of GaSb and GaAs [18].

Parameter	GaSb	GaAs
Crystal structure	Zinc Blend	Zinc Blend
Lattice constant (Å)	6.0959	5.653
Number of atoms per cm^3	$3.53 \cdot 10^{22}$	$4.42 \cdot 10^{22}$
Density (g. cm^{-3})	5.6137	5.32
Electron affinity (eV)	4.06	4.07
Optical Energy gap (eV)	0.725	1.424
Index of Refraction	3.82	3.3
Melting Temperature ($^{\circ}\text{C}$)	711.85	1240
Thermal Expansion at 300K	$7.75 \cdot 10^{-6} (^{\circ}\text{C}^{-1})$	$5.73 \cdot 10^{-6} (^{\circ}\text{C}^{-1})$
Dielectric constant	15.69	13.18
Mobility holes ($\text{cm}^2 \text{V}^{-1} \text{s}^{-1}$)	≤ 1000	≤ 400
Mobility electrons ($\text{cm}^2 \text{V}^{-1} \text{s}^{-1}$)	≤ 3000	≤ 8500
Thermal conductivity at 300K	$0.39 (\text{W.cm}^{-1}. ^{\circ}\text{C}^{-1})$	$0.55 (\text{W.cm}^{-1}. ^{\circ}\text{C}^{-1})$
Intrinsic Resistivity ($\Omega \cdot \text{cm}$)	10^3	$3.3 \cdot 10^8$

1.3 Thin Film Growth Process

Any thin-film deposition process involves three main steps:

1. Production of the appropriate atomic, molecular, or ionic species.
2. Transport of these species to the substrate through a medium.
3. Condensation on the substrate, either directly or via a chemical and/or electrochemical reaction, to form a solid deposit.

Formation of a thin film takes place via nucleation and growth processes.

The general picture of the step-by-step growth process emerging from the various experimental and theoretical studies can be presented as follows:

1. The unit species, on impacting the substrate, lose their velocity component normal to the substrate (provided the incident energy is not too high) and are physically adsorbed on the substrate surface.
2. The adsorbed species are not in thermal equilibrium with the substrate initially and move over the substrate surface. In this process they interact among themselves, forming bigger clusters.
3. The clusters or the *nuclei*, as they are called, are thermodynamically unstable and may tend to be desorbed in time, depending on the deposition parameters. If the deposition parameters are such that a cluster collides with other adsorbed species before getting desorbed, it starts growing in size. After reaching a certain critical size, the cluster becomes thermodynamically stable and the *nucleation barrier* is said to have been overcome. This step involving the formation of stable, chemisorbed, critical-sized nuclei is called the *nucleation stage*.
4. The critical nuclei grow in number as well as in size until a saturation nucleation density is reached. The nucleation density and the average nucleus size depend on a number of parameters such as the energy of the impinging

species, the rate of impingement, the activation energies of adsorption, desorption, thermal diffusion, and the temperature, topography, and chemical nature of the substrate.

A nucleus can grow both parallel to the substrate by surface diffusion of the adsorbed species, and perpendicular to it by direct impingement of the incident species. In general, however, the rate of lateral growth at this stage is much higher than the perpendicular growth. The grown nuclei are called *islands*.

5. The next stage in the process of film formation is the *coalescence stage*, in which the small islands start coalescing with each other in an attempt to reduce the substrate surface area. This tendency to form bigger islands is termed *agglomeration* and is enhanced by increasing the surface mobility of the adsorbed species, by, for example, increasing the substrate temperature. In some cases, formation of new nuclei may occur on areas freshly exposed as a consequence of coalescence.

6. Larger islands grow together, leaving channels and holes of uncovered substrate. The structure of the films at this stage changes from discontinuous island type to porous network type. Filling of the channels and holes forms a completely continuous film.

The growth process thus may be summarized as consisting of a statistical process of nucleation, surface-diffusion controlled growth of the three-dimensional nuclei, and formation of a network structure and its subsequent filling to give a continuous film. Depending on the thermodynamic parameters of the deposit and the substrate surface, the initial nucleation and growth stages may be described as (a) island type, called Volmer-Weber type, (b) layer type, called Frank-van der Merwe type, and (c) mixed type, called

Stranski-Krastanov type. This is illustrated in Fig. (1.2). In almost all practical cases, the growth takes place by island formation.

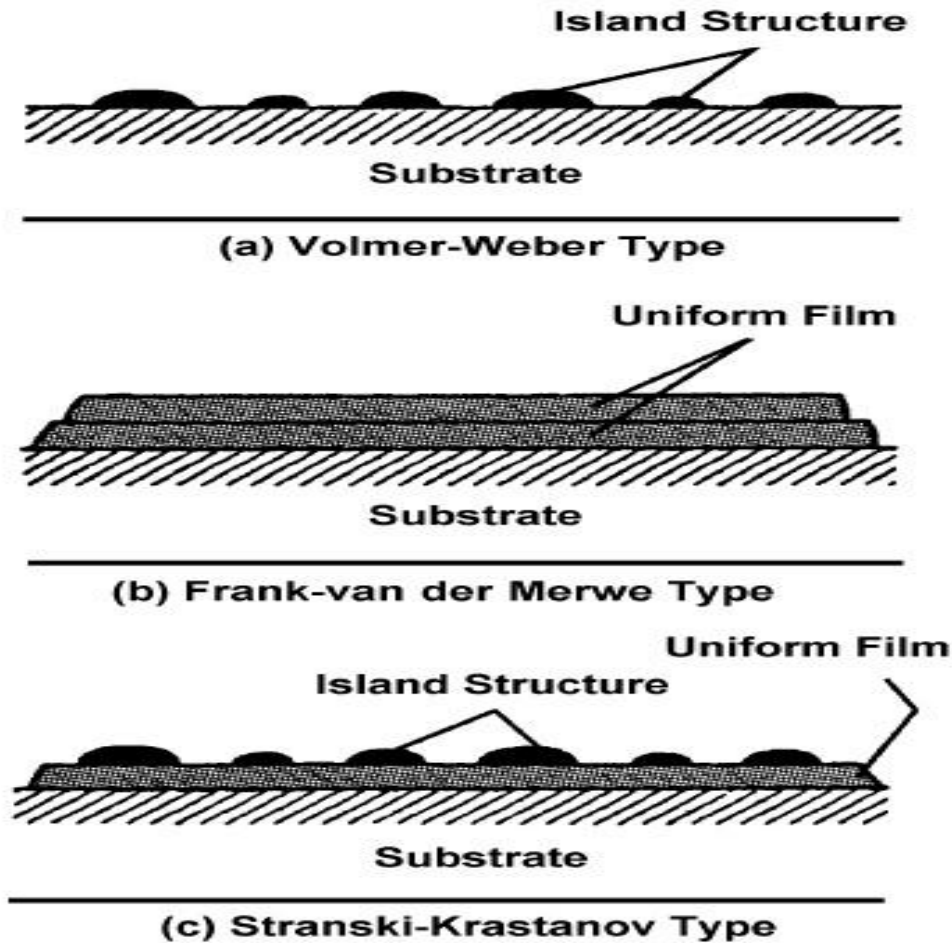


Fig.(1.2) Three modes of thin film growth processes [19].

Except under special conditions, the crystallographic orientations and the topographical details of different islands are randomly distributed, so that when they touch each other during growth, grain boundaries and various point and line defects are incorporated into the film due to mismatch of geometrical configurations and crystallographic orientations. If the grains are randomly oriented, the films show a ring-type diffraction pattern and are said to be polycrystalline. However, if the grain size is small 20 \AA , the films show halo-

type diffraction patterns similar to those exhibited by highly disordered or amorphous (noncrystalline) structures. Even if the orientation of different islands is the same throughout, as obtained under special deposition conditions (described above) on suitable single-crystal substrates, a single-crystal film is not obtained. Instead, the film consists of single-crystal grains oriented parallel to each other and connected by low-angle grain boundaries. These films show diffraction patterns similar to those of single crystals and are called epitaxial single-crystal films [19].

1.4 Thin Film Preparation

1.4.1 Molecular Beam Epitaxy (MBE)

This growth method is schematically shown in Fig. 1.3 The whole setup is situated within an ultrahigh vacuum (UHV) chamber serving as growth reactor. Within this reactor, the mounted sample substrate can be heated to the desired growth temperature. All growth components are evaporated from individually heatable effusion cells which are placed adjacent to the sample surface. Thus, the partial pressures of the different materials, which determine the chemical nature of the epitaxial film and the growth rate, are given by the geometry and the temperature of the effusion cells. For exact conditions and for enabling a fast change of the deposited material in heteroepitaxy, the effusion cells are equipped with shutters.

In many MBE reactors, the partial pressures can directly be measured by a mass spectrometer or an ion gauge in the beam, the growth rate can be controlled by a quartz-crystal oscillator [20].

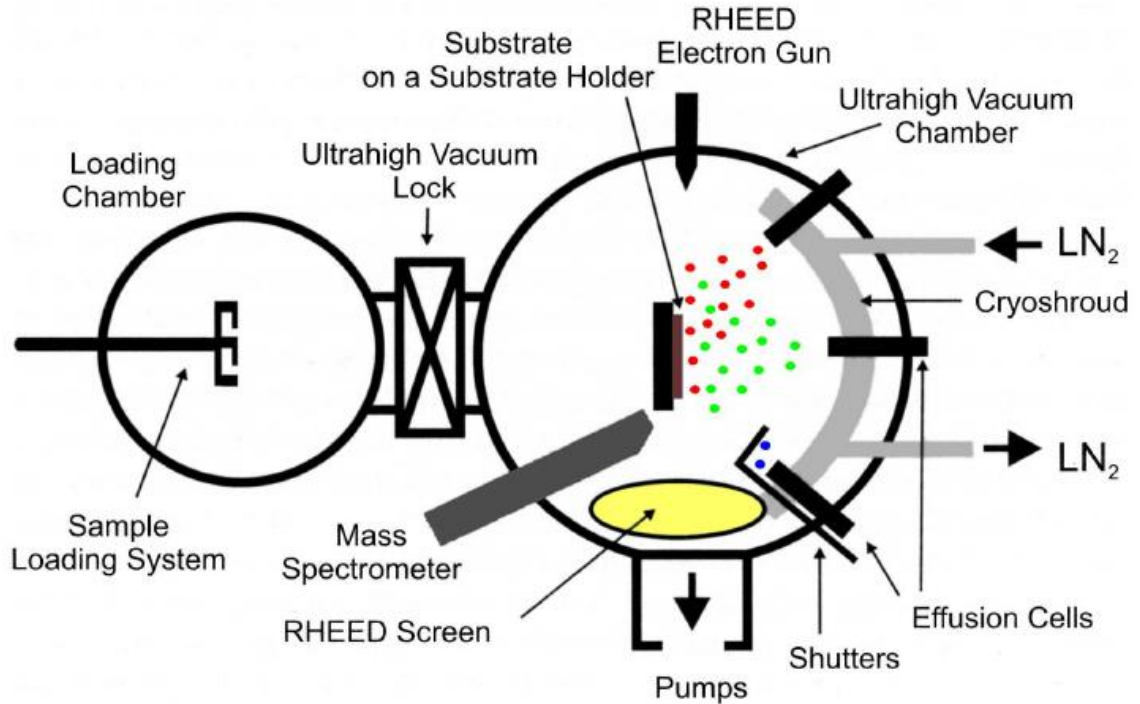


Fig. (1.3) Schematic diagram of an MBE setup [20].

The surface structure of the evolving epitaxial layer can in situ be monitored by reflection high energy electron diffraction (RHEED), which shows the geometry of the surface reconstruction in reciprocal space, characterized by specific spots. The layer by layer growth of a semiconductor film results in an oscillating surface roughness and therewith an oscillating RHEED signal e.g. of the specular reflex, allowing to count the deposited atomic layers directly. The growth of III-V semiconductors can be controlled by the flux of the group-III atoms. Because the group-V atoms cannot stick on the substrate surface without the presence of group-III atoms, they are typically offered abundantly in the reactor, while the group-III flux governs the growth rate. The ratio of group-V to group-III atoms (often called V/III ratio which should be much larger than one) and the substrate temperature determine which kind of possible surface reconstructions appears. Therefore it

is much easier to change the group-III element during growth, like switching from GaAs to InAs, than the group-V element, like changing between GaAs and GaSb. In the latter case, As and Sb atoms form a permanent background within the reactor which needs some time to decline and which can influence the stability and stoichiometry of the growth surface [21].

1.4.2 Metalorganic Vapor Phase Epitaxy (MOVPE)

It is also known as MOCVD (metalorganic chemical vapor deposition), is a chemical vapour deposition method for epitaxial growth of materials, especially compound semiconductors from the surface reaction of organic compounds or metalorganics and hydrides containing the required chemical elements. In the MOVPE process the source materials are mixed with a carrier gas and transported into a reactor where the substrate is located on a heated susceptor. When the metalorganic precursor molecules decompose in the hot zone over the substrate, the group III and V elements diffuse to the surface of the substrate. After the atoms are adsorbed to the surface, they can diffuse on the surface, nucleate into the growing epilayer or desorb away. The most attractive features of the MOVPE method are the wide range of metalorganic compounds available as precursors and facility of fabricating highly homogeneous layers, atomically at surfaces, and sharp material interfaces while controlling the composition precisely.

All the group-III and group-V source materials are metalorganic compounds. Trimethylindium (TMIn), trimethylgallium (TMGa), tertiarybutylarsine (TBAs), tertiarybutylphosphine (TBP) and dimethylhydrazine (DMHy) are used as sources of indium, gallium, arsenic, phosphorus and nitrogen, respectively. The source materials are held in steel bubblers and kept in temperature-controlled baths. Hydrogen is used as the

carrier gas. When the carrier gas flows through the bubblers, it is saturated with the vaporized source material molecules. The concentration of the precursor in the gas is determined by the vapor pressure of the compound at the bath temperature. The flow rate is controlled by mass flow controllers. The saturated flow from each bubbler is directed either to the vent line or to the mixing manifolds which lead to the reactor. Separate mixing manifolds are used for group-III and group-V precursors to prevent unwanted pre-reactions before the reactor. The vent line is used for stabilizing the flow rates and the concentrations before the epitaxial growth and to flush the residual materials after the growth. The gas flows from the reactor and the vent line are directed to the exhaust where the toxic particles are absorbed and oxidized in a gas scrubber [22].

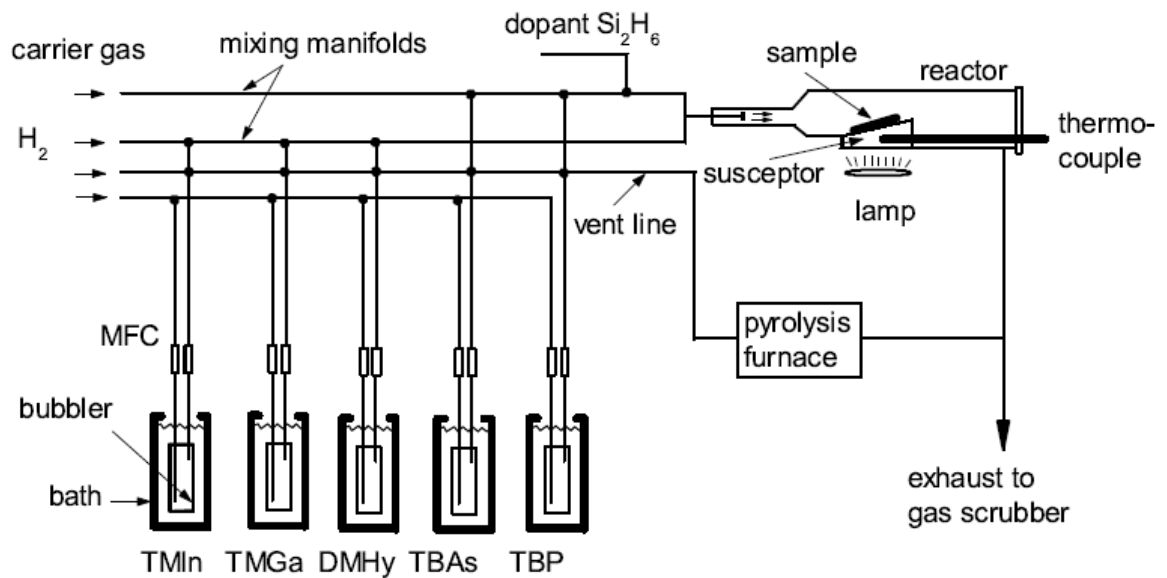


Fig.(1.4) Schematic diagram of the MOVPE system [22].

1.4.3 Thermal Evaporation.

The thermal evaporation process comprises evaporating source materials in a vacuum chamber below 1×10^{-6} torr (1.3×10^{-4} Pa) and condensing the evaporated particles on a substrate.

The thermal evaporation process is conventionally called *vacuum deposition*. Two types of thermal evaporation processes are shown in Fig. (1.5).

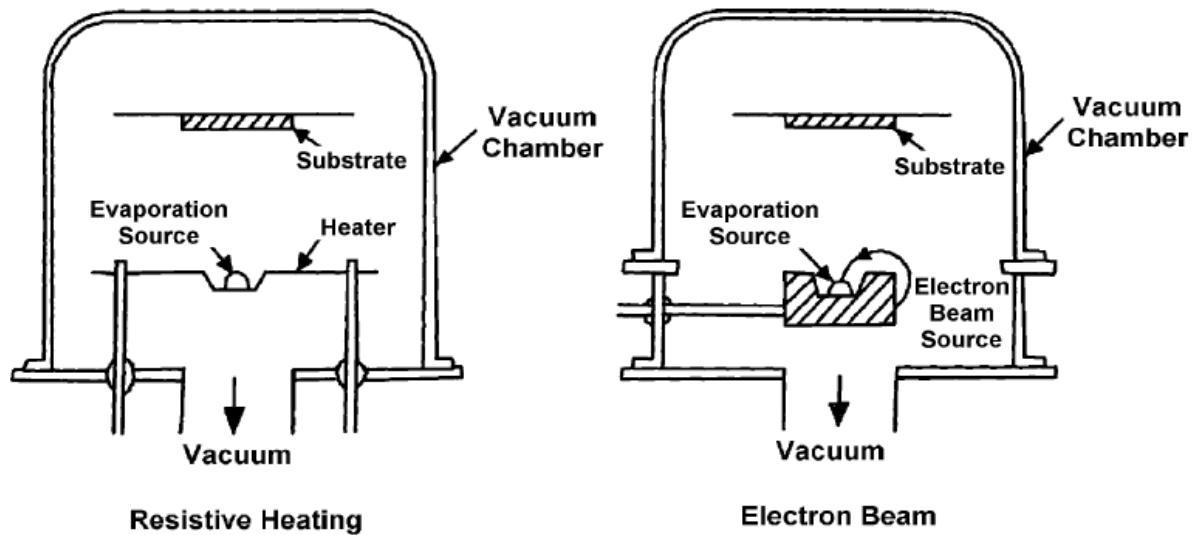


Fig. (1.5) Thermal evaporation process [19].

Resistive heating is most commonly used for the deposition of thin films. The source materials are evaporated by a resistively heated filament or boat, generally made of refractory metals such as Tungsten, Molybdenum, or Tantalum, with or without ceramic coatings. Crucibles of quartz, graphite, alumina, beryllia, boronnitride, or zirconia are used with indirect heating. The refractory metals are evaporated by electron-beam deposition since simple resistive heating cannot evaporate high melting point materials [19].

1.5 Structural Properties

1.5.1 Phase Diagram of Gallium – Antimony

GaSb was prepared from the phase diagram of Ga-Sb to obtain a cubic zinc blend type structure, with $a = 6.105 \text{ \AA}$ as shown in Fig.(1.6) phase diagram of Ga-Sb.

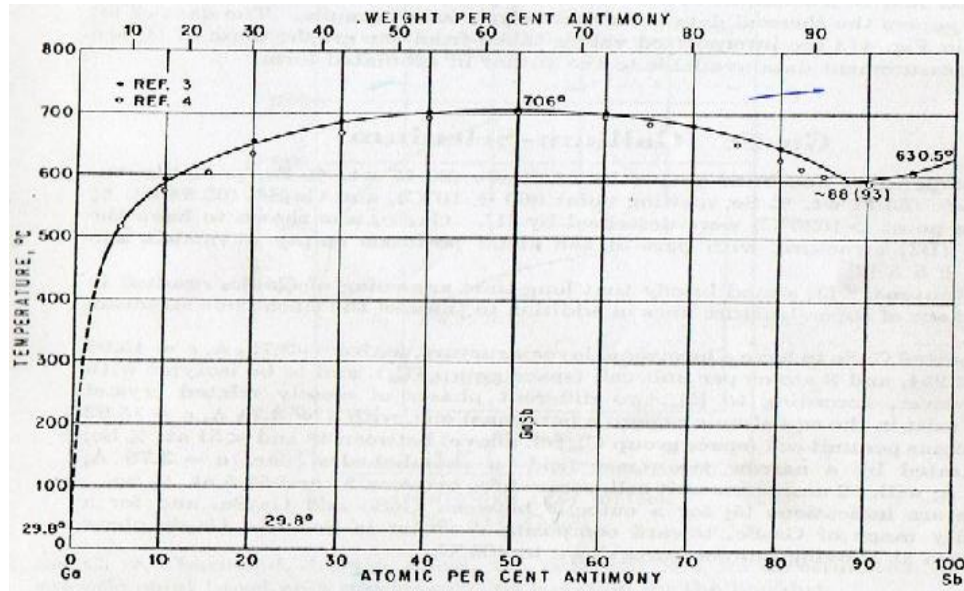


Fig.(1.6) Phase diagram of Gallium – Antimony [23]

1.5.2 GaSb Crystallization

Diffraction patterns provide structural details related to the specimen's orientation, polytype, phase, and defect morphology. Diffraction pattern analysis is an excellent complement to x-ray diffraction data. Many semiconductor materials form in the zinc blend crystal structure, as shown in Fig.(1.7). This structure consists of two interpenetrating face-centered cubic (Fcc) lattices displaced by $1/4$ of the length of the unit cell's diagonal. In a binary AB alloy (such as GaAs), all of the A atoms will lie on one of the fcc lattices, while all of the B atoms lie on the second Fcc lattice. Si has the diamond crystal structure, which is identical to the zinc blend structure with the exception that each atomic site is populated by the same atom such as

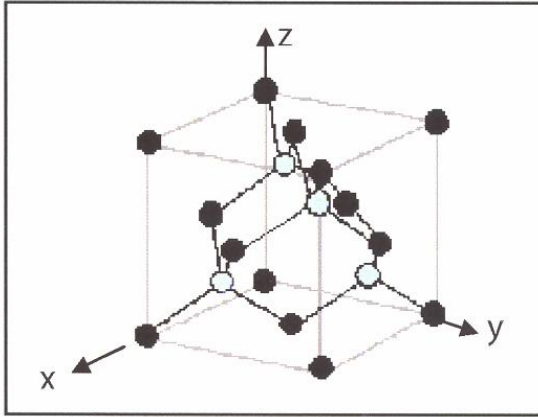


Fig.(1.7) Schematic of the zinc blende crystal structure in real space[24].

arsenides, have also been of physical interest because of the unconventional type-II and type-III band alignment [25]. It has been widely known that polycrystalline materials are composed of small crystallites joined together at grain boundaries. At the grain boundaries between the crystallites, there exist a substantial number of traps that pin the surface Fermi level and greatly influence the bulk conductivity [26,27]. It has been found that p-type GaSb's surface Fermi-level is pinned in the valence band. As shown in Fig.(1.8), this Fermi level pinning causes a band-bending barrier on the grain boundaries of p-type poly-GaSb much lower than that on the grain boundaries of p-type poly-GaAs, which has the surface Fermi-level pinned in the mid-bandgap. Similarly, the grain boundary barrier of p-type poly-GaSb will also be lower than p-type poly-InAs, which has the surface Fermi level pinned above the conduction band. For these reasons, the conduction between grains in poly-GaSb is much less limited and lower bulk resistivity is more likely to be achieved [28].

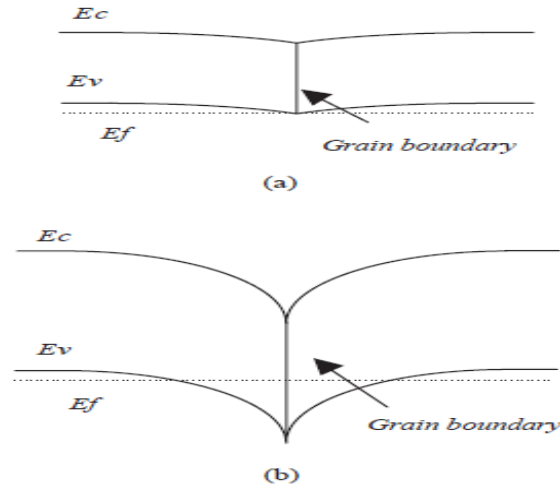


Fig. (1.8) Schematic diagrams of suggested energy band structure near grain boundaries in p-type of (a) GaSb and (b) GaAs[28].

The grain boundaries have an inherent space charge region due to the interface. Band bending occurs, and potential barriers to the charge transport result. This situation is represented schematically for *n*-type semiconductor in Fig.(1.9). One of the earliest models accounting for the conductivity in polycrystalline semiconductor film was that of Volger [30].

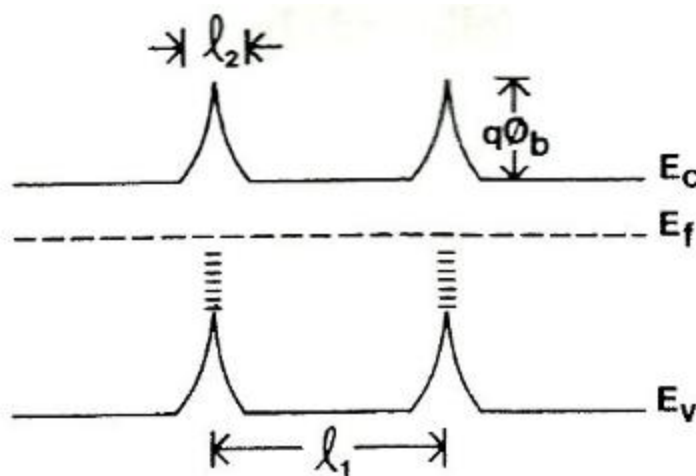


Fig.(1.9) Energy band representation of an *n*-type polycrystalline semiconductor thin film with grain size l_1 and grain boundary width l_2 . Grain boundary barrier potential is $q\Phi_b$ [29].

Thus, he simulates a polycrystalline semiconductor in which ohmic transport of the carriers dominates. Defining l_1 as the grain size and l_2 as the boundary width showing that:

$$\mu_g = \mu_1 \{ [1 + (l_2 / l_1) \exp(q\Phi_b / kT)]^{-1} + (l_2 / l_1) \} \dots \dots \dots (1.1)$$

where μ_g is the effective mobility, μ_1 is the bulk grain mobility and Φ_b is a barrier potential relating to the concentration in the grain and boundary domains [29].

1.6 Morphology, Crystal Structure and Element Composition Characterizations

1.6.1 Scanning Electron Microscope (SEM)

SEM is a type of electron microscope that images the sample surface by scanning it with a high-energy electron beam. When the electrons interact with the atoms of a sample, they will produce a series of signals that contain information about surface topography and composition of the sample. These signals include secondary electrons, back scattered electrons, transmitted electrons, characteristic x-rays, cathodoluminescence and electron-beam-induced current. They can be used to modulate the monitor intensity, build up a two-dimensional map of the near-surface topography, and analyze element composition and electrical conductivity. In the standard detection mode, SEM can produce high-resolution images of the sample surface using secondary electron imaging. This make it an outstanding tool to observe the performance of potentially problematic samples, such as wet, oil, dirty, out gassing and non-conductive samples, without significant sample preparation.

1.6.2 Energy dispersive X-ray spectroscopy (EDXS)

EDXS is a stable, compact and robust element analysis instrument and it is very easy to use and interpret. The typical EDXS spectra are plots of X-ray counts versus X-ray energy. The principle scheme of EDXS is shown in Fig. (1.10). When electrons penetrate through outer electron shells and interact

with the core electrons, two kinds of X-rays are generated. One is characteristic X-ray caused by the ionization of atoms and the other is the continuous Bremsstrahlung X-ray produced by the interaction of high-energy electrons and nucleus. In the ionization process, an inner-shell (or core) electron is ejected from the atoms by the high-energy electron and a hole is left behind. Then an outer-shell electron will fill in this hole and emit an X-ray that has unique energy related to the ionized atom. Hence, the obtained EDXS spectrum is the characteristic X-rays with Gaussian-shaped peaks superimposed on the Bremsstrahlung X-rays background [21].

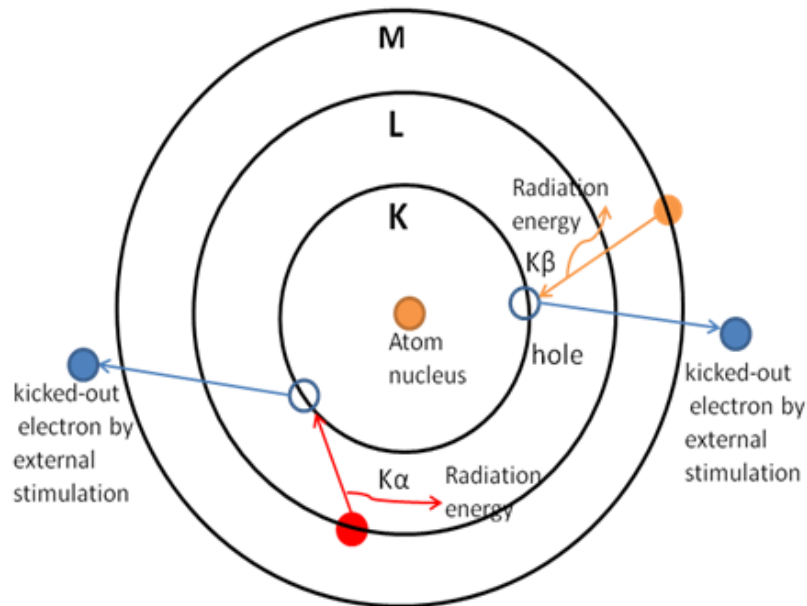


Fig.(1.10) Atomic energy level diagram for characteristic x-ray signal generation in EDXS [21].

1.7 Band Diagrams of Heterostructures

In a semiconductor heterostructure, two different semiconductors are brought into physical contact (distance between the two surfaces equal to the lattice constant of one of them). In practice, different semiconductors are “brought into contact” by epitaxially growing one semiconductor on top of

another semiconductor. Heterostructures were classified according to the alignment of the bands of the two semiconductors. Three different alignments of the conduction and valence bands and of the forbidden gap are shown in Fig. (1.11a) shows the most common alignment which will be referred to as the straddled alignment or “Type I” alignment. The most widely studied heterostructure, that is the GaAs / $\text{Al}_x\text{Ga}_{1-x}$. As heterostructure, exhibits this straddled band alignment. Fig. (1.11b) shows the staggered lineup. In this alignment, the steps in the valence and conduction band go in the same direction. The staggered band alignment occurs for a wide composition range in the $\text{Ga}_x\text{In}_{1-x}$ As / $\text{GaAs}_y\text{Sb}_{1-y}$ material system. The most extreme band alignment is the broken gap alignment shown in Fig. (1.11c); this alignment occurs in the InAs / GaSb material system. Both the staggered lineup and the broken-gap alignment are called “Type II” energy band alignments.

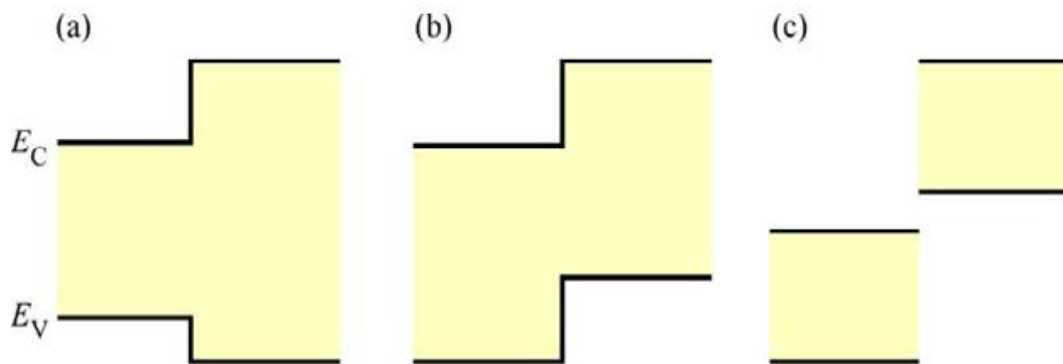


Fig.(1.11) Types of energy band lineups: (a)straddled or “ Type I “ lineup, (b) staggered or : “ Type II “ lineup, and (c) broken or “ Type II “ lineup [2] .

At the semiconductor interface of the heterostructure, the energies of the conduction and valence band edges change. The magnitudes of the changes in the band-edge energies are critically important for many semiconductor devices.

1.8 The Electron Affinity Model

The electron affinity model is the oldest model invoked to calculate the band offsets in semiconductor heterostructures. This model has proven to give accurate predictions for the band offsets in several semiconductor heterostructures, whereas the model fails for others. The basic idea of the electron affinity model is illustrated in Fig. (1.12).

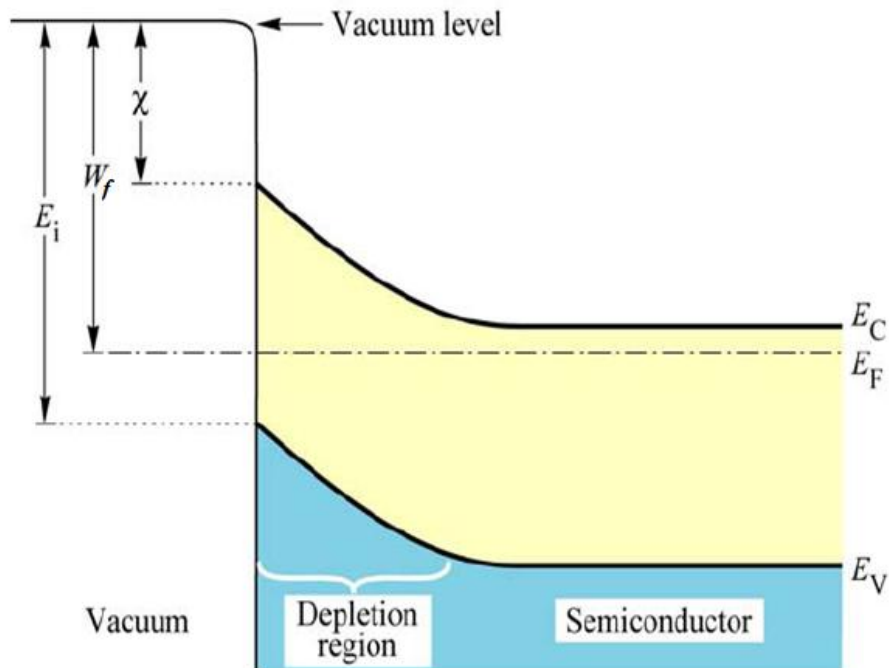


Fig. (1.12) Electron affinity χ , work function W_f and ionization energy E_i of a semiconductor. The electron affinity is measured from the bottom of the conduction band at the semiconductor surface, the work function from the Fermi level, and the ionization energy from the top of the valence band at the surface [2].

The band diagram of a semiconductor-vacuum interface is shown in Fig.(1.12). Near the surface, the n-type semiconductor is depleted of free electrons due to the pinning of the Fermi level near the middle of the forbidden gap at the semiconductor surface. Such a pinning of the Fermi level at the surface occurs for most semiconductors. The energy required to move

an electron from the semiconductor to the vacuum surrounding the semiconductor depends on the initial energy of the electron in the semiconductor. Promoting an electron from the bottom of the conduction band to the vacuum beyond the reach of image forces requires work called the electron affinity (χ). Lifting an electron from the Fermi level requires work called the work function W_f which is defined the same way in semiconductors as it is in metals. Finally, raising an electron from the top of the valence band requires the ionization energy E_i . This energy is measured by photoionization experiments, in which semiconductors are illuminated by monochromatic light with a variable wavelength. The longest wavelength at which photoionization occurs defines the ionization energy [2]. Consider that two semiconductors are brought into physical contact. The two semiconductors are assumed to have an electron affinity of χ_1 and χ_2 and a bandgap energy of E_{g1} and E_{g2} , respectively, as illustrated in Fig. 1.13. Near-surface band bending and the effect of image forces have been neglected in the figure. The electron affinity model is based on the fact that the energy balance of an electron moved from the vacuum level to semiconductor “1”, from there to semiconductor “2”, and from there again to the vacuum level must be zero, that is:

$$\chi_1 - \Delta E_C - \chi_2 = 0 \quad \dots\dots\dots (1.2)$$

or

$$\Delta E_C = \chi_1 - \chi_2$$

The valence band discontinuity then follows automatically as:

$$\Delta E_V = E_{g2} - E_{g1} - \Delta E_C \quad \dots\dots\dots (1.3)$$

Note that Eqs. (1.2) and (1.3) are valid only if the potential steps caused by atomic dipoles at the semiconductor surfaces and the heterostructure interfaces can be neglected. In this case, the knowledge of the electron affinities of two semiconductors provides the band offsets between these two

semiconductors as shown in Fig.(1.13). Shay *et al.* [31] report that the influence of dipole layers at semiconductor surfaces change the values of the electron affinity by about only 1%. Therefore, they argued, the electron affinity rule is indeed applicable to semiconductor heterostructures.

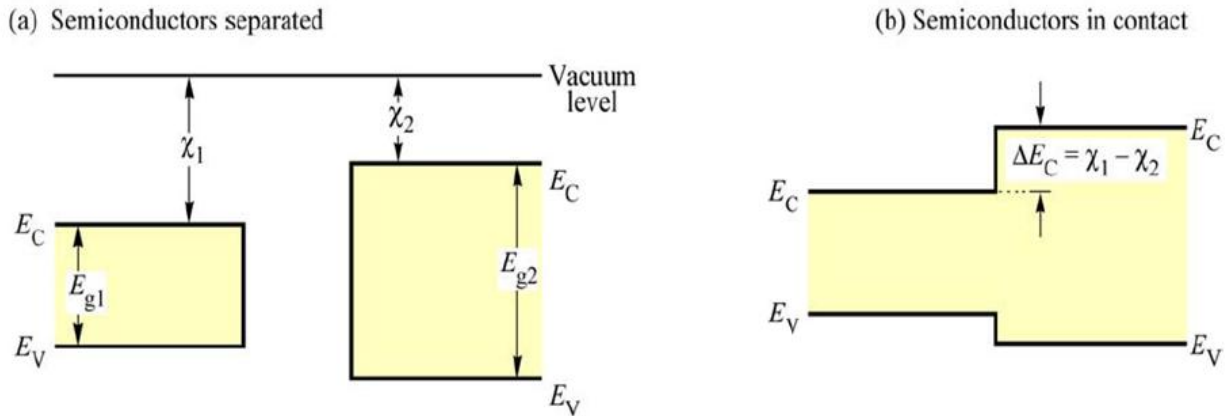


Fig.(1.13) Band diagram of (a) two separated semiconductors and (b) two semiconductors in contact .The semiconductors have band gap energy of E_{g1} and E_{g2} and electron affinity of χ_1 and χ_2 .

1.9 Electrical Properties of Semiconductors

1.9.1 D. C. Conductivity

The D.C. conductivity in crystalline semiconductors depends on the presence of free electrons and free positive holes. At zero Kelvin, the valence band is regarded as filled and the conduction band is empty. As the temperature is raised bonds are broken and the effect is that free electrons are excited into the conduction band, and this leaves behind holes in valence band [32]. The electrical conductivity (σ) is given by Ohm's law

$$J = \sigma E \dots\dots\dots (1.4)$$

where:

J: is the current density.

E: is the electric field.

$$\sigma = nq\mu \dots\dots\dots (1.5)$$

or

$$\sigma = (nq^2\tau)/m^* \dots\dots\dots (1.6)$$

where

μ : is the mobility,

τ : is the carrier's lifetime,

n : is the carrier's concentration,

m^* : is the effective mass of the carrier, and

q : is the electron charge

In semiconductors, the relation between the current density and electric field is given by:

$$J = q(n\mu_n + p\mu_p) E \dots\dots\dots (1.7)$$

where

n & p are the electron and hole concentration and μ_n & μ_p are the mobility of electron and hole, respectively,

$$\mu = \frac{V_d}{E} \dots\dots\dots (1.8)$$

where

V_d is the drift velocity. So that we have

$$\sigma = q(n\mu_n + p\mu_p) \dots\dots\dots (1.9)$$

This important relationship is connecting the conductivity with the electron and hole concentrations and mobilities [33].

The change of electrical conductivity with temperature for most cases of intrinsic semiconductors are given by:

$$\sigma = \sigma_0 \exp (-E_a/k_B T) \dots\dots\dots (1.10)$$

where:

E_a : is the thermal activation energy

T: is the absolute temperature

k_B : is the Boltzmann constant

σ_0 : is the minimum electrical conductivity at zero Kelvin.

Indeed for intrinsic semiconductor $2E_a = E_g$, where the Fermi energy is centered at the middle of the gap, and equation above can be written as [34].

$$\sigma = \sigma_0 \exp (-E_g/ 2k_B T) \dots \dots \dots (1.11)$$

1.9.2 Hall Effect

The Hall effect is a widely used method to determine the type of the carriers, the concentration, and the mobility in the semiconductors [35].

When a constant current (I) follows along the x-axis from right to left in the presence of a z-directional magnetic field (B); electrons are subjected to the Lorentz force initially, and they drift toward the negative y-axis, resulting an excess surface electrical charge on the side of the sample and causing a transverse voltage; this transverse voltage is known the Hall voltage (V_H) as shown in Fig. (1.14).

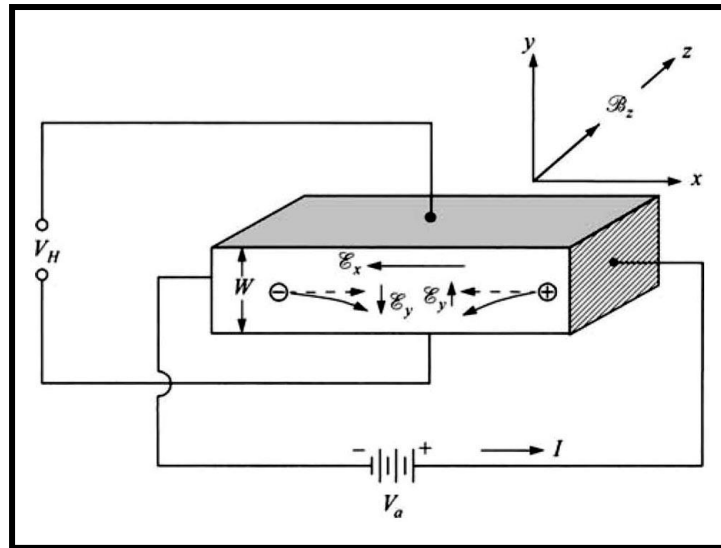


Fig. (1.14) Schematic diagram of Hall effectt [37].

The Hall coefficient R_H is determined by measuring the Hall voltage that generates the Hall field across the sample of thickness t , by [36]:

$$R_H = \frac{V_H}{I} \cdot \frac{t}{B} \dots\dots\dots (1.12)$$

where B is the applied magnetic field

Carriers concentration can be determined by using the relation [35]

$$n_H = \frac{-1}{qR_H} \dots\dots\dots (1.13)$$

for electrons

or

$$p_H = \frac{+1}{qR_H} \dots\dots\dots (1.14)$$

for holes.

Hall's mobility (μ_H) can be written in the form [36]

$$\mu_H = \frac{\sigma}{n \cdot q} \dots\dots\dots (1.15)$$

$$\mu_H = \sigma |R_H| \dots \dots \dots (1.16)$$

1.10 Optical Properties

The optical properties of a semiconductor can be defined as any property that involves the interaction between electromagnetic radiation and the semiconductor, including absorption, diffraction, polarization, reflection, and scattering effects. The best values of the band gap are obtained by the measurement of optical absorption [36]. The absorption of radiation in semiconductors which leads to the electronic transition between the V.B, and the C.B may be divided into direct and indirect transitions as shown in Fig. (1.15).

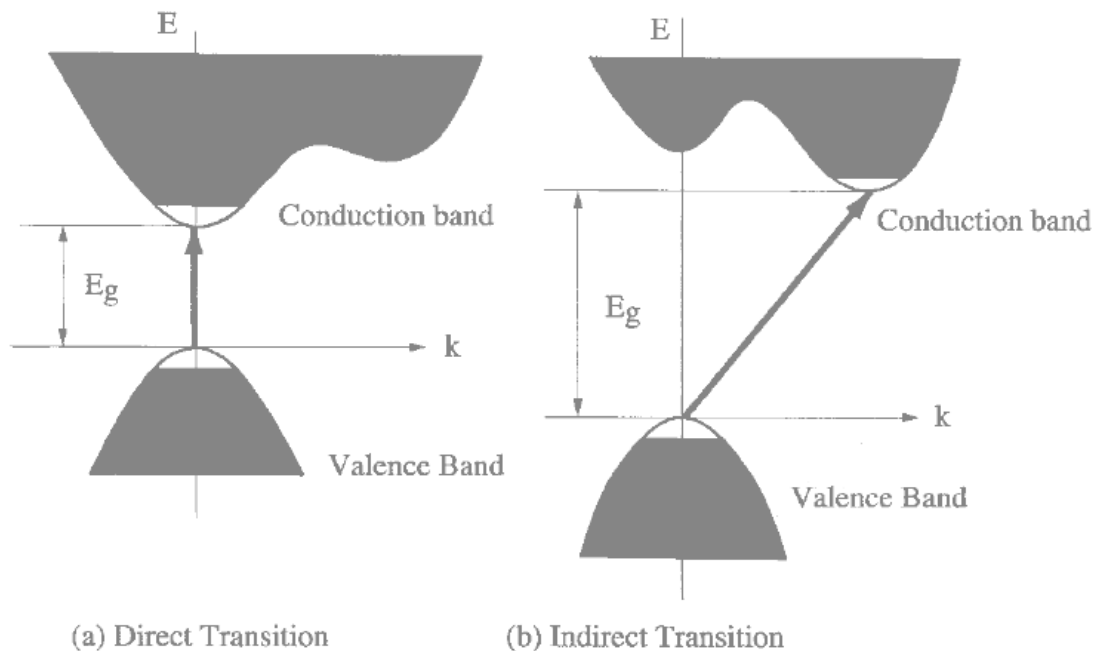


Figure (1.15): Optical transitions: (a) allowed direct, (b) allowed indirect [37].

1.10.1 Fundamental Absorption Edge

The fundamental absorption edge of polycrystalline or crystalline semiconductor is the region in which the electrons are transferred (excited)

from the valence band to conduction band by absorbing the incident photons and create electron-hole pairs. These photons should have energy greater than energy gap of semiconductor [36]. It manifests itself by a rapid rise in absorption, which can be used to determine the energy gap of the semiconductor [38]. The electronic transition between the V.B and the C.B starting at the absorption edge which corresponds to minimum energy difference E_g between the lowest minimum of the C.B and the highest maximum of the V.B [37].

The wavelength ($\lambda_{\text{cut of}}$) of the incident photon, which creates the electron-hole pair is defined as [39]:

$$\lambda(\mu\text{m}) = \frac{hc}{E_g} = \frac{1.24}{E_g(\text{eV})} \dots\dots\dots (1.17)$$

when

The light of intensity I_0 incident on the film of thickness (t), the transmitted intensity I can be given as [40]

$$I = I_0 \exp(-\alpha t) \dots\dots\dots (1.18)$$

where

α : is the absorption coefficient.

t: is the thickness of the film.

I: is the transmitted intensity

λ : is the wavelength of the incident radiation and

The absorption edge becomes wide for unideal, polycrystalline and amorphous semiconductor because the allowed localized levels are found in energy gap. The width of the localized levels can be calculated using Urbach Rule [41].

$$\alpha = \alpha_0 \cdot e^{(h\nu/\Delta E)} \dots\dots\dots (1.19)$$

α_0 is a constant, $h\nu$ is the photon energy, and ΔE is the width of localized levels into energy gap.

1.10.2 Direct Transitions

The direct transition occurs between top of valence band and the bottom of conduction band (vertical transition), without changing the wave vector \vec{k} of electrons as shown in Fig. (1.15). This transition is described by the following relation

$$\alpha(h\nu) = B (h\nu - E_g)^r \dots\dots\dots (1.20)$$

where

B is constant involving the properties of the bands, r is a constant depending on the nature of transition.

The direct transition at $\vec{\Delta k} = 0$ is called allowed transition, when the transition occurred exactly between the top of V.B and the bottom of C.B, in this case the value of r is taken to be $1/2$.

The direct transition is called forbidden if the transition occurs also between states of the same wave vector, but the wave vector does not equal to zero and $r = 3/2$ [42] .

1.10.3 Indirect Transition

In indirect transition, minimum of the conduction band and top of the valence band differ in their position in \vec{k} -space (i.e. $\vec{\Delta k} \neq 0$) [43] . As shown in Fig. (1.15). Indirect transition requires absorption or emission of phonons to balance the crystal momentum. In this transition, the electrons can not make a direct (perpendicular) transition from the valence band to the conduction band because of the change in their crystal momentum. Such transition may take place by a two step process. The electron either absorbs both a photon and a

phonon or absorbs a photon and emits a phonon simultaneously. The photon supplies the needed energy, while the phonon supplies required momentum conservation. This transition is also described by eq. (1.20). The allowed indirect transition occurs from the top of the V.B to the bottom of the C.B, and $r = 2$, while, the forbidden indirect transitions occur from any point near the top of V.B to any point other than the bottom of C.B, and $r = 3$ [42].

1.10.4 Optical Constants

The optical constants fully describe the optical behavior of materials; they are important and fundamental properties of matter [44,45]. The optical properties of an evaporated film depend strongly on the technique of evaporation[46]. Knowledge of optical constant of a film from a given material is basic importance in determining the characteristics of light transmission in the film. Such knowledge of the optical parameters of the material is of importance when designing devices through which electromagnetic radiation absorbed or transmitted. The absorption coefficient of the material is a very strong function of the photon energy and band gap energy. Absorption coefficient represents the attenuation that occurs in incident photon energy on the material for unit thickness, and the main reason for this attenuation is attributed to the absorption processes [47]. Optical constants included refractive index (n), extinction coefficient (k), and real (ϵ_r) and imaginary parts (ϵ_i) of dielectric constant. The refractive index (n) can be calculated from the following equation [48].

$$n = \left[\frac{4R}{(R-1)^2} - k^2 \right]^{1/2} - \frac{(R+1)}{(R-1)} \dots\dots\dots (1.21)$$

where R: is the reflectance and given by the equation[49]:

$$R = \frac{(n-1)^2 + k^2}{(n+1)^2 - k^2} \dots\dots\dots (1.22)$$

The extinction coefficient (imaginary part of the refractive index), which is related to the exponential decay of the wave as it passes through the medium can be determined by using equation[50,51] :

$$k = \frac{\alpha\lambda}{4\pi} \dots\dots\dots (1.23)$$

where α is given by [51]

$$\alpha = 2.303 \frac{A}{t} \dots\dots\dots (1.24)$$

where A: is the absorbance and t is the sample thickness.

The real and imaginary part of the dielectric constant (ϵ_r and ϵ_i) can be calculated by using equations[52]:

$$\epsilon_r = n^2 - k^2 \dots\dots\dots (1.25)$$

$$\epsilon_i = 2nk \dots\dots\dots (1.26)$$

1.11 Literature Survey

The sun's energy can be concentrated and it's spectrum divided into visible light and infrared where the visible light can be used for applications such as plant growth or building interior lighting and the IR can be converted to electricity using low bandgap GaSb photovoltaic cells. Most recently some additional applications for GaSb have emerged such as building lighting and plant lighting. For these applications the solar spectrum is divided into 2 parts with optical filters. The high-energy visible light is used for one purpose while longer wavelength energy, greater than 0.7 microns for example, is directed onto GaSb photovoltaic cells to generate electricity at incident flux power densities approaching 20 W/cm² [53].

A. Gheorghiu et. al(1982) have prepared thin (200-1000 Å) films of amorphous GaSb by deposited them under ultra-high vacuum by flash-evaporation of crystalline powder onto super smooth silica substrates maintained at different temperatures between 100 and 390 K.

The optical gap E_g determined is equal to 0.64 eV for nearly stoichiometric films deposited or annealed at room temperature. It increases to 0.74 eV after high-temperature annealing, i.e. a value very close to the crystalline minimum gap. The activation energy is significantly larger than half the optical gap (0.55 eV compared to 0.37 eV). This means, either a strong temperature dependence of the gap width, or a shift of the Fermi level due to localized states related to some specific defects. Below room temperature, the observed activated behavior, again in contradiction with amorphous Ge or GaAs, suggests transport by hopping following excitation in tail states at the band edge. It is remarkable that variable-range hopping conduction in states near the Fermi level is not observed, either before or after annealing, although numerous defects are obviously present in the films [54].

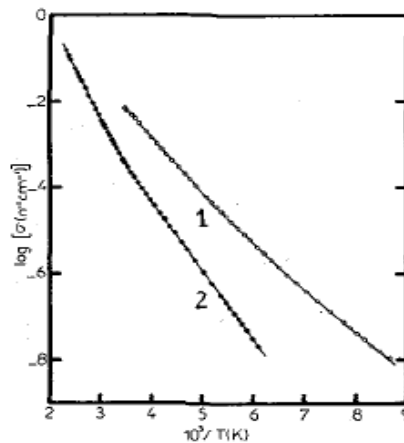


Fig. (1.16) Conductivity σ versus reciprocal temperature T for amorphous GaSb films deposited at 100 K and annealed at 300 (graph 1) and 420 K (graph 2) [54].

M. Munoz Urbi et.al (1996) have measured the refractive index of p-type GaSb ($1.0 \times 10^{17} \text{ cm}^{-3}$ at 300 K) for the transparent region from 1.8 to $2.56 \mu\text{m}$ as shown in Fig.1.17 using refraction of light in a prism [55] .

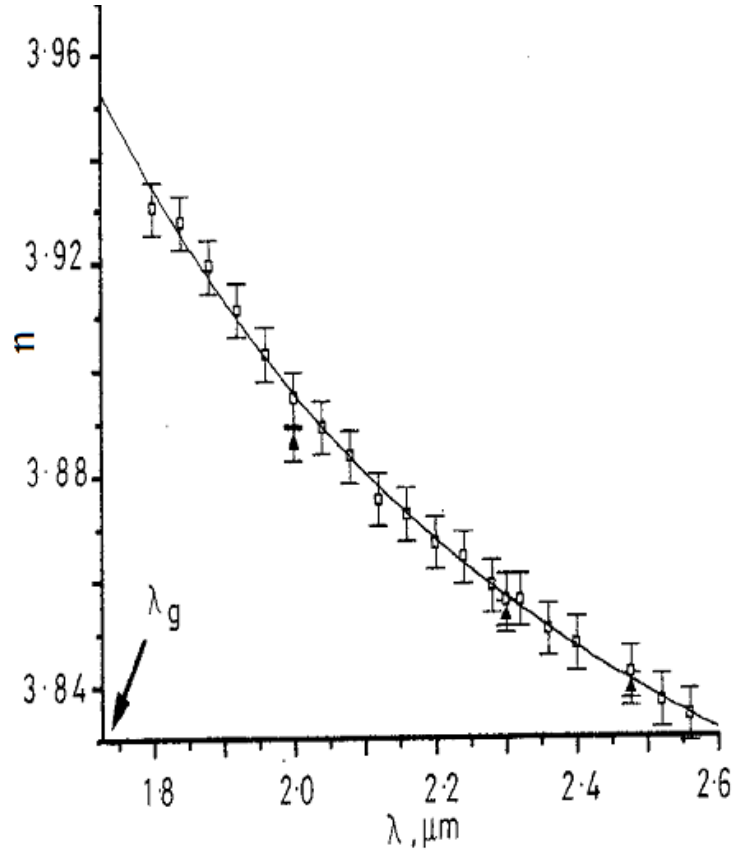


Fig.(1.17) Fit of prism data by single oscillator model [55] .

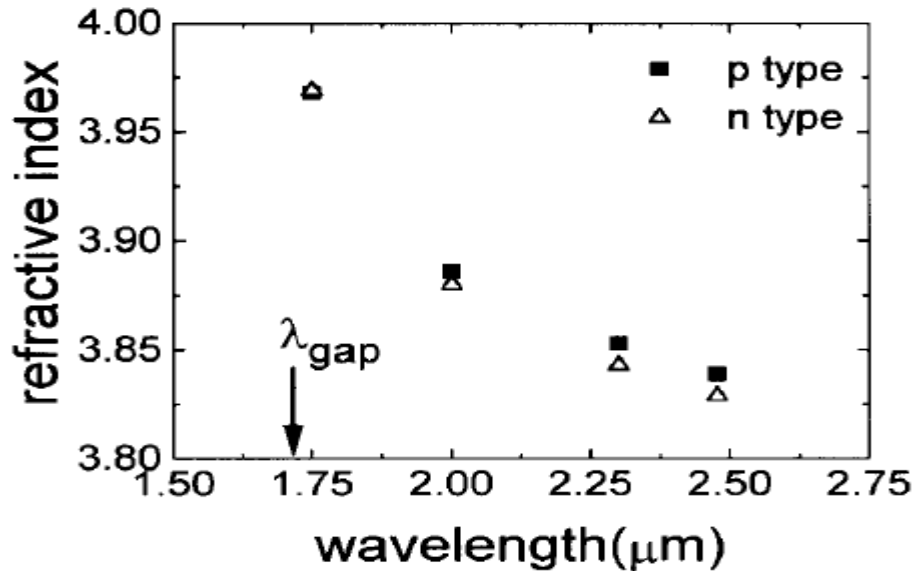


Fig.(1.18) Plot of refractive index vs. wavelength for p- and n-doped GaSb.[56]

In the same year another researcher have reported the refractive index measurements of the GaSb by using the ellipsometry technique for the wavelength region below band gap ranging for 1.75 to 2.5 μm . They found that below the band gap the index values for the n-type material are slightly smaller than the corresponding values for the p-type substrate. This is expected, because band filling in the conduction band increases the average gap and hence decreases the dielectric constant. This effect is not relevant for the p-type material, because the hole density is two orders of magnitude smaller ($1.5 \times 10^{15} \text{ cm}^{-3}$) while for a n-type ($4.6 \times 10^{17} \text{ cm}^{-3}$) besides the density of states being higher in valance band [56].

Lilik Hasanah et. al (2003) have reported Gallium Antimony (GaSb) thin film were grown on semi Insulating (SI) GaAs (100) substrate by MOCVD (Metal-Organic Chemical Vapor Deposition) method. (TMGa)

(Trimethylgallium) and (TDMASb) (Tridimethyl amino antimony) were used as precursors of group III and V, respectively, with H_2 as gas carrier. The films were grown with V/III varied between 1.15 and 3.1. V/III ratio dependent of surface morphology and atomic composition of GaSb thin films were studied. The best surface morphology stoichiometric GaSb obtained at the V/III ratio of 2.0 [57].

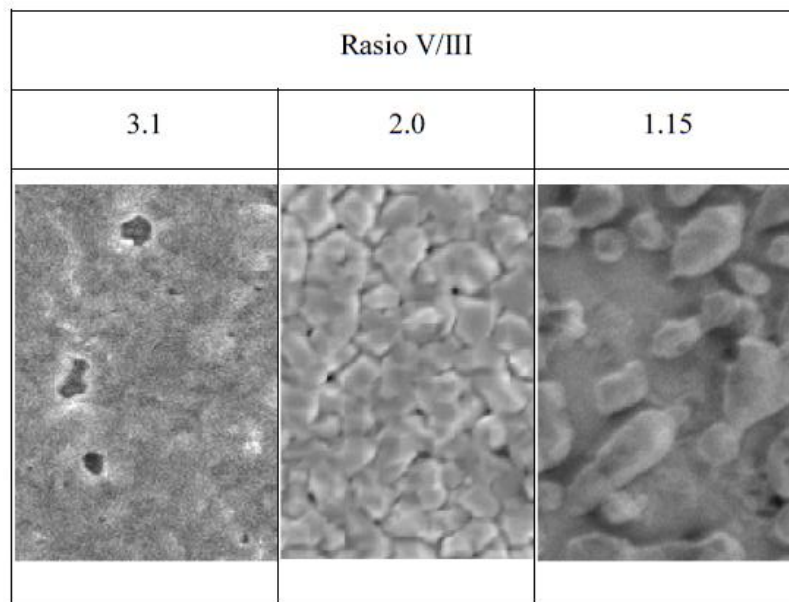


Fig. (1.19) SEM photos for different Sb/Ga ratios [57].

Yingda Dong et.al(2003) showed low resistance poly-GaSb films can be achieved by MBE growth using CBr_4 doping. The resistivity of poly-GaSb has strong dependence on film's thickness and grain size, particularly when the film thickness is comparable with the grain size. It has been found that growth temperature strongly influence the grain size, but has little effect on hole concentration. The hole concentration, on the other hand, is significantly affected by the antimony to gallium beam flux ratio, with low V/III ratios increasing the carbon incorporation. Therefore, low growth temperature and low V/III beam flux ratio are desirable to achieve low-resistivity poly-GaSb

films. With the same doping level ($8 \times 10^{19} \text{ cm}^{-3}$), grain size ($\sim 100 \text{ nm}$) and similar film thickness, the resistivity of poly-GaSb is found to be more than one order of magnitude lower than that of poly-GaAs. This low resistivity is attributed to GaSb's favorable surface Fermi level pinning position and higher hole mobility [58].

Liu et.al(2004) had utilized Te-doped n-GaSb wafers with a carrier concentration of about 10^{17} cm^{-3} was used. All wafers were chemically degreased, and then blown dry with nitrogen. The back side ohmic contacts were made by electron-beam (e-beam) evaporation of Au-Ge/Ni/Au and then alloyed at $300 \text{ }^\circ\text{C}$ for 4 min. The Schottky diode fabricated on a GaSb surface after such HCl treatment exhibits both an increased zero-bias barrier height (0.46 eV) and a decreased ideality factor (1.89). Before the deposition of Au contact on the topside, the GaSb surface was prepared in several ways, including chemical degreasing, immersion in concentrated HCl, or sulfide treatment in aqueous or nonaqueous Na_2S -saturated solutions. the Au/n-GaSb contact exhibits Schottky junction behavior. benzene-based nonaqueous sulfidization prior to metallization increases the Au/n-GaSb barrier height to 0.61 eV and reduces the ideality factor to close to unity [59].

Guo et. al (2006) had reported that highly lattice mismatched (7.8%) GaAs/GaSb nanowire heterostructures were grown by metal-organic chemical vapor deposition and their detailed structural characteristics were determined by electron microscopy. The facts that (i) no defects have been found in GaSb and its interfaces with GaAs and (ii) the lattice mismatch between GaSb/GaAs was fully relaxed suggest that the growth of GaSb nanowires is purely governed by the thermodynamics. The authors believe that the low growth rate of GaSb nanowires leads to the equilibrium growth. By careful measurement

of corresponding atomic planes for GaAs and GaSb, a $7.5 \pm 0.3\%$ lattice mismatch was determined by using the equation [60].

$$f = \frac{d_{GaSb}^{hkl} - d_{GaAs}^{hkl}}{d_{GaAs}^{hkl}} \dots\dots\dots (1. 27)$$

At same year V.P Khvostikov et.al [61] examined the methods for reducing the resistance of ohmic contacts to *p* and *n* GaSb. The minimum values of the specific resistance of contacts, $(1-3) \times 10^{-6} \Omega \text{ cm}^2$, to *p* GaSb with the doping level of 10^{20} cm^{-3} were obtained using the Ti/Pt/Au contact system. For *n* GaSb ($n = 2 \times 10^{18} \text{ cm}^{-3}$), the minimum values of the specific contact resistance were equal to $(1-3) \times 10^{-6} \Omega \text{ cm}^2$ and were obtained using the Au(Ge)/Ni/Au and Au/Ni/Au contact systems. They developed and studied high-efficiency GaSb photovoltaic cells designed for conversion of high power monochromatic radiation and infrared radiation of emitters. The maximum conversion efficiency of GaSb photovoltaic cells was 49% for the incident radiation with the wavelength of $\lambda = 1680 \text{ nm}$ [61].

Shenghong Huang(2007) had reported that the growth of the GaSb bulk on GaAs was done in a MBE reactor. The valved crackers are used for the As and the Sb sources. Substrate temperature is measured with a pyrometer. Growth is initiated with the deoxidation of the GaAs substrate at 600°C . This is followed by the reduction of the substrate temperature to 560°C and the growth of 1000 \AA of GaAs to obtain a smooth surface. The surface reconstruction is constantly monitored by RHEED pattern and at this point is noted to be an expected (2 x 4) pattern indicating an As-rich surface. After completion of the homoepitaxy, the substrate temperature is brought down to 510°C with a constant As overpressure. At this point they close the As valve and the GaAs surface starts losing the surface As. The misfit separation,

measured to be 5.6 nm, corresponds to exactly 13 GaSb lattice sites grown on 14 GaAs lattice sites. The identical misfit arrays have been observed along both $[110]$ and $[1\bar{1}0]$ directions, which showed that there is a 2D 90° pure edge dislocation array at the compressive GaSb/GaAs interface. It is shown that the GaAs to GaSb ratio is precisely 14:13. It be verified with very simple arithmetic that the lattice space occupied by 14 atoms of GaAs along the $[110]$ direction is about the same as that occupied by 13 atomic spaces of GaSb.

This is shown as follows [62]:

$$\text{For GaAs, } (14 \times d_{110}) = 14 \times (5.65/1.414) = 55.94 \text{ \AA}$$

$$\text{For GaSb, } (13 \times d_{110}) = 13 \times (6.09/1.414) = 55.99 \text{ \AA}$$

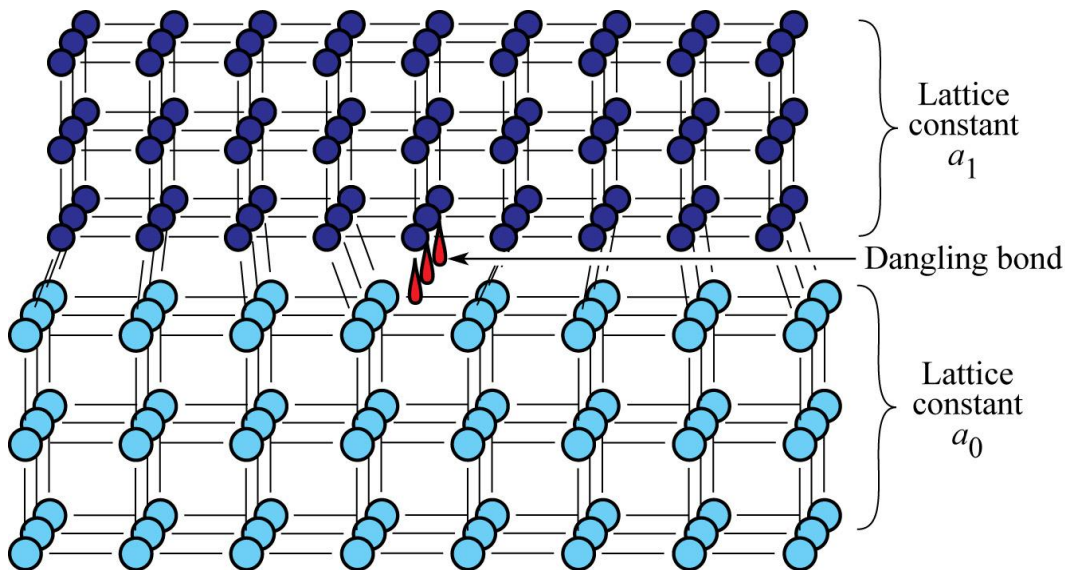


Fig.(1.20) Illustration of two crystals with mismatched lattice constant resulting in dislocations at or near the two semiconductors [62].

The electrical and magnetic properties of GaSb:Mn layers deposited on (100) GaAs substrates from a laser plasma in vacuum had studied by N. A. Sobolev et. al(2007). They were shown that the films deposited at 200–440 °C are mosaic single crystalline and epitaxial to the substrate, with p-type

conduction. Manganese-doped layers had a hole concentration higher than $1 \times 10^{19} \text{ cm}^{-3}$ and fairly high values of mobility (up to $40 \text{ cm}^2/\text{Vs}$ at 300 K). The layers grown at $200 \text{ }^\circ\text{C}$ exhibited an anomalous Hall effect up to approximately room temperature. On the contrary, a normal Hall effect was observed in the layers grown at $440 \text{ }^\circ\text{C}$. Ferromagnetic resonance measurements have revealed the existence of ferromagnetism in the sample grown at $200 \text{ }^\circ\text{C}$. The substrate was heated up to a temperature $T_s = 200\text{--}440 \text{ }^\circ\text{C}$. The resulting films were $40\text{--}140 \text{ nm}$ thick. The X-ray diffraction had proven that the films were mosaic single crystalline and epitaxial to the substrate. The properties of the deposited layers depended on the growth temperature. Undoped GaSb was of p-type conductivity with hole concentrations of 1.6×10^{19} and $2 \times 10^{18} \text{ cm}^{-3}$ for $T_s = 200 \text{ }^\circ\text{C}$ and $440 \text{ }^\circ\text{C}$, respectively. The undoped GaSb layers exhibited the normal Hall effect. Doping of GaSb layers by Mn during the growth at $T_s = 200 \text{ }^\circ\text{C}$ led to the emergence of the anomalous Hall effect persisting up to at least room temperature. The anomalous Hall effect characteristics are presented in Fig. (1.21) [63].

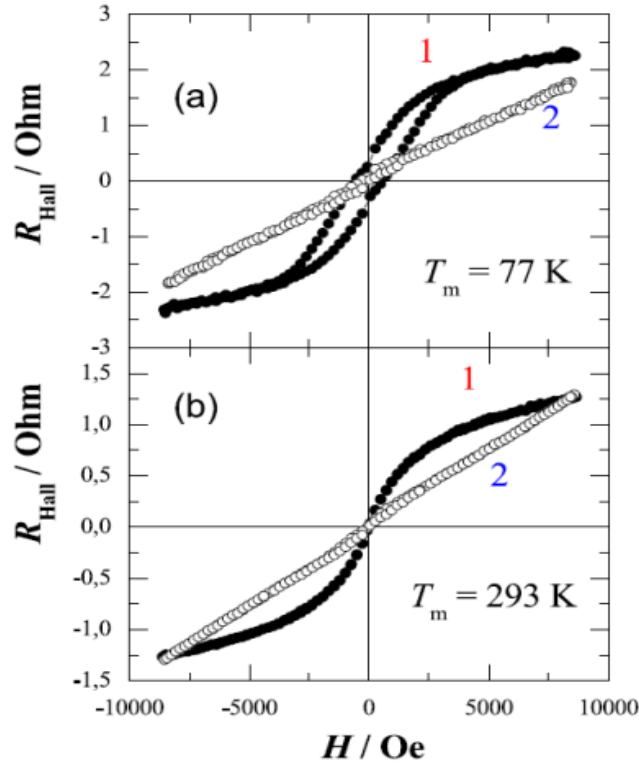


Fig. (1.21) Hall resistance dependences on the magnetic field for two GaMnSb layers (Mn concentration is ≈ 10 at.%) [63] sample (1) $p = 1.5 \times 10^{20} \text{ cm}^{-3}$, $T_s = 200^\circ \text{C}$, $d = 70 \text{ nm}$; sample (2) $p = 3 \times 10^{19} \text{ cm}^{-3}$, $T_s = 440^\circ \text{C}$, $d = 140 \text{ nm}$.

Low energy ion-beam sputtering of GaSb results in self-organized nanostructures, with the potential of structuring large surface areas. Characterization of such nanostructures by optical methods was studied and compared to direct (local) microscopic methods by I.S. Nerbo et al. (2008). The samples consist of densely packed GaSb cones on bulk GaSb, approximately 30, 50 and 300 nm in height, prepared by sputtering at normal incidence. Good agreement is achieved between the two classes of methods when the experimental optical response of the short cones ($< 55 \text{ nm}$) was inverted with respect to topological surface information via a graded anisotropic effective medium model. The main topological parameter measured was the average cone height, but estimates of typical cone shape and density (in terms of volume fractions) were also obtained. The longer cones (300 nm) were found

experimentally to give rise to considerable reduction in the measured degree of polarization. This is presumably caused by multiple scattering effects, Moreover, the reflectance of the samples were also measured and modeled, and found to be reduced significantly due to the nanostructuration. The nanostructuration of the surface was shown to considerably reduce the reflectance. The antireflecting properties increased with cone height. Samples with long nanocones (200–300nm) were found to be strongly depolarizing [64].

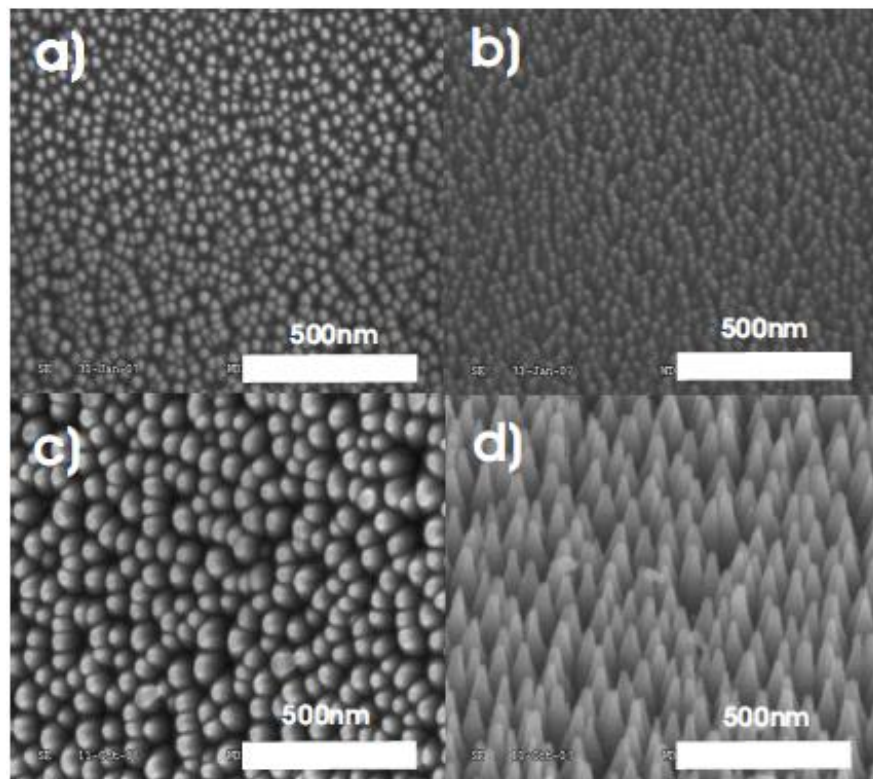


Fig.(1.22) SEM images of GaSb nanocones. Figure (a), sample A at normal beam incidence, (b) tilted sample A. Sample D is also depicted at (c) normal beam incidence and (d) tilted beam incidence [64].

Jallipalli et. al(2009) reported structural analysis of completely relaxed GaSb epitaxial layers deposited monolithically on GaAs substrates using interfacial misfit (IMF) array growth mode. Recent technical advancements have enabled high quality lattice matched GaSb epitaxy on native substrates,

for many applications GaAs substrates are desirable. This is because of the following reasons: GaAs is inexpensive, has favorable thermal properties, transparent to more (long wave length) active regions, forms excellent n and p ohmic contacts, and can be semi-insulating compared to GaSb. However, the high (7.8%) lattice mismatch between the GaSb epilayer and the GaAs substrate complicates the growth of sophisticated device structures. Currently, this mismatch is accommodated via metamorphic buffer layers and strain-relief superlattices. In metamorphic buffer layer approach, initially the strain within the critical thickness is accommodated by tetragonal distortion followed by defect formation and filtering. While this approach has enabled a number of device demonstrations, it exhibits several deficiencies such as the necessity to grow thick buffer layers (often about $1\mu\text{m}$), poor thermal and electrical conductivity, and has resulted in significant material degradation through the presence of threading dislocations (TDs) [65].

Qiao Zaixiang et.al(2009) prepared polycrystalline GaSb thin films grown by coevaporation on soda-lime glass substrates. The thin films have preferential orientation of the (111) direction. SEM results indicate that the average grain size of GaSb thin film is 500 nm with the substrate temperature of $560\text{ }^\circ\text{C}$. The average reflectance of GaSb thin film is about 30% and the absorption coefficient is of the order of 10^4 cm^{-1} . The optical bandgap of GaSb thin film was 0.726 eV. The hole concentration showed a clear increasing trend as the Ga evaporation-temperature / Sb-evaporation-temperature ($T_{\text{Ga}}/T_{\text{Sb}}$) ratio increases. When the Ga crucible temperature is $810\text{ }^\circ\text{C}$ and the antimony crucible temperature is $415\text{ }^\circ\text{C}$, the hole concentration of polycrystalline GaSb is $2 \times 10^{17}\text{ cm}^{-3}$ and the hole mobility is $130\text{ cm}^2/(\text{V}\cdot\text{s})$.

These results suggest that polycrystalline GaSb thin film is a good candidate for the use as a cheap material in thermal photovoltaic TPV cells [66].

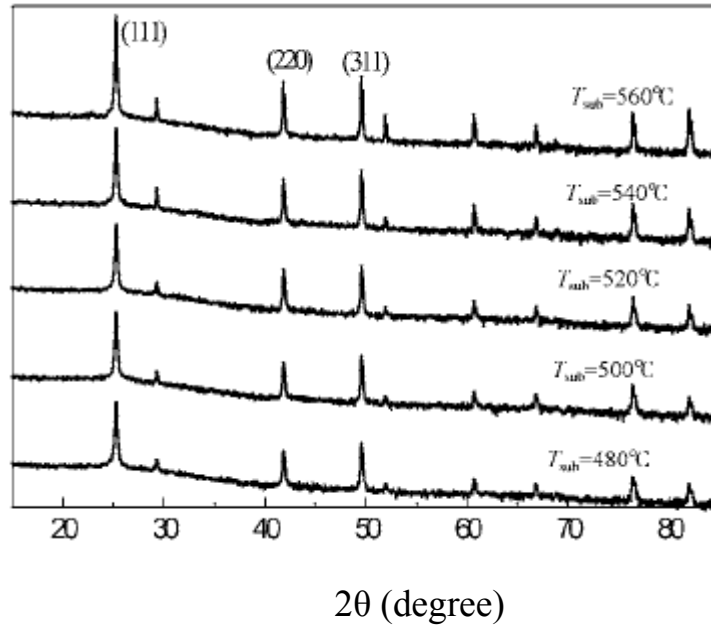


Fig. (1.23) XRD patterns for GaSb thin films of different substrate temperatures [66].

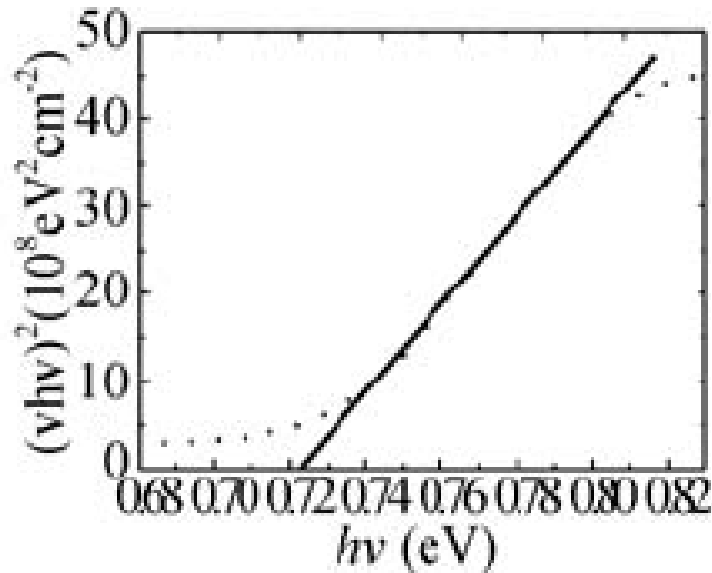


Fig. (1.24) Absorption coefficient of the GaSb film [66].

L. Zheng et.al (2000) have shown that the diode characteristics of MOVPE grown of p-GaSb/n-GaAs junctions are strongly influenced by the growth temperature. The acceptable growth temperature considering both epilayer quality and growth rate is 500-520°C. They investigate the effect of doping and GaSb epilayer thickness on dark and photo I-V curves, and on spectral response. The optimum GaSb thickness is a trade-off between the diffusion length and the thickness required to maximise light absorption. The highest open circuit voltage, V_{oc} (0.33V) to date has been obtained from a thin (0.3 μm) GaSb layer doped at $6 \times 10^{16} \text{ cm}^{-3}$, under illumination by a focused tungsten-halogen lamp (1 w cm^{-2}) The short circuit current, I_{sh} was (13 mA/cm^2) with a corresponding fill factor of 0.63, and an external quantum efficiency of 10% [67].

1.12 The aim of the work

There are a lot of progress have been done for utilization a lot of progress have been done for utilization of various evaporation techniques to prepare and study the properties of $\text{Ga}_x\text{Sb}_{1-x}$ films and $\text{Ga}_x\text{Sb}_{1-x} / \text{GaAs}$ heterojunction devices. The flash evaporation technique is much less complicated than the techniques currently used for fabrication $\text{Ga}_x\text{Sb}_{1-x} / \text{GaAs}$ heterojunction. The aim of present work is to utilize this flash evaporation method to prepare $\text{Ga}_x\text{Sb}_{1-x}$ films with various Ga content, substrate temperature and thickness which deposited on (111) p- and n-type GaAs wafer and investigate their physical properties such as composition of the element, structural, electrical, optical and optoelectronic properties. The ultimate objective of our study is obtained a series of related results from measurements of different physical properties which we hope to be suitable for using them in various optoelectronic devices.

C h a p t e r T w o

Experimental Procedure and Measurements

2.1 Introduction

This chapter includes the preparation and processing of $\text{Ga}_x\text{Sb}_{1-x}$ alloys and technique employed to produce $\text{Ga}_x\text{Sb}_{1-x}$ thin films at various gallium percentages (x) substrate temperatures (T_s) and thicknesses (t), which deposited onto glass substrates, n- and p- GaAs type wafers, Table (2.1) shows some specifications of GaAs wafers.

Table (2.1) Some specifications of GaAs wafers.

Type	Doped by	Orientation	Concentration (cm^{-3})	Thickness (μ)
p-type	Zn	111	$1-2 \times 10^{17}$	450
n-type	Te	111	$2-4 \times 10^{18}$	600

The $\text{Ga}_x\text{Sb}_{1-x}$ alloys prepared used as a source to prepare the films having thickness (200, 300 and 400 nm). The composition of prepared alloys and films were determined by using energy dispersive x-ray spectroscopy (EDXS). The X-ray diffraction (XRD) and scanning electron microscope (SEM) techniques were employed to determine the crystal structure of prepared alloys and films.

The electrical measurements (D.C conductivity and Hall Effect) were made for films deposited on glass substrates. The optical properties of these films are presented.

Electrical measurements were examined for n and p - $\text{Ga}_x\text{Sb}_{1-x}$ /n and p -GaAs heterojunction with different thickness (200,300 and 400) nm of GaSb, which include current-voltage (I-V) characteristics (dark and under illumination) and capacitance-voltage (C-V) characteristics. Built-in potential, type of the junction were calculated from C-V measurements. Solar cell efficiency was determined from I-V measurements in the illumination condition. All these procedures are illustrated schematically in Fig. (2.1).

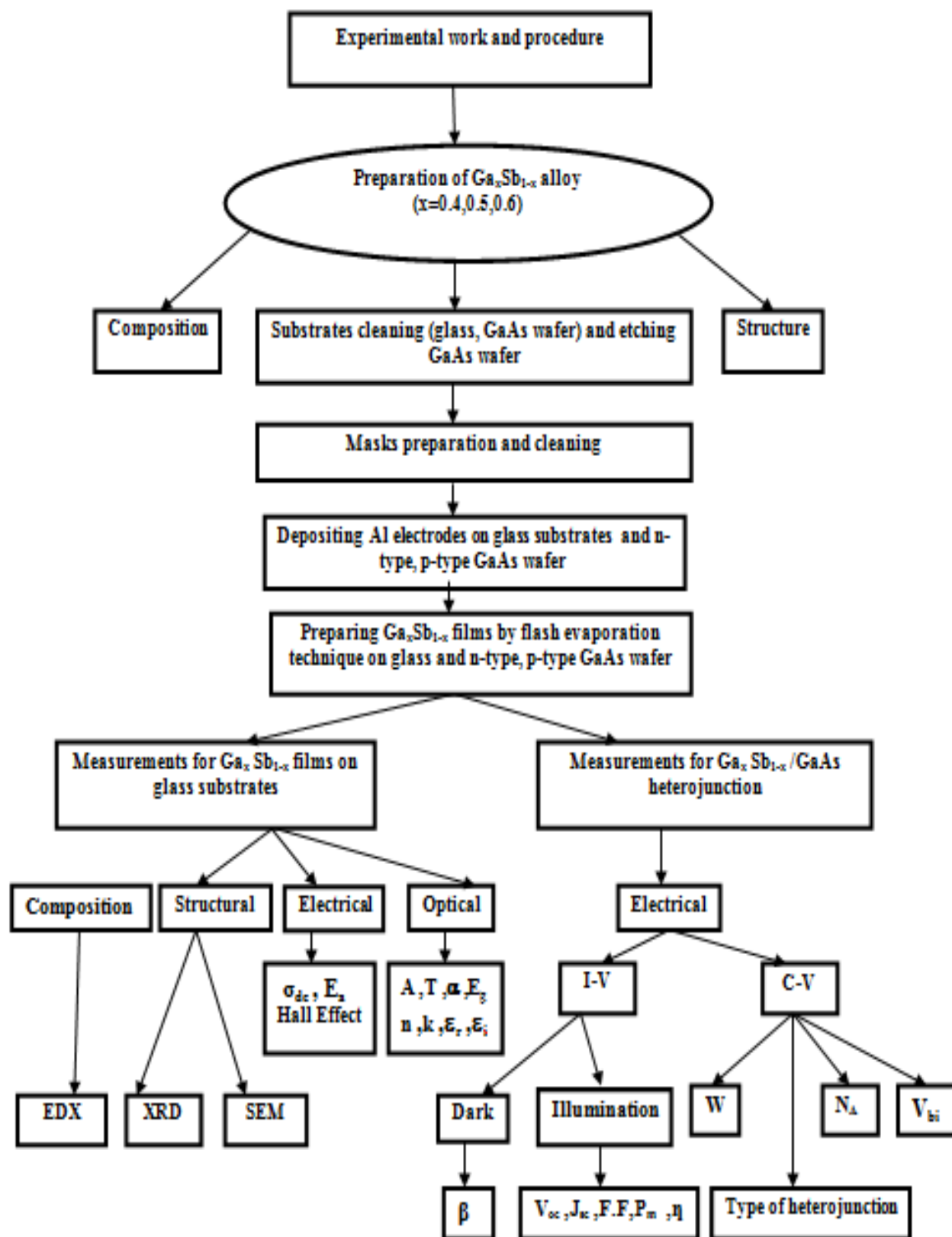


Fig. (2.1): Schematic diagram for the experimental work.

2.2 GaSb Compound Preparation

The $\text{Ga}_x\text{Sb}_{1-x}$ with various gallium percentage ($x= 0.4,0.5$ and 0.6) prepared as alloys by mixing appropriate weights of Ga and Sb using stoichiometric and high purity (99.999%) gallium metal packed under argon, obtained from Certified Chemicals, UK and (99.95%) antimony obtained from Fluca, Germany. Each element weighted according to its atomic weight and then mixing in quartz ampoule evacuated under 10^{-3} mbar pressure. The tube was sealed and heated in electrical program controller furnace type (Nabertherm), Germany, with a rate of 200 K per hour in steps up to 1173 K, and also maintained at this temperature for about one hour and then allowed to cool slowly to room temperature. After that the ampoule was broken and the prepared compound of $\text{Ga}_x\text{Sb}_{1-x}$ taken out and crushed to a fine grain powder. The powder of the compounds was used as a source of the evaporation to prepare the $\text{Ga}_x\text{Sb}_{1-x}$ films. Fig.(2.2) illustrates the dimension of prepared $\text{Ga}_x\text{Sb}_{1-x}$ alloy.



Fig. (2.2): Prepared $\text{Ga}_x\text{Sb}_{1-x}$ alloy.

2.3 Substrate Cleaning

The nature of the substrate is extremely important because it greatly influence the properties of the films deposited on it. The effectiveness of the

cleaning of substrates has strong effect on the adhesion properties of the deposited films. The substrate ideally should not have any chemical reaction and can not change the properties of the film except for sufficient adhesion [37].

The substrates were cleaned by different methods depending on the used type.

- a) Glass slides substrates were cleaned by using detergent with water, and then they were rinsed by ultrasonic cleaner's bath filled with distilled water for 15 min. After that the substrates were rinsed by ultrasonic cleaner's bath filled with a pure alcohol for 15 min also. Finally, the slides were dried by blowing air and wiped with soft paper.
- b) Both types of GaAs wafers substrates were cleaned and etched by immersing and stirring them in chemical polishing solution that consisted of 10 ml HF, 15 ml HNO₃ and 25 ml H₂O for 3 min and then they were rinsed with distilled water and dried by immersing them in alcohol then by air blower and wiped with lens paper.

2.4 Masks preparation

The mask is a piece of aluminum foil having thickness 0.25 mm with the same size of the substrate. Various shapes of masks were used to determine the shape of films and electrodes for different measurements as shown in Fig. (2.3).

The masks were cleaned according to the following stages:

1. Immersed in HCl (5%) for five min.
2. Washed in distilled water.
3. Immersed in a pure alcohol.
4. Dried by blowing with hot dry air.

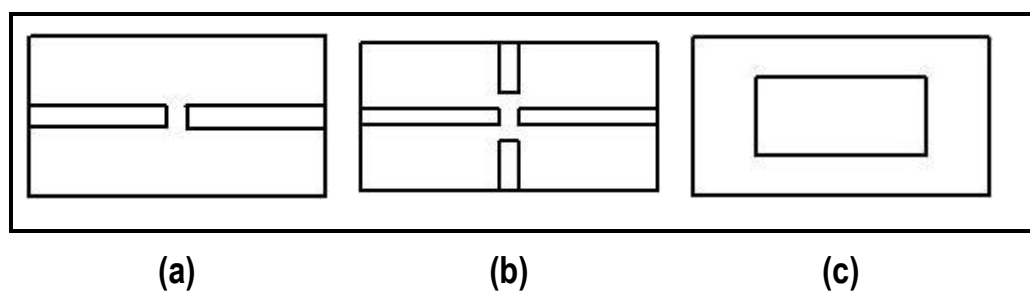


Fig.(2.3): Masks of different shapes and purposes. (a) D.C conductivity electrodes. (b) Hall effect electrodes. (c) $\text{Ga}_x\text{Sb}_{1-x}$ film deposition.

Edwards coating unit system type E306A has been used for deposition Aluminum (Al) electrodes of thickness $(0.2) \mu\text{m}$ as ohmic contact on glass substrate for electrical measurement. Indium (In) with 99.999 purity was used to connect thin wires with Al electrode.

2.5 Flash Evaporation Method

Solid materials vaporized when heated to sufficiently high temperatures. The condensation of the vapor above the substrate yields thin solid films. The deposition by the flash evaporation method is simple and very convenient.

2.5.1 Evaporation Source

The evaporation sources are metals with a high melting point, and it should not react with the evaporated material. A spiral-heating source (tungsten) was used for Al electrodes deposition as shown in Fig. (2.4a), and molybdenum boat was used for preparation $\text{Ga}_x\text{Sb}_{1-x}$ films as shown in Fig. (2.4b).

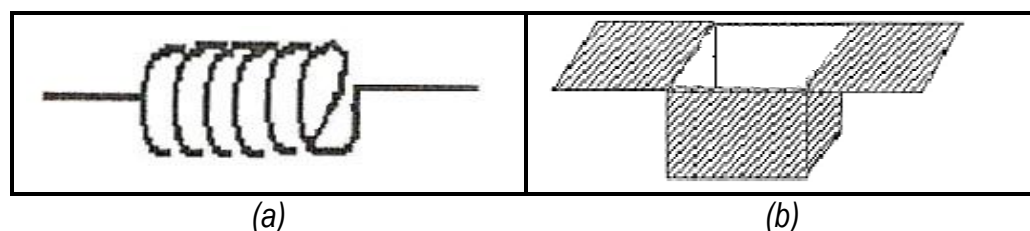


Figure (2.4): Types and shapes of boats (a) Tungsten spiral (b) Molybdenum.

The $\text{Ga}_x\text{Sb}_{1-x}$ films have been prepared by using Edwards coating unit type E306A (coating system) as shown in Fig. (2.5).

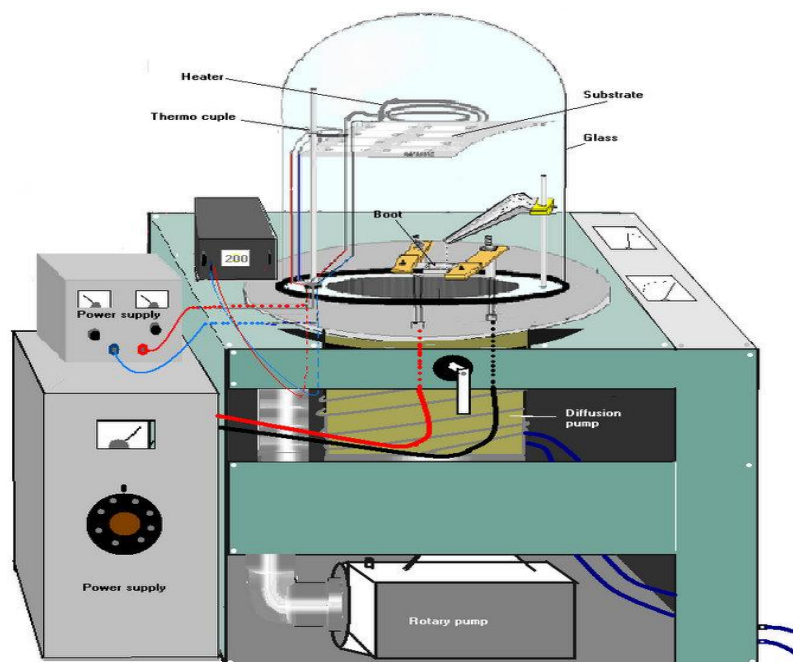


Figure (2.5): Typical coating system

2.5.2 Substrate Holder Modification

To get more homogeneous thin films we have modulate substrate holder by linking it with a small electric motor to make it rotate at two revolutions per minute as shown in Fig.(2.6). Electric motor was thermally isolated from substrate holder by putting two layers of mica paper between them.



Fig.(2.6) Modified substrate holder.

The procedure for preparing $\text{Ga}_x\text{Sb}_{1-x}$ thin films could be described as follow:

1. The required weight of $\text{Ga}_x\text{Sb}_{1-x}$ powder is charged into feed cone then by knocking on a steel bar connected from out side of bejar to feed cone the powder will gradually fall onto molybdenum boat that was mounted between two electrodes in the vacuum chamber.
2. The substrates were fixed on a hemispherical holder and placed in position at height of about 12 cm above the boat.
3. When the system was pumped down to a vacuum 10^{-5} mbar, substrates was heated to a suitable degree (T_s), then substrates holder connected with motor starts turn on and electric current was passed through the boat gradually to prevent breaking the boat.
4. The rate of deposition (R_d) was about 100 nm/min and the thicknesses of the films were 0.2, 0.3 and 0.4 μm .
5. After these steps, the current supply, substrates heater and motor were switched off and the samples were left in the high vacuum.
6. After several hours the air was admitted to the chamber then the films were taken out this coating unit, and kept in the desiccators until the measurements were made.

All the samples were prepared under constant conditions (pressure and rate of deposition); the main parameters that control the nature of the film properties are thickness (0.2, 0.3 and 0.4 μm) and substrates temperature (348, 398, 448 and 473 K).

2.6 Assembly Processes

Assembly processes were done by attaching thin wires to the heterojunction with silver paste and fixed the heterojunction on glass slide.

2.7 The Thickness Measurement

In our work, two experimental methods of thickness measurements were used:

2.7.1 Weighting Method

This method gives an approximate thickness value of the thin films with an error 25%. Film thickness (t) is determined by the relation:

$$t = \frac{m}{2\pi\rho'R^2} \dots\dots\dots (2.1)$$

where m and ρ' are the material mass and density, respectively, R is the distance between the substrate and the boat.

2.7.2 Scanning Electron Microscope Method

In this method, the thickness of the deposited films was measured using scanning electron microscope (SEM) pictures (Hitachi FE-SEM model S-4160) where samples tilted at 45°. We depend on this method in our work as shown in Fig.(2.7).

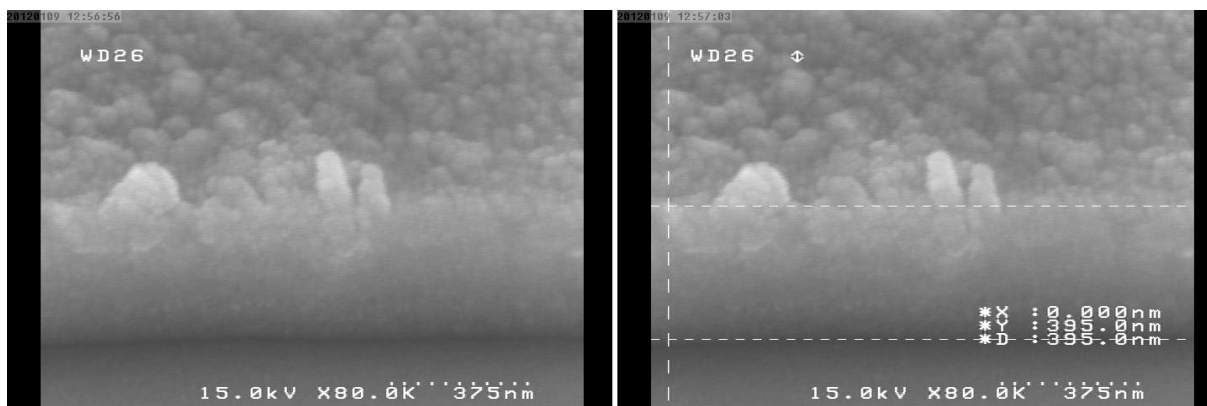


Fig. (2.7) SEM pictures show how measuring film thickness.

2.8 Energy Dispersive X-Ray Measurements

In order to know the atomic percentage of samples components, samples were examined by energy dispersive X-ray spectroscopy (EDXS).

2.9 X-Ray Diffraction

$\text{Ga}_x\text{Sb}_{1-x}$ films structure has been examined by X-ray diffraction using a Shimadzu XRD-6000 Japan.

The measure conditions are:

Target: Cu

Wavelength $\lambda_{\text{Cu}\alpha} = 1.54060 \text{ \AA}$

Voltage = 40 kV

Current = 30 mA

Scanning angle: (10° - 60°)

Scanning Speed = 5 (deg/min)

2.10 The Electrical Measurement

The electrical measurements include D.C conductivity and Hall Effect for samples deposited on glass substrate with aluminum electrodes as ohmic contact for $\text{Ga}_x\text{Sb}_{1-x}$ films with different thicknesses and substrates temperatures.

2.10.1 The D.C Conductivity Measurement

The electrical resistance has been measured as a function of temperature for $\text{Ga}_x\text{Sb}_{1-x}$ films in the range (300 – 500) K by using the electrical circuit as shown in Fig. (2.8).

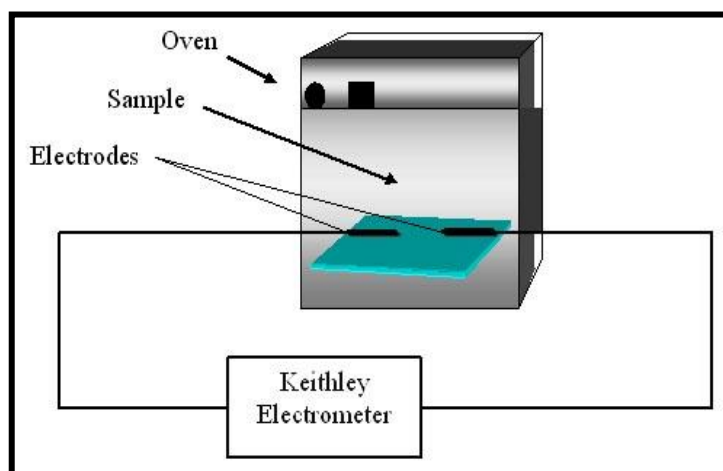


Figure (2.8): The circuit for measuring D.C. conductivity

The measurements have been done using sensitive digital electrometer type Keithley 616 and electrical oven.

The resistivity (ρ) of the film was calculated by using the following equation:

$$\rho = \frac{R'.A}{L} \dots\dots\dots (2.2)$$

where:

R': is the resistance of the film.

A: is the area of the film which is contacted with aluminum electrodes.

L: is the distance between the electrodes.

The conductivity (σ) of the films was obtained from the reciprocal of the resistivity:

$$\sigma = \frac{1}{\rho} \dots\dots\dots (2.3)$$

The activation energies could be calculated from the plot of $\ln\sigma$ versus $10^3/T$ according to equation (1.10).

2.10.2 Hall Effect Measurements

Hall Effect has been measured by using the electrical circuit as shown in Fig.(2.9), which contains D.C power supply (0-40) volt and two digital electrometers (type Keithley 616) to measure the current and voltage. When the samples carrying a current are exposed to a constant magnetic field ($B = 0.5$ Tesla) perpendicular to the electric field, then Hall voltage (V_H) is set up across the sample.

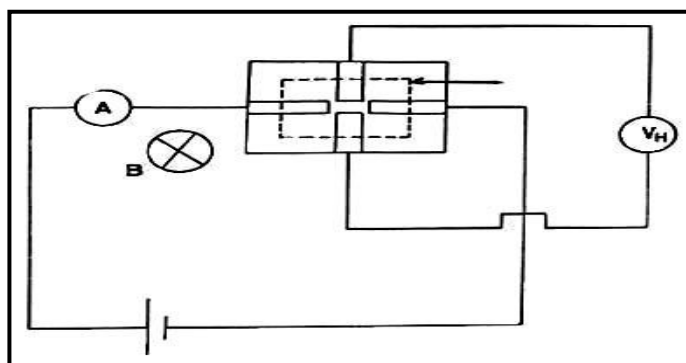


Fig. (2.9): The circuit diagram for Hall measurements

The Hall coefficient (R_H) can be found from equation (1.12). The sign of Hall coefficient determines the type of charge carriers. From the value of R_H , we can find the charge carrier concentrations n_H and p_H by using the relations (1.13), (1.14). Hall mobility μ_H can be obtained according to the equation (1.15).

2.11 Optical Properties Measurement

Optical properties of $\text{Ga}_x\text{Sb}_{1-x}$ films deposited on glass substrate with different gallium content (x), thicknesses and substrate temperatures were studied at constant temperature 300 K and in the wavelength range (1.25- 5.0) μm by using Shimadzu FTIR recorder spectrophotometer model UV-160. The output data of wavelength, transmittance and absorbance were used in a computer program to

deduce the optical energy band gap, fundamental optical edge and all optical constants.

2.11.1 Optical Energy Gap

The transmittance spectrum was used to determine the optical energy gap. The absorption coefficient, which is a measure of the rate of light loss, can be calculated using equation (1.18) at every wavelength to measure the fundamental optical edge of $\text{Ga}_x\text{Sb}_{1-x}$ film. Computer program is used and Tauc formula was employed in the program.

The value of $(\alpha h\nu)^2$ was plotted against photon energy ($h\nu$). The straight lines portion was extrapolated to zero, and the value which was obtained represented the optical energy gap.

2.11.2 Optical Constants

The optical constants (the refractive index, extinction coefficient, and dielectric constants) were calculated from transmittance and absorbance spectrum at normal incidence over the range (1.25-5.0) μm . The optical constants were calculated using equations (1.21), (1.23), (1. 25) and (1.26) for refractive index, extinction coefficient, real part of dielectric constant and imaginary part of dielectric constant, respectively.

2.12 Electrical Measurements of Heterojunction in the Dark

Current-voltage and capacitance-voltage characteristics in the dark condition were measured for $\text{Ga}_x\text{Sb}_{1-x}$ /GaAs heterojunction which were prepared at different gallium content, substrate temperatures and thicknesses.

2.12.1 Current-Voltage Measurements in the Dark

The current-voltage measurements in the dark were done by using Keithley digital electrometer type 238 high current source measurement unit and D.C power

supply. The bias voltage was varied in the range of (0-2) Volt in the case of forward and reverse bias. From plotting the relation between forward current and bias voltage, the ideality factor (β) can be determined by using the equation:

$$\beta = \frac{q}{k_B T} \cdot \frac{V}{\ln(I_f / I_{s1})} \dots\dots\dots (2.4)$$

where V , I_f , I_{s1} are the forward bias voltage, the forward current and the saturation current, respectively.

2.12.2 Capacitance-Voltage Measurements in Dark

The capacitance versus reverse bias voltage at the range (0-2) Volt with different frequencies was measured by using multi-frequency LCR meter model hp. 4274 A and 4275 A; Hewlett Packard. From this measurement, we can determine the type of the heterojunction (abrupt or graded), the value of built in voltage (V_{bi}) (can be found from the plots of the relation between $1/C^2$ and the reverse bias voltage, then the interception of the straight line with voltage axis represents the built in voltage), and the width of depletion layer(W), which can be calculated from the equation:

$$W = \frac{\epsilon_s}{C_o / A} \dots\dots\dots (2.5)$$

where C_o is the capacitance at zero biasing voltage,

A is the device area

and,

$$\epsilon_s = \frac{\epsilon_n \epsilon_p}{\epsilon_n + \epsilon_p} \dots\dots\dots (2.6)$$

where ϵ_s is the semiconductor permittivity for the two semiconductor materials, ϵ_n and ϵ_p are the dielectric constants of n-and p-type semiconductor, respectively.

The concentration of carriers was calculated from the relation :

$$\frac{1}{C^2} = \left[\frac{2(\epsilon_p N_p + \epsilon_n N_n)}{q N_p N_n \epsilon_p \epsilon_n} \right] \cdot (V_{bi} - V) \dots \dots \dots (2.7)$$

where $[2(\epsilon_p N_p + \epsilon_n N_n)/q N_p N_n \epsilon_p \epsilon_n]$ is the slope and we can calculate the carriers concentration from it.

2.13 Photoelectric Measurements of Heterojunction

2.13.1 Current-Voltage Measurements under Illumination

The current-voltage measurements under illumination of $\text{Ga}_x\text{Sb}_{1-x}$ / n- and p-GaAs heterojunction with different thicknesses of $\text{Ga}_x\text{Sb}_{1-x}$ film, at forward and reverse conditions were measured by using Halogen lamp type Philips of 100 mW/cm^2 , voltmeter, Keithley digital electrometer type 616 and D.C power supply as shown in Fig.(2.10).

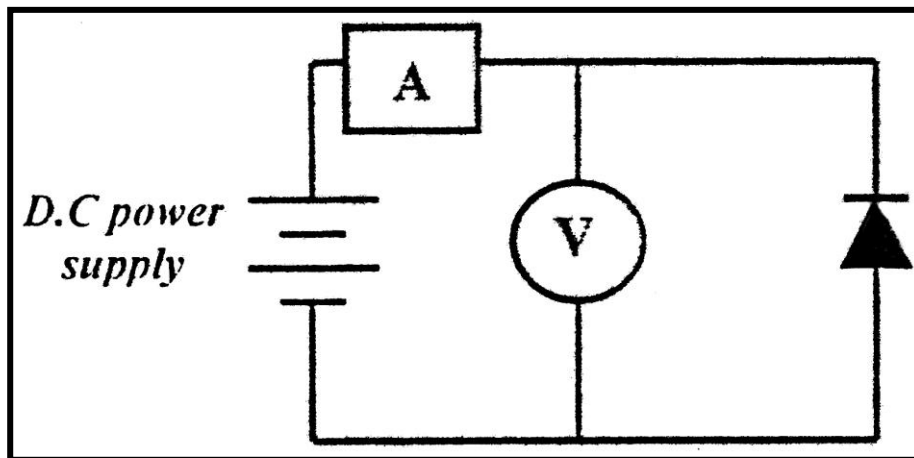
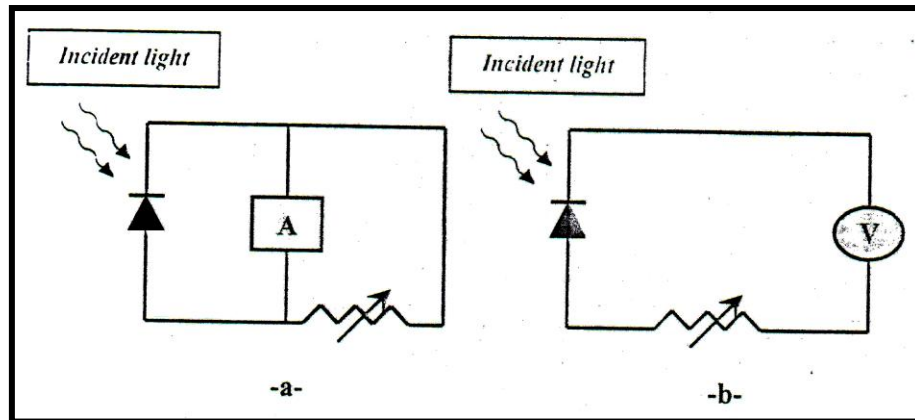


Fig. (2.10): Circuit diagram for I-V measurement

2.13.2 The Short Circuit Current and Open Circuit Voltage Measurements

The short circuit current (I_{sc}) condition occurs when $R = 0$ so that $V = 0$ while the open circuit voltage (V_{oc}) condition occurs when $R \rightarrow \infty$, where the net total current equal to zero. The I_{sc} and V_{oc} values for the $\text{Ga}_x\text{Sb}_{1-x}$ /GaAs heterojunction have been measured under illumination as shown in Fig. (2.11).



**Fig. (2.11) Circuit Diagram of (a) the short - circuit current
(b) the open – circuit voltage**

C h a p t e r T h r e e

Results and Discussion

3.1 Introduction

Results and analysis of the experimental measurements will be included in this chapter, involving composition and structural for prepared $\text{Ga}_x\text{Sb}_{1-x}$ alloys, at various Ga content also the composition, structural, electrical and optical properties of $\text{Ga}_x\text{Sb}_{1-x}$ films at different thickness, substrate temperatures and Ga content have been measured. The electrical measurements of $\text{Ga}_x\text{Sb}_{1-x}$ /GaAs Heterojunction and figure of merit for prepared structure were investigated.

3.2 Composition of $\text{Ga}_x\text{Sb}_{1-x}$ Alloys and Films

3.2.1 Energy Dispersive X-ray Spectroscopy Analyses (EDXS)

The concentrations of Ga and Sb in prepared $\text{Ga}_x\text{Sb}_{1-x}$ alloys have been determined by using energy dispersive x-ray spectroscopy (EDXS). The results of elemental concentrations are shown in Figs. (3.1) and (3.2) for bulk $\text{Ga}_x\text{Sb}_{1-x}$ and Figs. (3.3-3.5) for $\text{Ga}_x\text{Sb}_{1-x}$ thin films on glass substrates. The experimental values of Ga and Sb are almost the same as theoretical values.

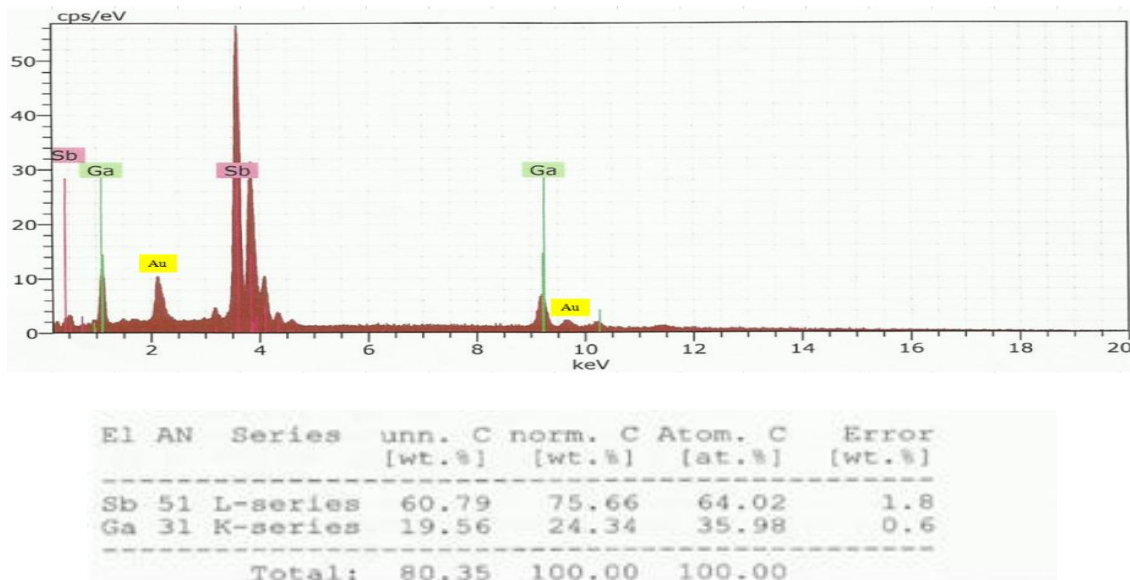


Fig. (3.1) EDXS pattern for bulk $\text{Ga}_{0.4}\text{Sb}_{0.6}$.

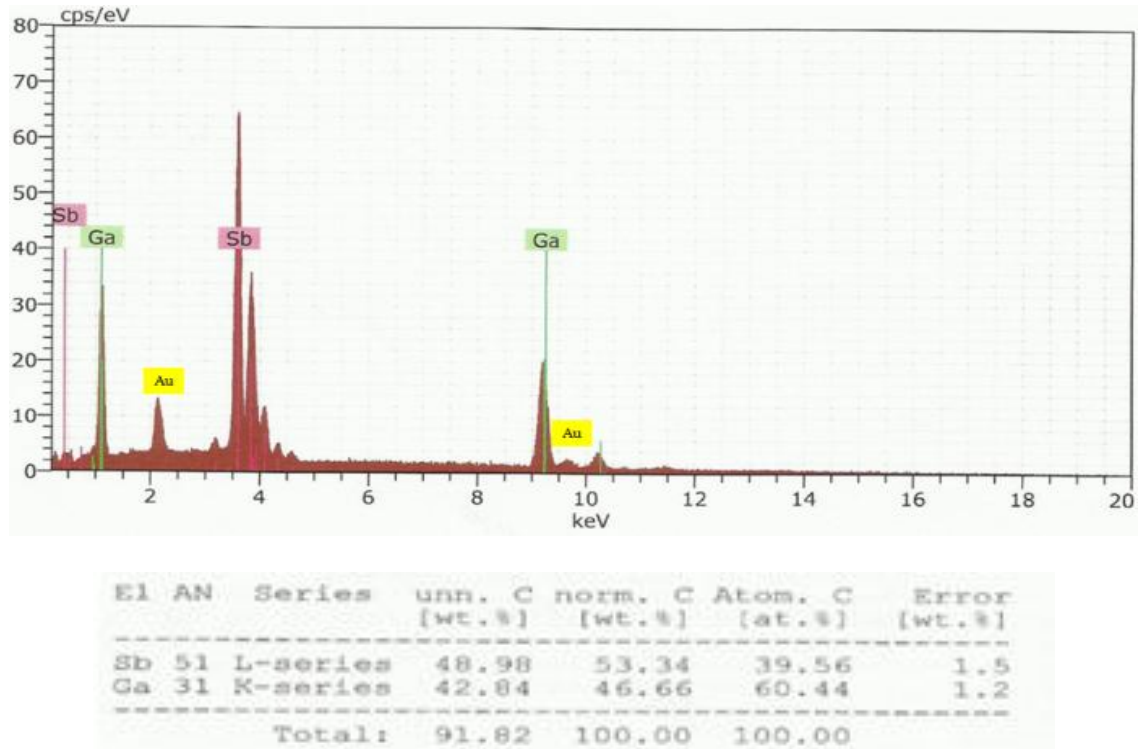


Fig. (3.2) EDXS pattern for bulk $Ga_{0.6}Sb_{0.4}$.

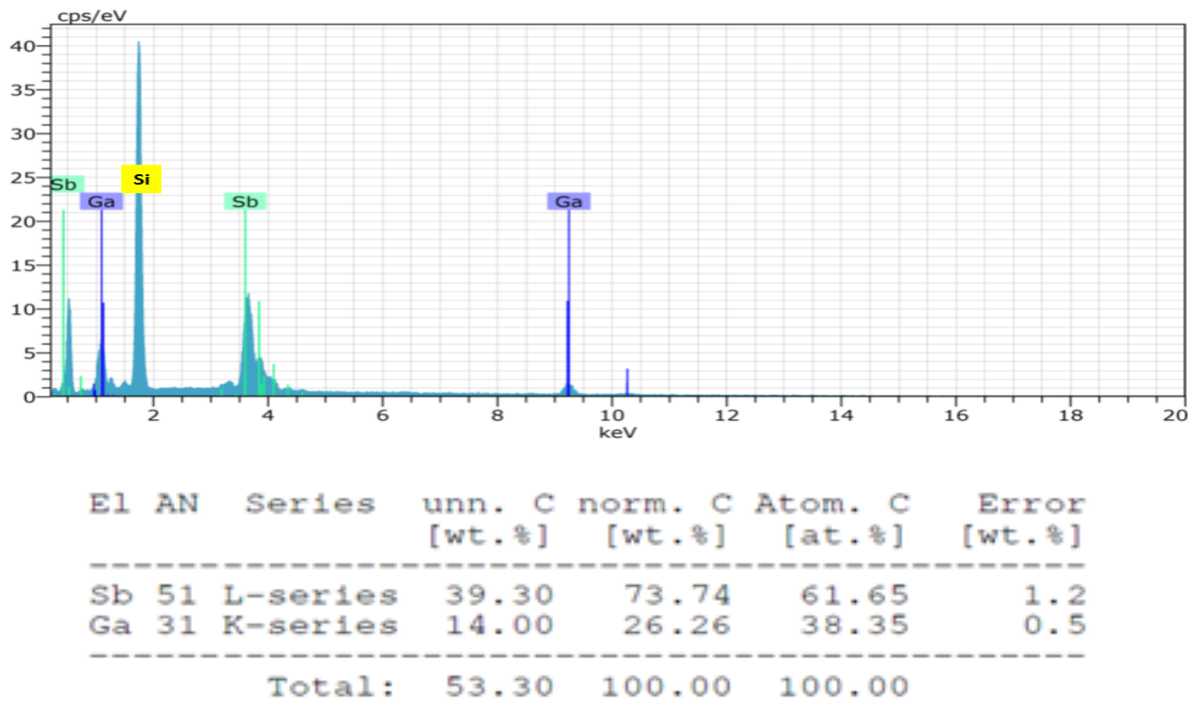
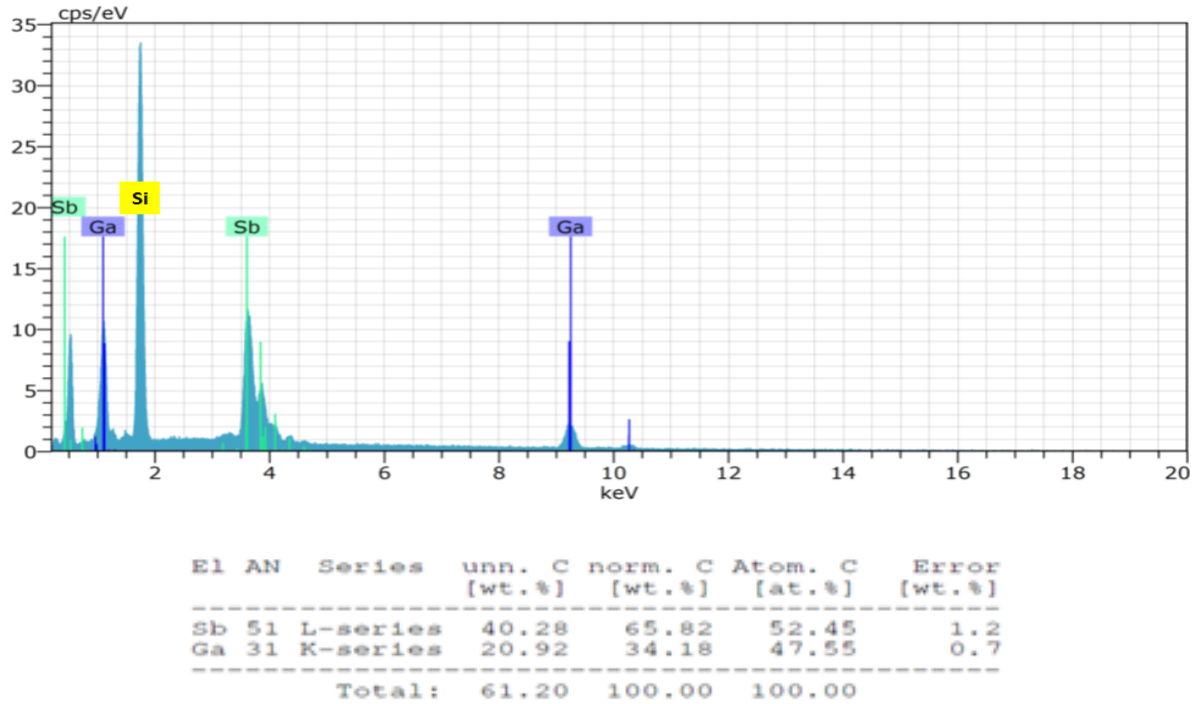
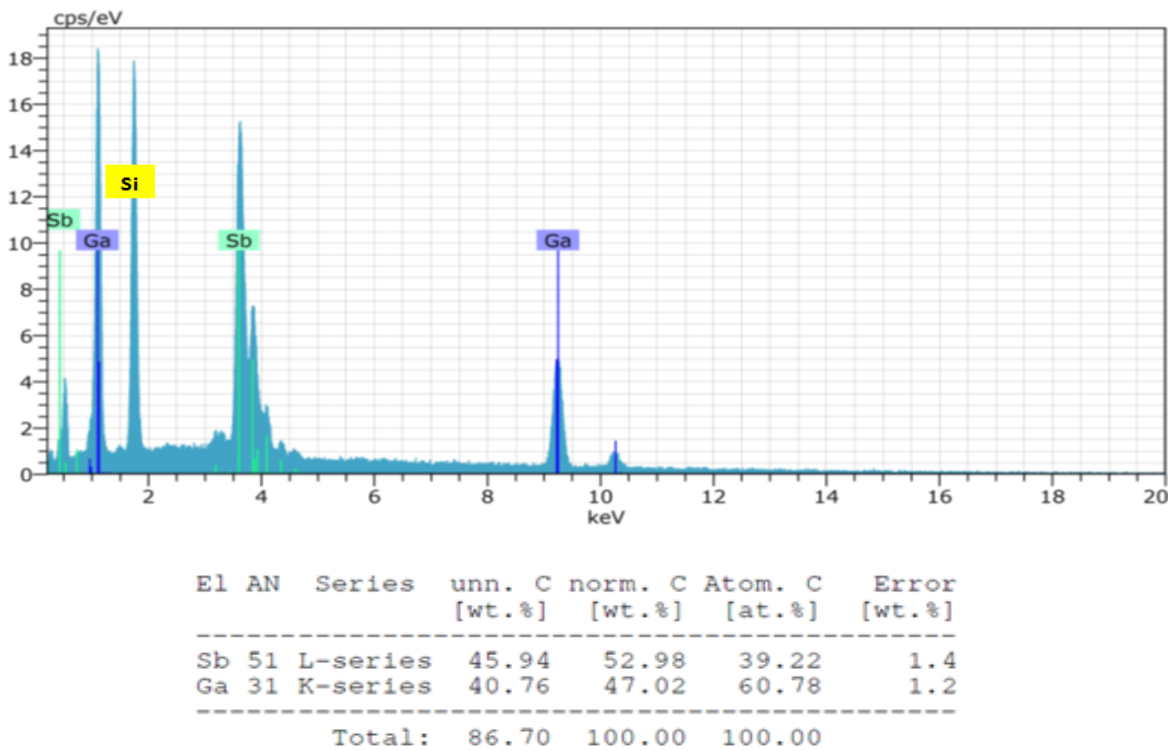


Fig.(3.3) EDXS pattern for $Ga_{0.4}Sb_{0.6}$ films.

Fig. (3.4) EDXS pattern for $\text{Ga}_{0.5}\text{Sb}_{0.5}$ films.Fig. (3.5) EDXS pattern for $\text{Ga}_{0.6}\text{Sb}_{0.4}$ films.

3.3 Structural Properties of $\text{Ga}_x\text{Sb}_{1-x}$ Alloys and Films

3.3.1 X-ray Diffraction Analysis (XRD)

Figures (3.6 - 3.18) reveal the XRD patterns of $\text{Ga}_x\text{Sb}_{1-x}$ alloys and thin films with different Ga content ($x=0.4, 0.5$ and 0.6) deposited at different substrate temperatures (348, 398, 448 and 473 K) and thicknesses (200, 300 and 400 nm) respectively.

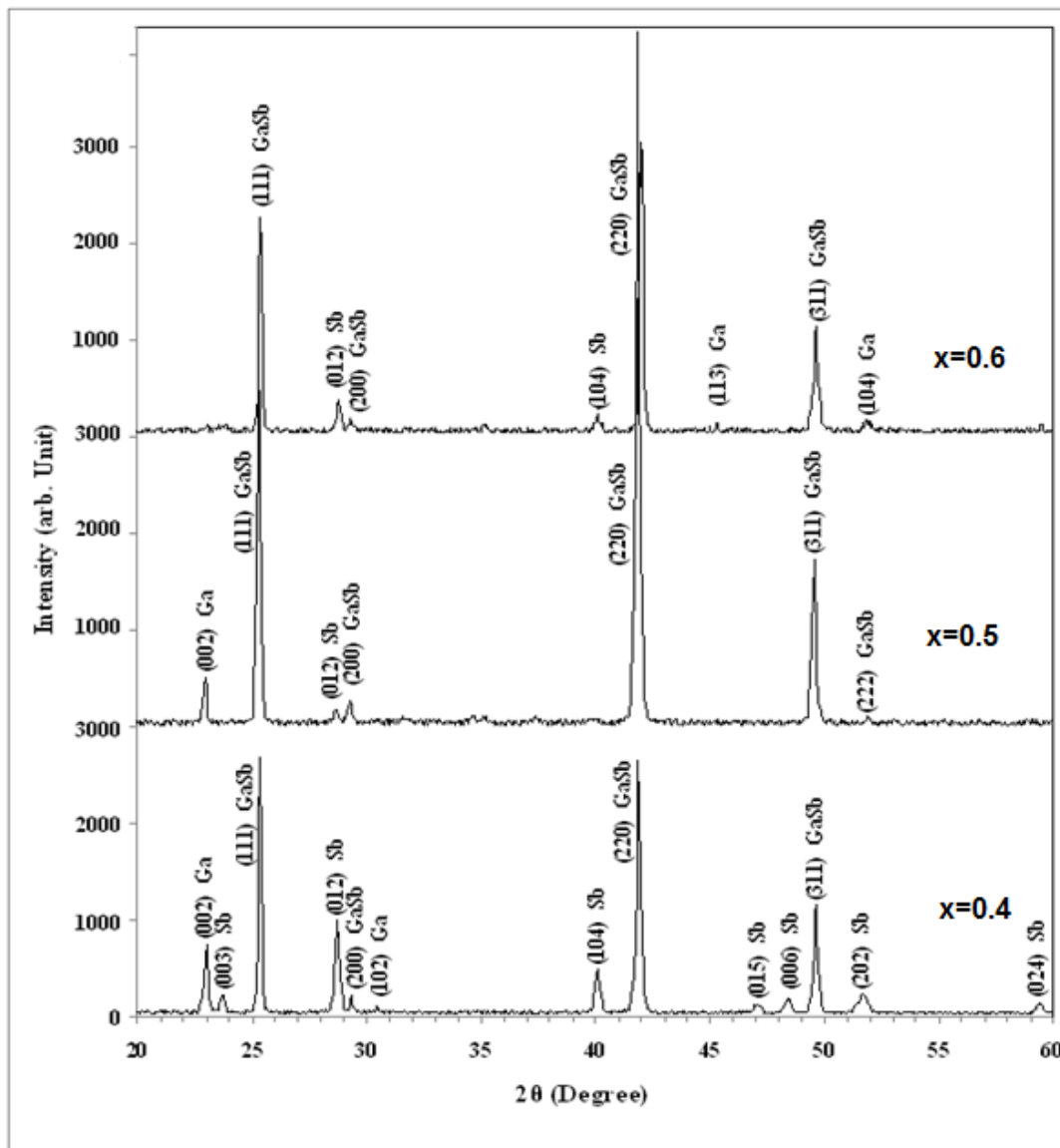


Fig.(3.6) XRD patterns for $\text{Ga}_x\text{Sb}_{1-x}$ alloys at different Ga percentage.

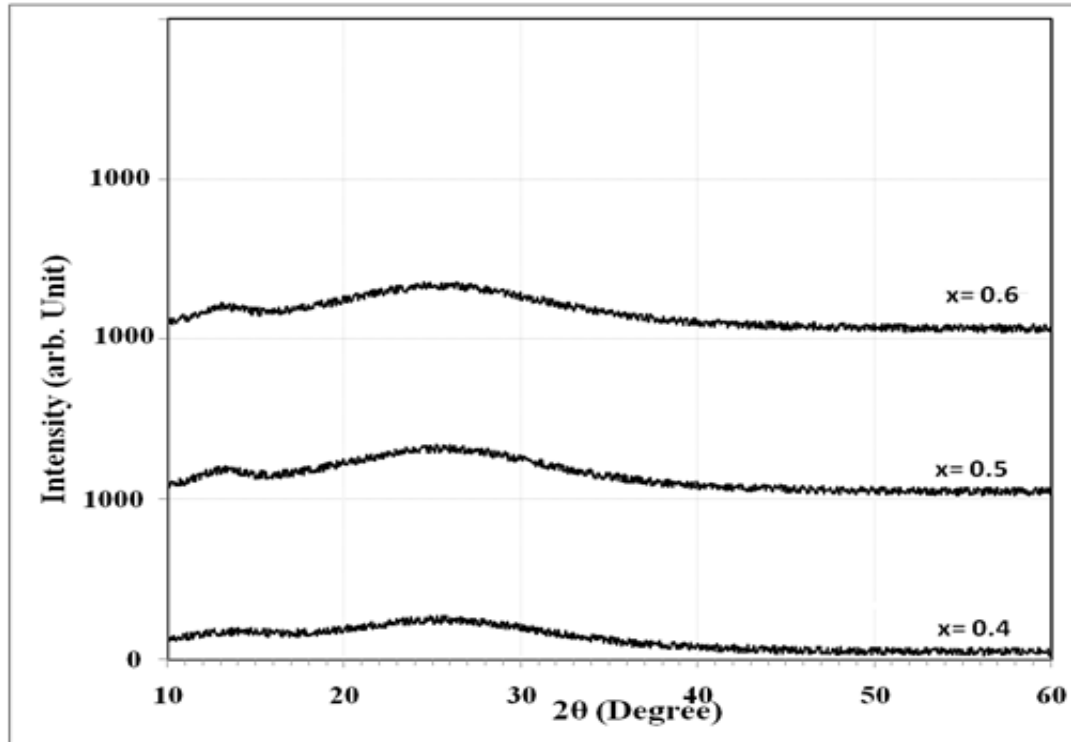


Fig. (3.7) XRD patterns for Ga_xSb_{1-x} films at T_s=348 K, of 200 nm thickness and different Ga content.

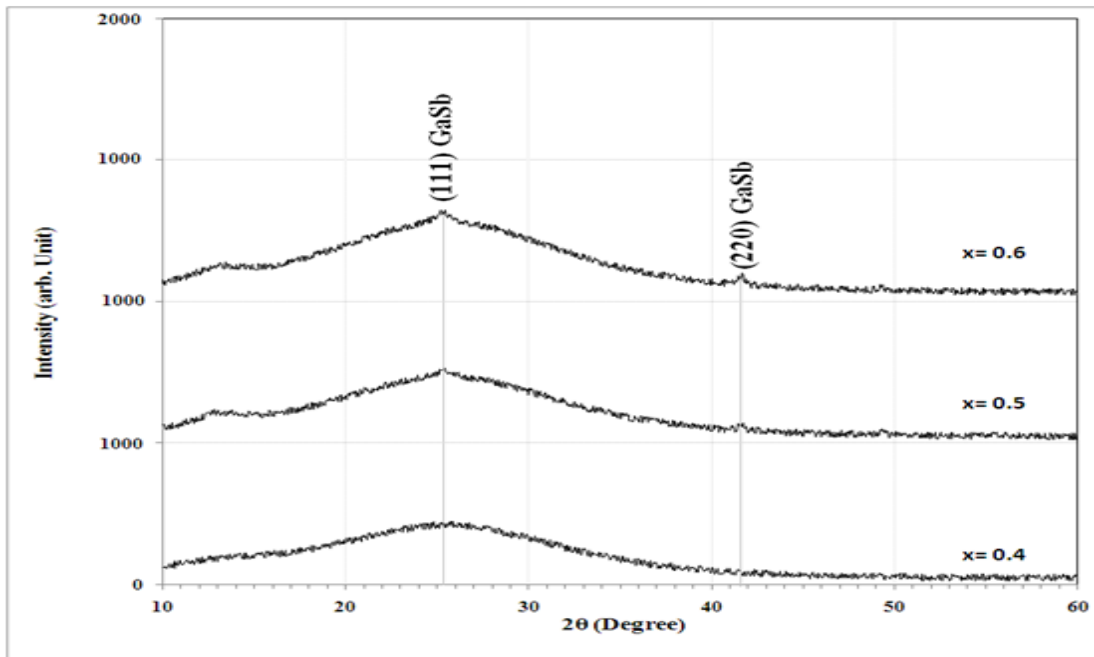


Fig. (3.8) XRD patterns for Ga_xSb_{1-x} films at T_s=348 K, of 300 nm thickness and different Ga content.

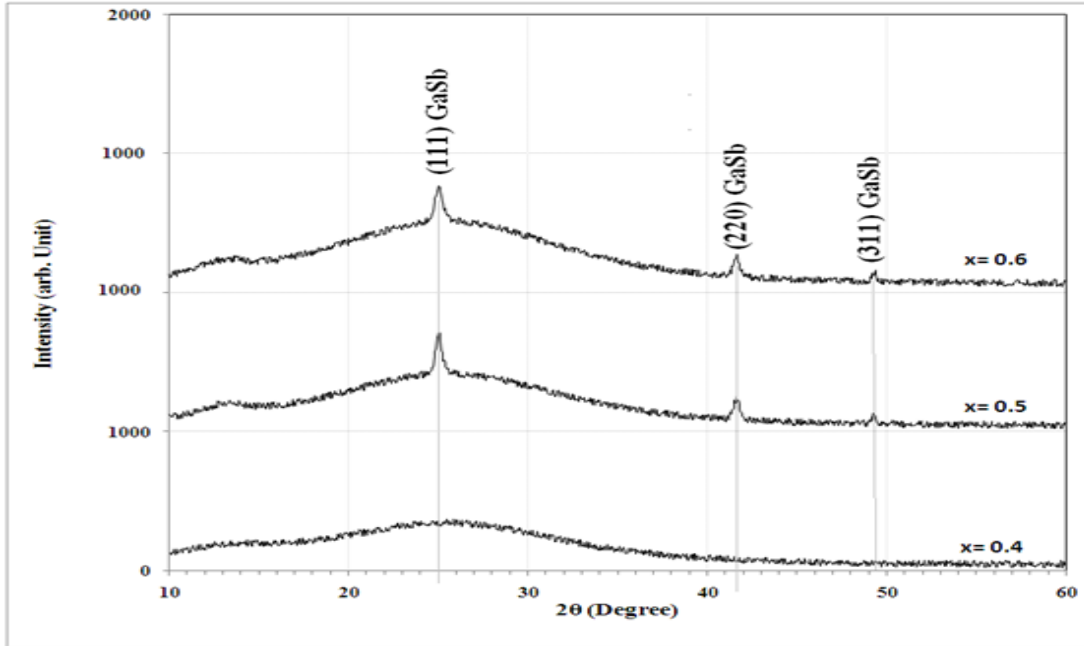


Fig. (3.9) XRD patterns for Ga_xSb_{1-x} films at T_s=348 K, 400 nm thickness and different Ga content.

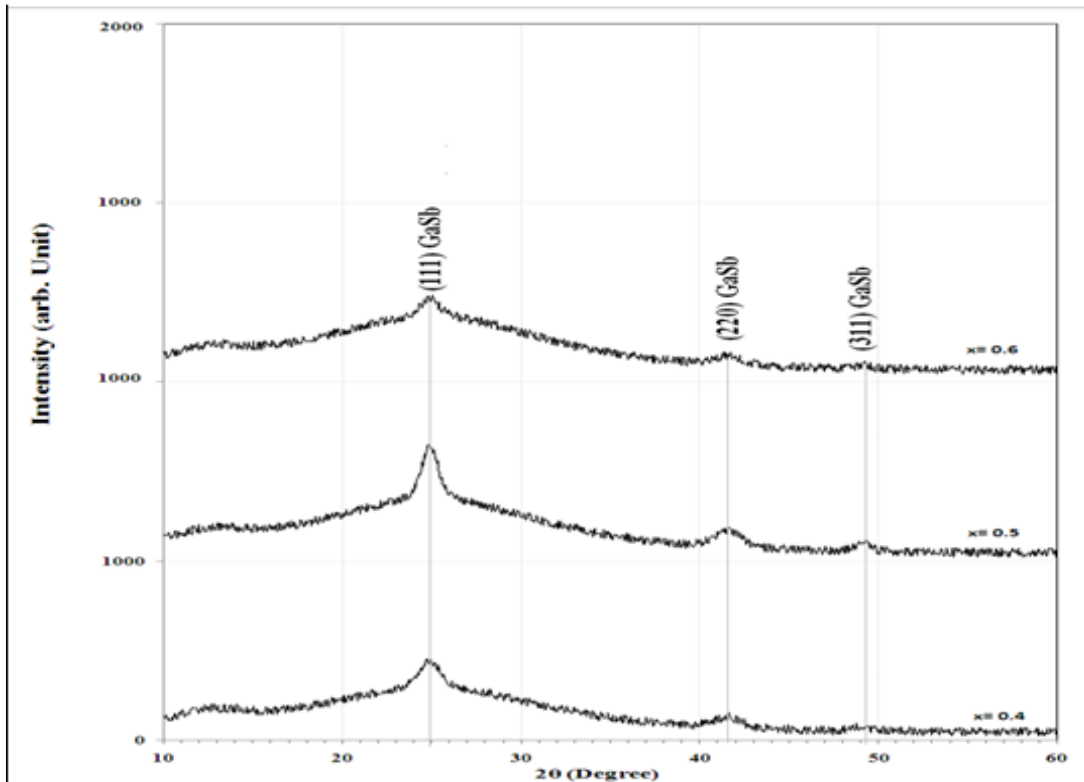


Fig. (3.10) XRD patterns for Ga_xSb_{1-x} films at T_s= 398 K, 200 nm thickness and different Ga content.

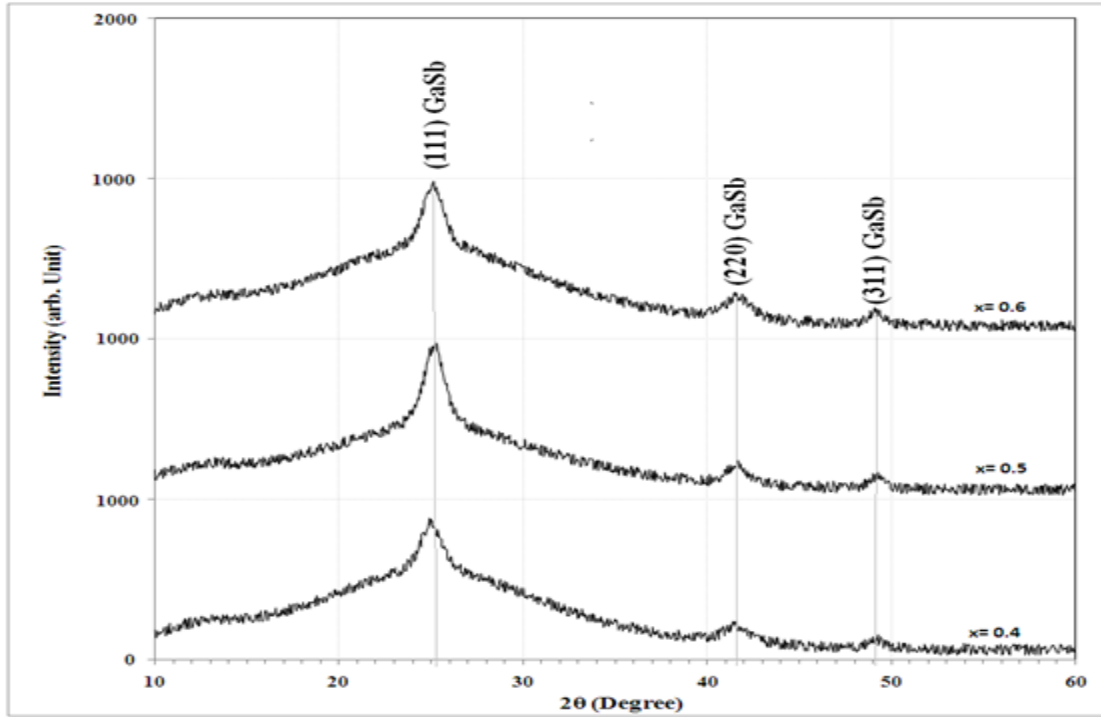


Fig. (3.11) XRD patterns for Ga_xSb_{1-x} films at T_s = 398 K, 300 nm thickness and different Ga content.

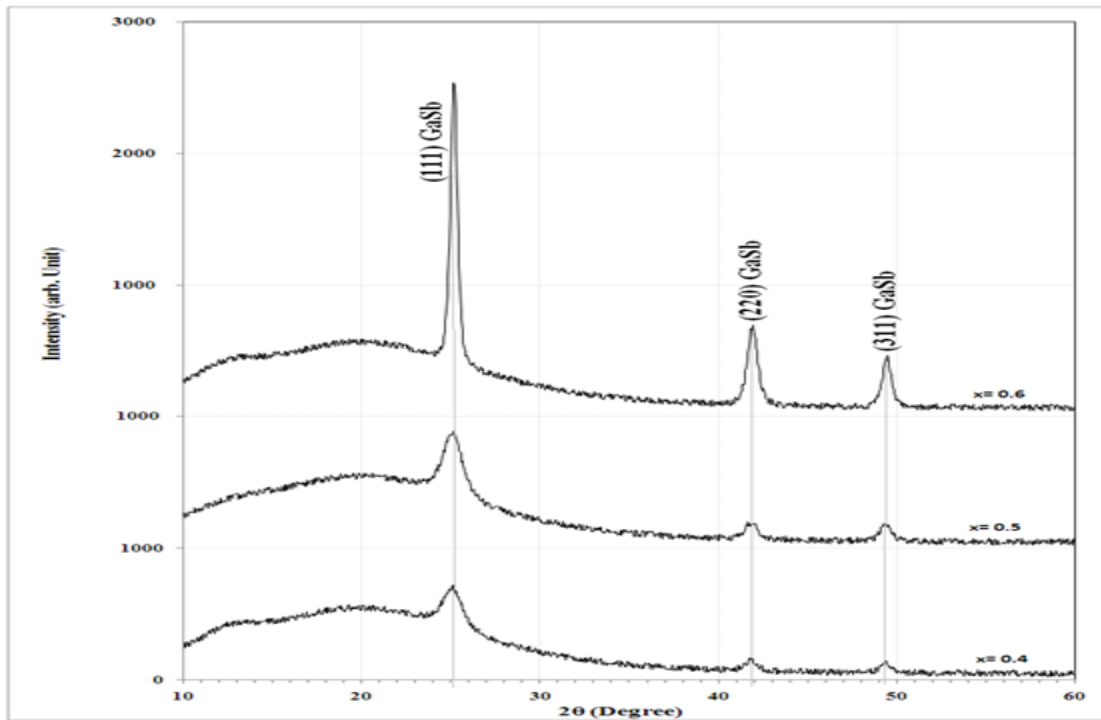


Fig. (3.12) XRD patterns for Ga_xSb_{1-x} films at T_s = 398 K, 400 nm thickness and different Ga content.

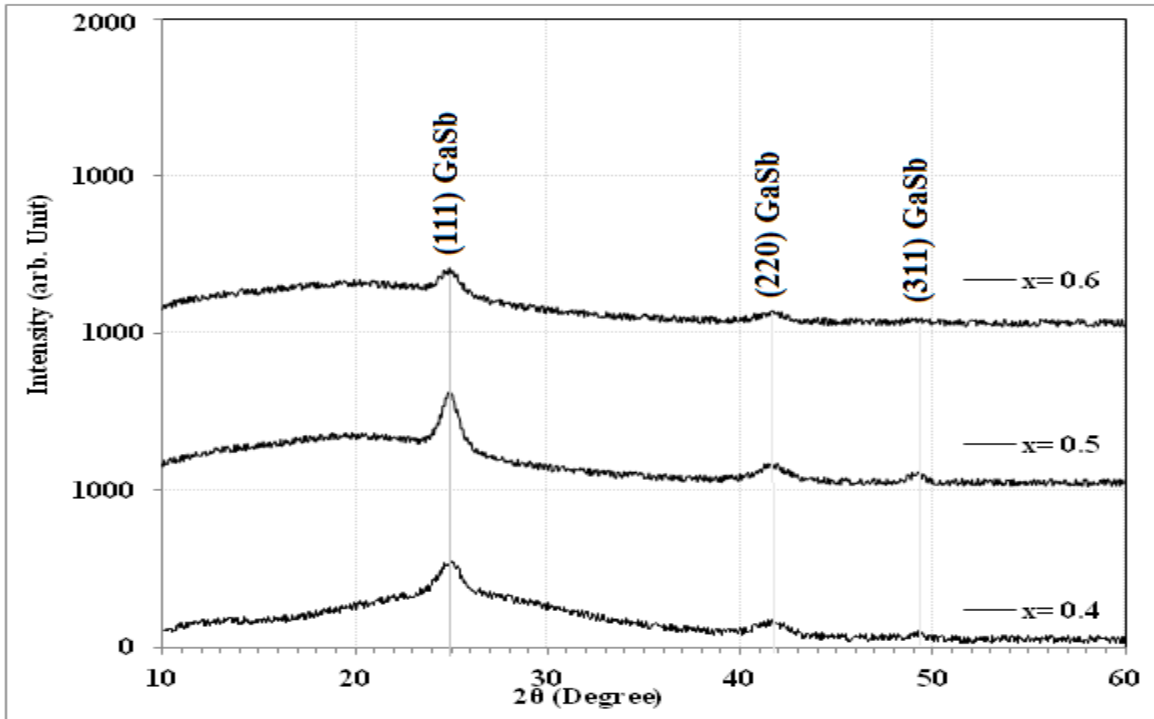


Fig. (3.13) XRD patterns for Ga_xSb_{1-x} films at T_s = 448 K, 200 nm thickness and different Ga content.

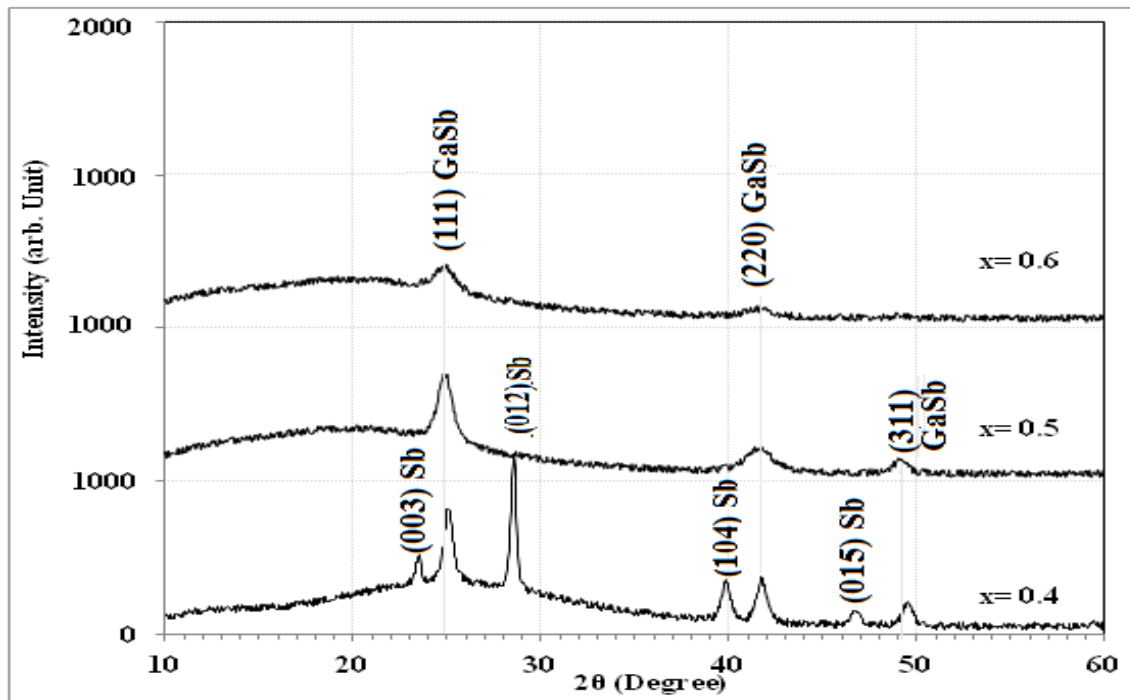


Fig. (3.14) XRD patterns for Ga_xSb_{1-x} films at T_s = 448 K, 300 nm thickness and different Ga content.

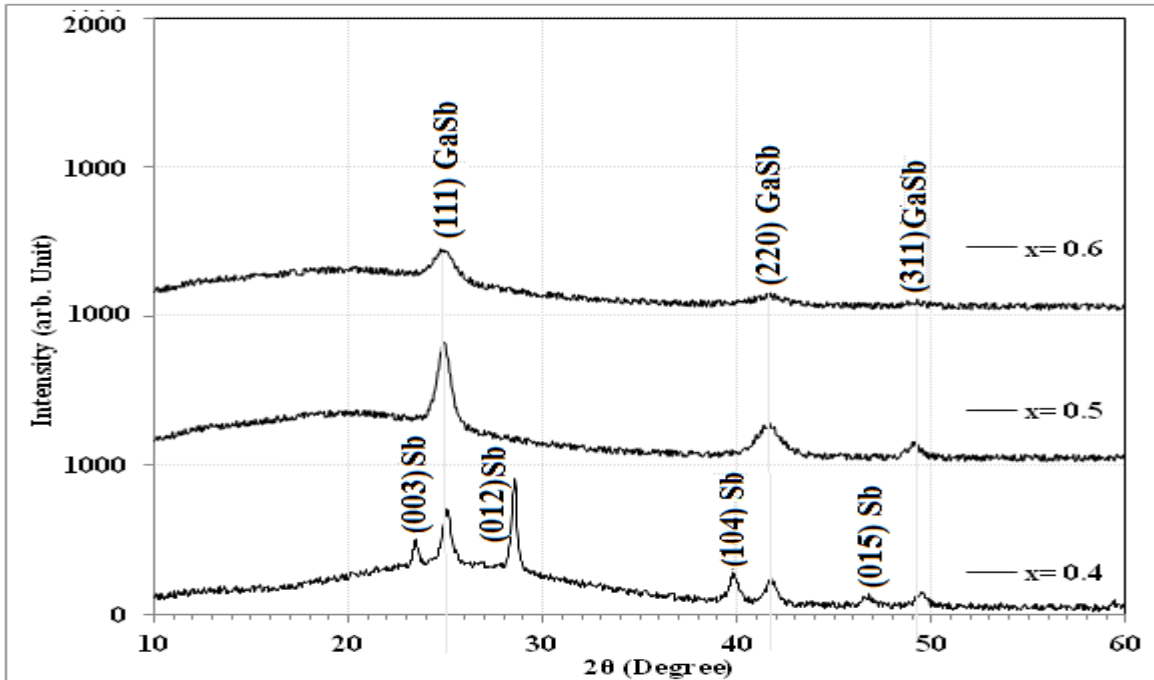


Fig. (3.15) XRD patterns for Ga_xSb_{1-x} films at $T_s=448$ K, 400 nm thickness and different Ga content.

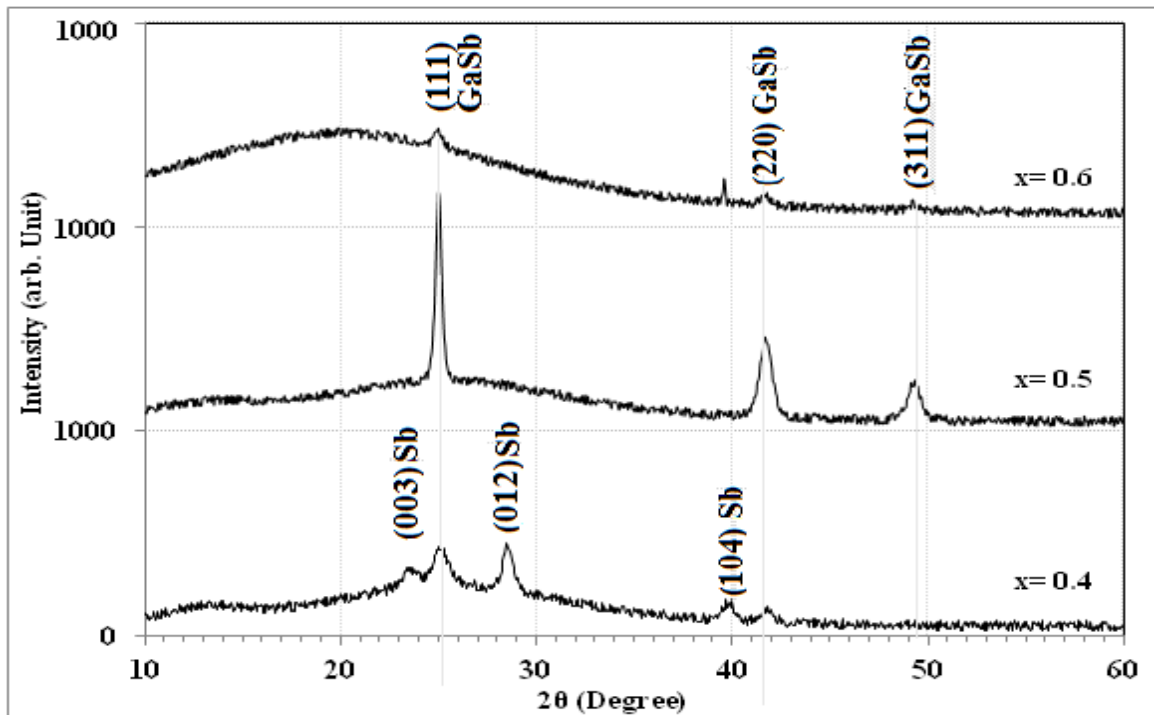


Fig. (3.16) XRD patterns for Ga_xSb_{1-x} films at $T_s=473$ K, 200 nm thickness and different Ga content.

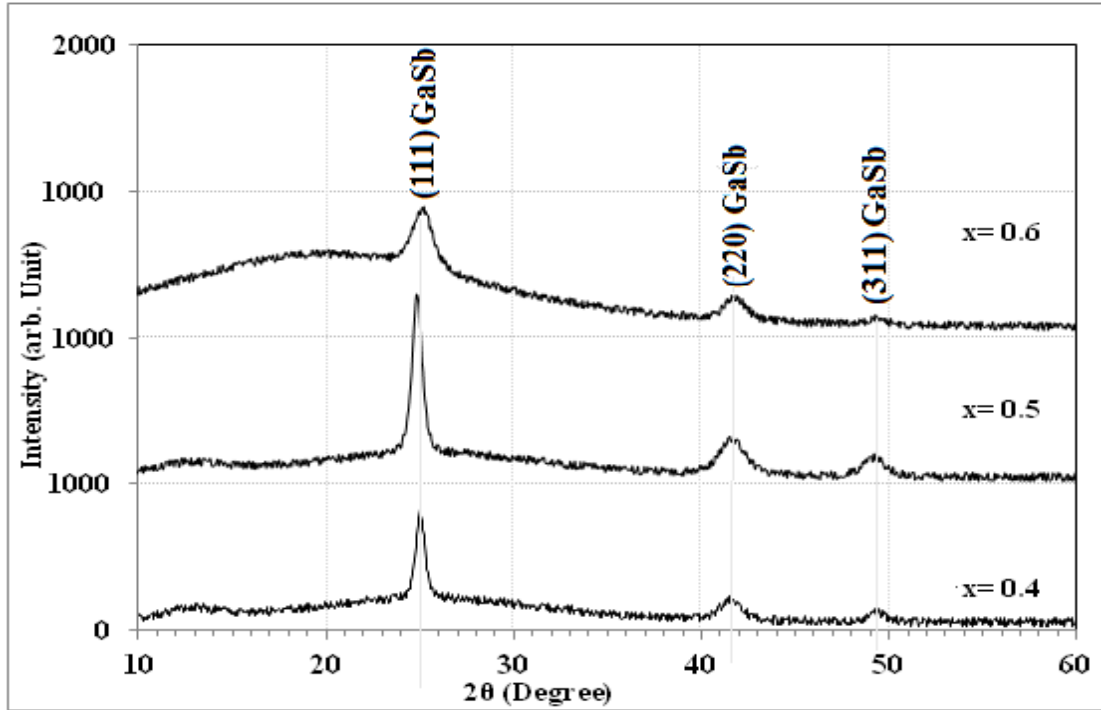


Fig. (3.17) XRD patterns for Ga_xSb_{1-x} films at T_s = 473 K, 300 nm thickness and different Ga content.

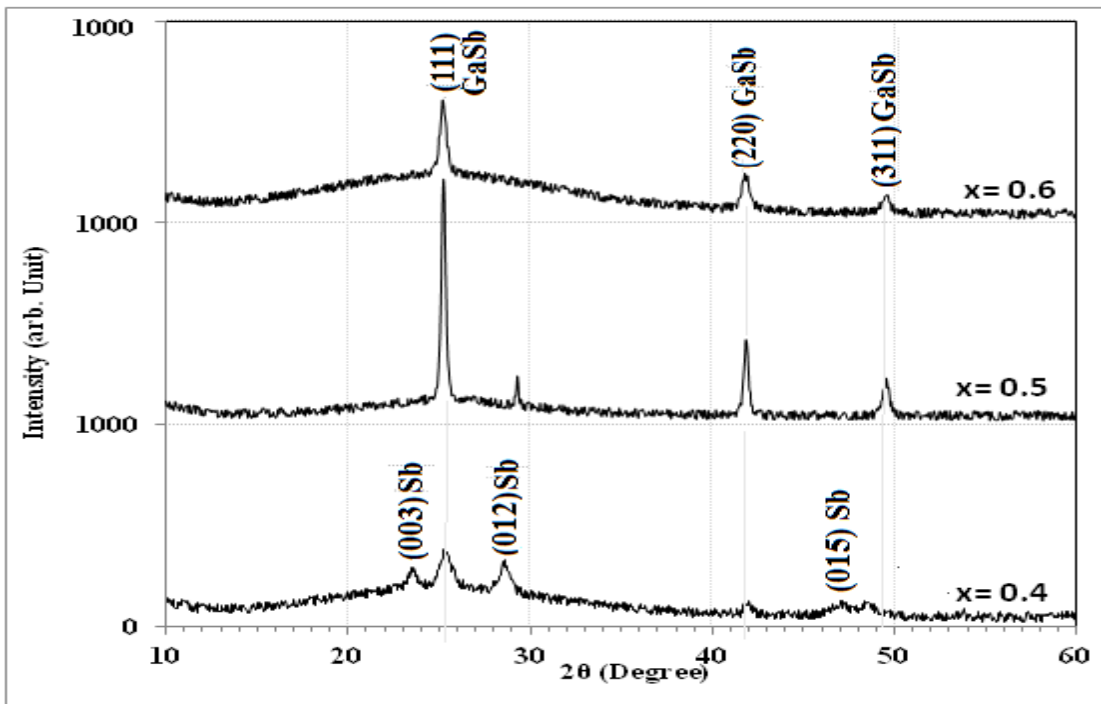


Fig. (3.18) XRD patterns for Ga_xSb_{1-x} films at T_s = 473 K, 400 nm thickness and different Ga content.

The XRD patterns are recorded in the range of $2\theta = 10\text{--}60^\circ$ using $\text{CuK}\alpha$ radiation. In general a polycrystalline structures were presented for all prepared alloys while amorphous and polycrystalline structures were presented for thin films. The thin films are dominated by three principal orientations: (111), (220) and (311). For $\text{Ga}_x\text{Sb}_{1-x}$ alloys the XRD pattern show that the zinc blend structure with preferential orientation is (220) for all values of Ga content. Also one can observe that there are another peaks at various 2θ belongs to Ga or Sb as shown in Fig. (3.6).

X-ray peaks in most of $\text{Ga}_x\text{Sb}_{1-x}$ thin films indicate that the vacuum-deposited films are nearly polycrystalline in nature. Table (3.1) lists the observed d-values with standard (JCPDS- ICDD file No. 07-0215), d-values for GaSb bulk and films. The observed d-values are in good agreement with the standard values for the zinc blend structure. In the XRD patterns for these films, the X-ray peak corresponding to (111), (220) and (331) reflections are observed in most patterns. It indicates that preferred orientation lies along (111) direction in vacuum-deposited GaSb films. This dominant orientation in the (111) direction is also reported for coevaporated GaSb thin films by Qiao Zaixiang et al.[66].

Table(3.1) Parameters of XRD Spectra for $\text{Ga}_x\text{Sb}_{1-x}$ alloys and films of $T_S=473\text{ K}$ and $t=400\text{ nm}$.

x	$2\theta^\circ_{\text{standard}}$	$d_{\text{standard}} \text{ \AA}$	$2\theta^\circ_{\text{exp}}$	$d_{\text{exp}} \text{ \AA}$	$\Delta(2\theta)^\circ$	hkl	$a_0 \text{ \AA}$
$\text{Ga}_x\text{Sb}_{1-x}$ alloys							
0.4	25.281	3.520	25.366	3.508	0.157	111	6.076
	29.277	3.048	28.776	3.099	0.179	200	6.199
	41.866	2.156	41.957	2.151	0.154	220	6.085
	49.554	1.838	49.646	1.834	0.156	311	6.085

0.5	25.281	3.520	25.338	3.512	0.137	111	6.083
	41.866	2.156	41.929	2.152	0.114	220	6.089
	49.554	1.838	49.598	1.836	0.129	311	6.090
0.6	25.281	3.520	25.401	3.503	0.143	111	6.068
	29.277	3.048	28.812	3.096	0.190	200	6.192
	41.866	2.156	42.029	2.148	0.155	220	6.075
	49.554	1.838	49.657	1.834	0.155	311	6.084
$\text{Ga}_x\text{Sb}_{1-x}$ films							
0.4	25.281	3.520	25.244	3.525	1.237	111	6.105
	29.277	3.048	28.682	3.109	0.725	200	6.219
	41.866	2.156	42.020	2.148	0.925	220	6.076
	49.554	1.838	47.954	1.895	1.150	311	6.286
0.5	25.281	3.520	25.352	3.510	0.646	111	6.080
0.6	25.281	3.520	25.273	3.521	0.445	111	6.098
	41.866	2.156	41.969	2.150	0.540	220	6.083
	49.554	1.838	49.570	1.837	0.383	311	6.094

Another noticeable remark from Figs.(3.7-3.9) is that when the thickness increased, the films became more crystalline at each substrate temperatures and Ga percentages, except for film $\text{Ga}_{0.4}\text{Sb}_{0.6}$ deposited at 348 K, the structure remain amorphous. X-ray pattern of $\text{Ga}_{0.5}\text{Sb}_{0.5}$ thin films shows they are the best in crystallinity because they are stoichiometric.

3.3.2 SEM Analysis

The grain size (grain diameter) l_1 and grain boundary l_2 of the $\text{Ga}_x\text{Sb}_{1-x}$ films have been studied by using the SEM micrographs as shown in Fig.(3.19).

A polycrystalline film with uniform and homogenous distribution of grain size was clearly observed. GaSb films deposited at 348 K on glass substrate Fig.(3.19 a). Fig.(3.19 b) shows image of $\text{Ga}_x\text{Sb}_{1-x}$ deposited at 398 K. One notices no adsorbed colloidal pentides as indicated by a presence of white boulders on the film surface. There was also difference in grain sizes with their uniformity distributed all over the film surface. An elevation in substrate temperature caused an enlargement in average grain size of $\text{Ga}_x\text{Sb}_{1-x}$ thin film and the film becomes more homogenous as depicted in Fig.(3.19) and there is many cracks in this sample. Fig.(3.20) shows the grain size increased with increasing film thickness and substrate temperatures. This behaviour is an agreement with Al-Douri et. al[68]. The grain size increased about two to four times with increasing T_s for various thicknesses of films. Its values increased about five times with increasing thickness from 200 to 400 nm for each T_s as shown in Fig. (3.20). It increased about two times with the increase of gallium content as shown in Fig. (3.21). The grain boundary (l_2) decreased about seven times with increasing of substrate temperatures for $\text{Ga}_{0.4}\text{Sb}_{0.6}$ film with thickness equal to 400 nm as shown in Fig.(3.22) while for $\text{Ga}_{0.6}\text{Sb}_{0.4}$ film with thickness equal to 400 nm the grain boundary increased about two times as shown in Fig.(3.23), this may be interpreted in term that Ga ratio which increase the liquid phase of $\text{Ga}_{0.6}\text{Sb}_{0.4}$.

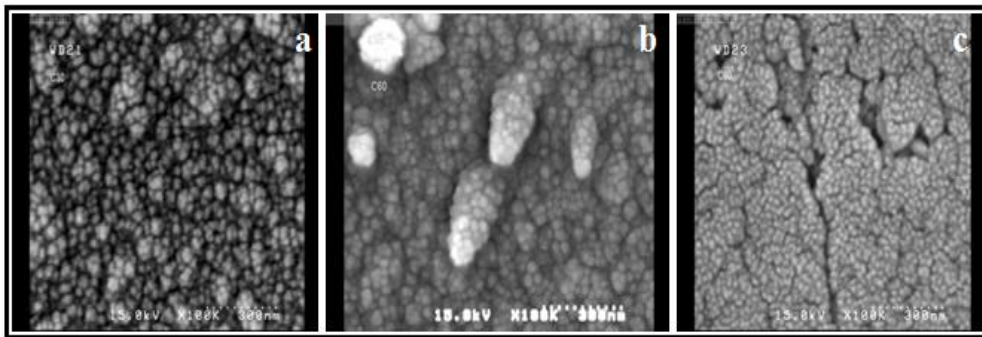


Fig.(3.19) SEM images of $\text{Ga}_x\text{Sb}_{1-x}$ films deposited on soda lime substrates at (a) 348K (b)398K (c)448K.

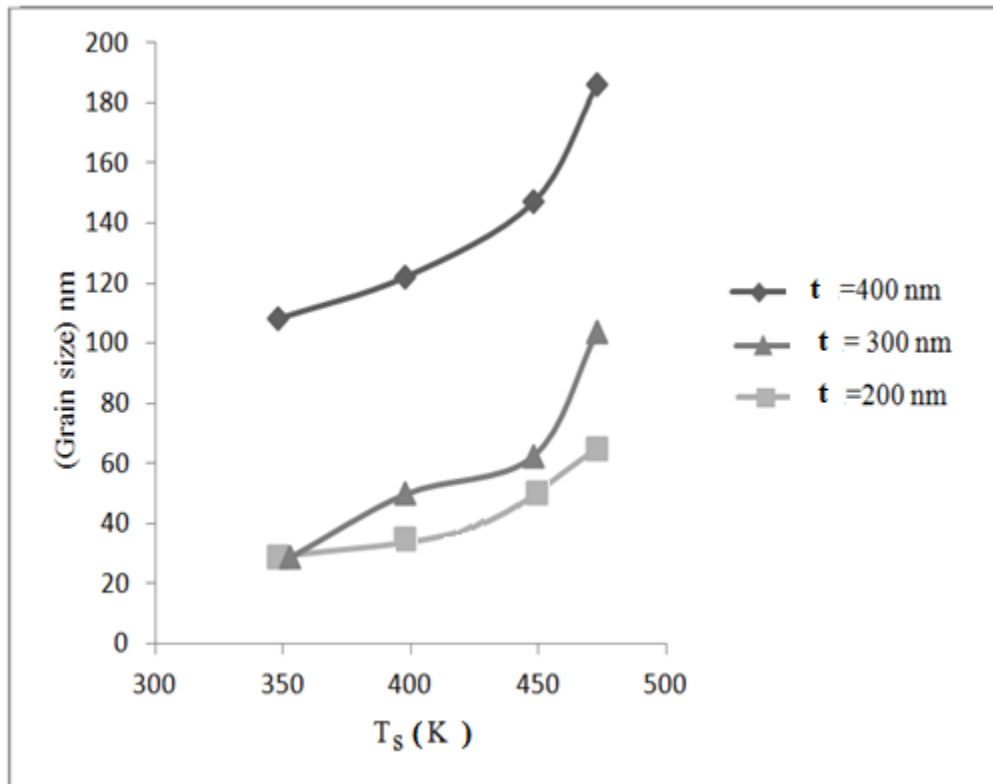


Fig. (3.20) Dependence of grain size on T_s and t for $Ga_{0.5}Sb_{0.5}$ films.

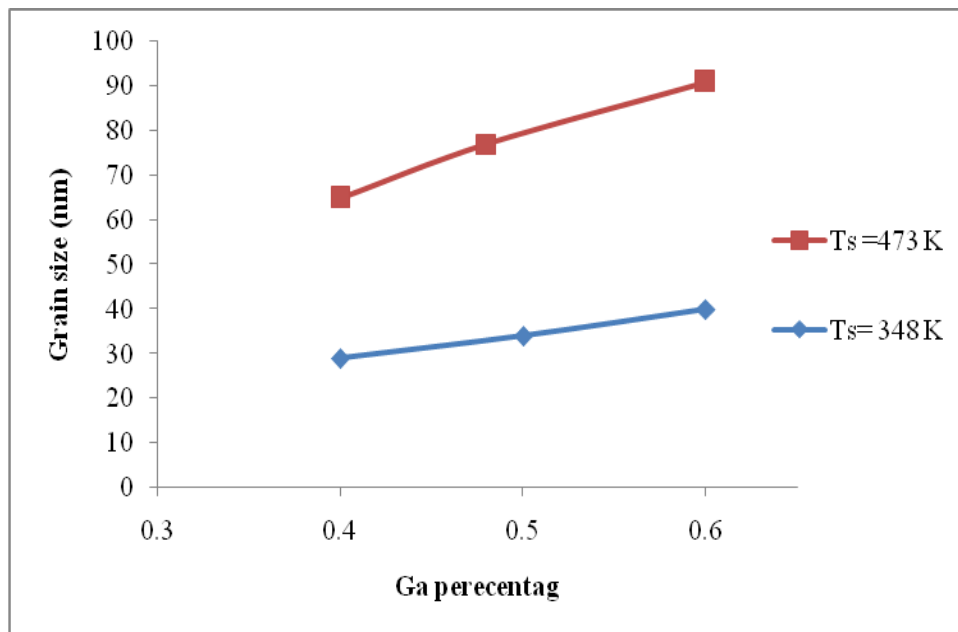


Fig.(3.21)Dependence of grain size with gallium percentage and substrate temperature for Ga_xSb_{1-x} film with $t=200$ nm.

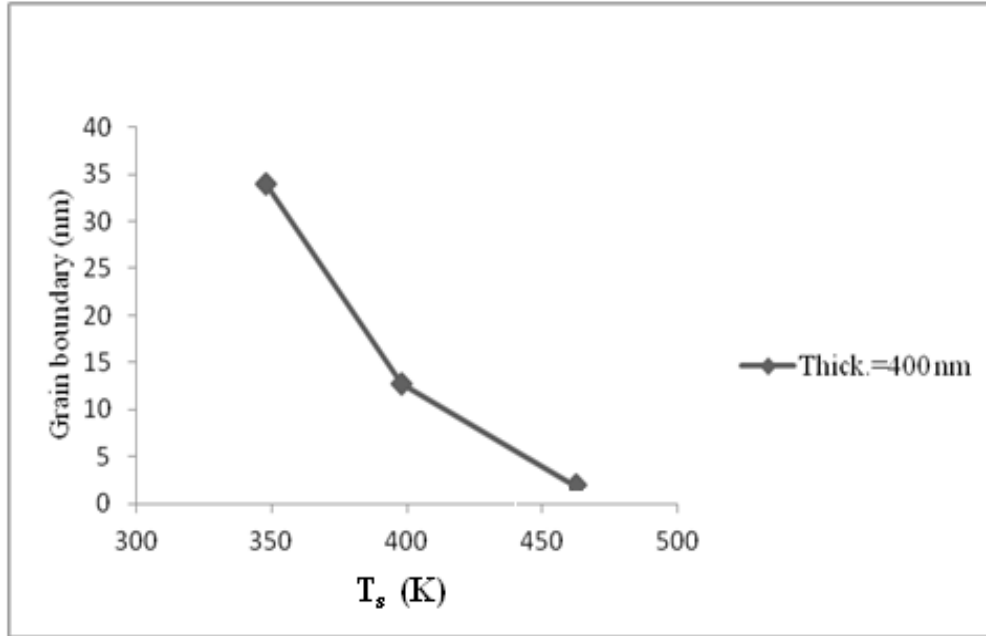


Fig. (3.22) Dependence of grain boundary on substrate temperature for $\text{Ga}_{0.4}\text{Sb}_{0.6}$ film with $t=400$ nm.

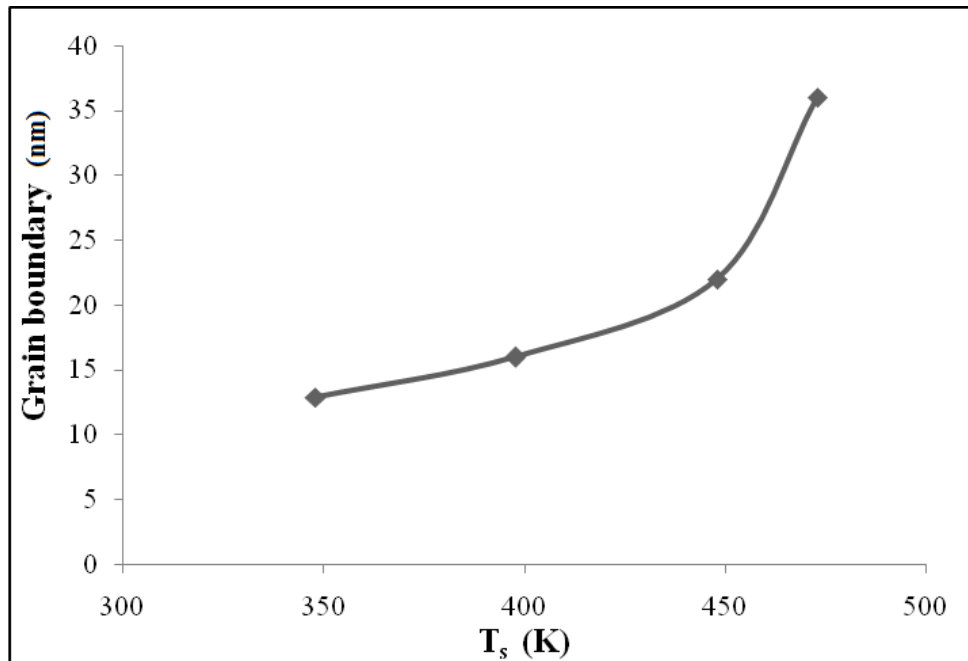


Fig.(3.23) Dependence of grain boundary on substrate temperature for $\text{Ga}_{0.6}\text{Sb}_{0.4}$ film at $t=400$ nm.

3.4 Electrical Properties of $\text{Ga}_x\text{Sb}_{1-x}$ Films

The electrical properties of $\text{Ga}_x\text{Sb}_{1-x}$ films deposited on glass substrates, which involve D.C conductivity, Hall effect and I-V characteristics were investigated as a function of substrate temperatures, percentages of (Ga, Sb) and thickness.

3.4.1 Ohmic Contact

Aluminum was deposited as electrodes on $\text{Ga}_x\text{Sb}_{1-x}$ thin films deposited at 473 K with thickness 200 nm as shown in Fig.(3.24). It is clear that the contact between the aluminum electrodes and $\text{Ga}_x\text{Sb}_{1-x}$ thin films was an ohmic contact.

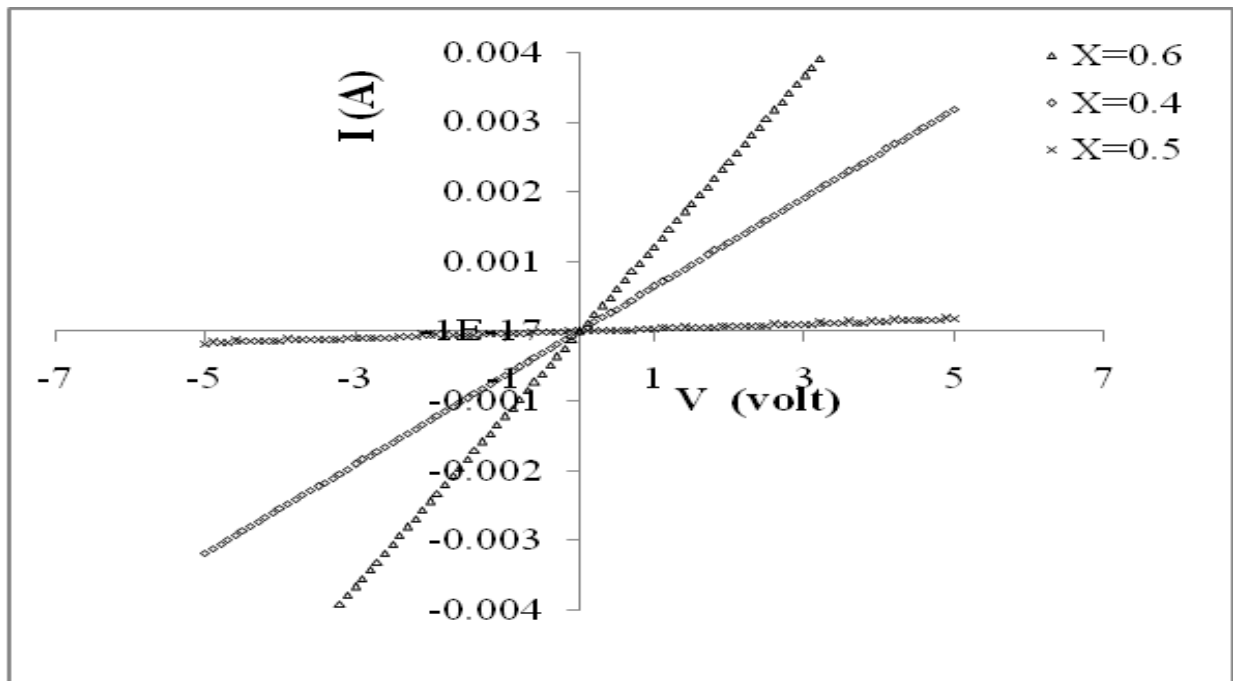


Fig.(3.24) I-V curve for $\text{Ga}_x\text{Sb}_{1-x}$ films deposited at $T_s=473$ K, $t=200$ nm.

3.4.2 D.C Electrical Conductivity

The plot of $\ln\sigma_{d.c}$ for $\text{Ga}_x\text{Sb}_{1-x}$ films as a function of $10^3/T$ at different substrate temperatures, percentages of (Ga, Sb) and thickness were investigated.

Fig.(3.25) shows the variation of $\ln\sigma_{d.c}$ with $10^3/T$ for $\text{Ga}_{0.5}\text{Sb}_{0.5}$ films deposited at T_s (348,398 and 473) K for 400 nm thickness.

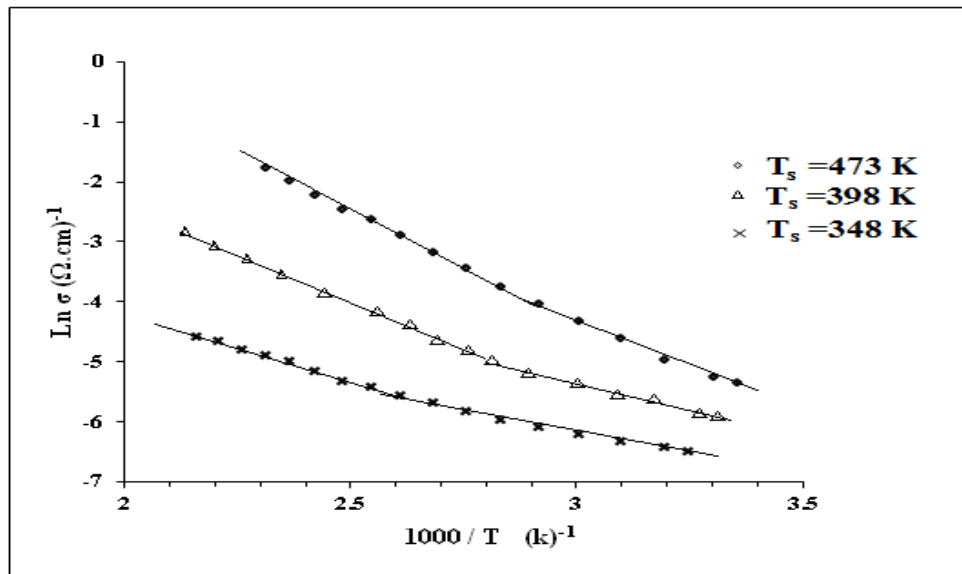


Fig.(3.25) $\ln \sigma_{d.c}$ versus $1000/T$ for $\text{Ga}_{0.5}\text{Sb}_{0.5}$ films at different T_s at thickness=400 nm

As shown in Fig. (3.25) the $\ln\sigma_{d.c}$ of the $\text{Ga}_{0.5}\text{Sb}_{0.5}$ films increases with increasing substrate temperatures (T_s). The observed low conductivity in low T_s films can be explained due to lower degree of crystallization and the small grain size. Also the conductivity decreases with decrease of gallium content (increase of antimony concentration) as shown in Fig.(3.26), i.e the access of Ga content may be reduce the density of states, and eliminate tails in the band gap and improve the structure of films. Fig.(3.27) shows that the resistivity of GaSb films increases with the increasing of grain boundary and decreases with increasing of grain size because of the reasons which mentioned above.

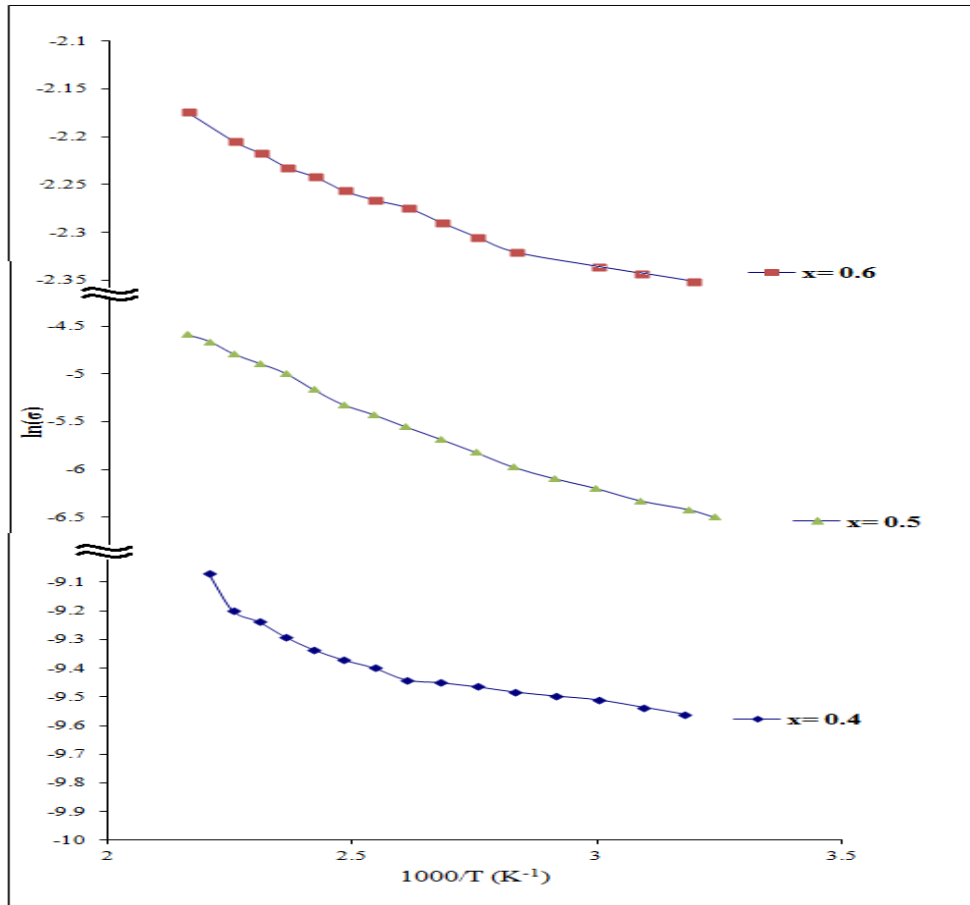


Fig. (3.26) $\text{Ln}\sigma_{d.c}$ versus $1000/T$ for $\text{Ga}_{0.4}\text{Sb}_{0.6}$ films at different Ga content deposited at $T_s=398$ K, $t=200$ nm.

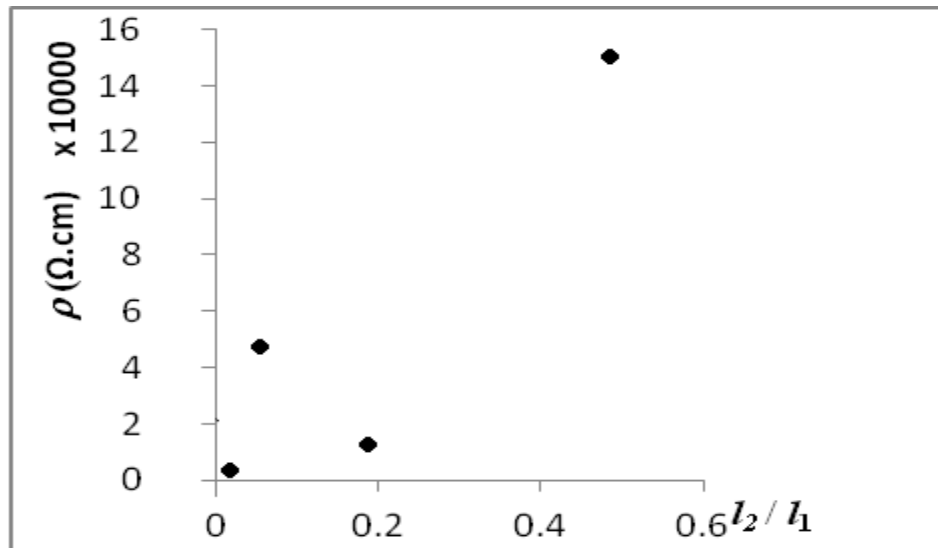


Fig.(3.27) Resistivity of GaSb films vs ratio of grain boundary to grain size.

It is clear from Fig.(3.25) that there are two transport mechanisms, giving rise to two activation energies E_{a1} and E_{a2} . The conduction mechanism of the activation energy (E_{a2}) at the higher temperatures range (400-473) K is due to carriers excitation into the extended states beyond the mobility edge, and at the lower range of temperatures (300-400) K, the conduction mechanism of the activation energy (E_{a1}) is due to carriers excitation into localized states of the edge of the band. The values of E_{a2} increase with increasing of substrates temperatures due to the elimination of some defects from the films and the improvement in crystallization during growth process as we observe in previous XRD analysis. We also observe that the values of E_{a2} decrease with increasing gallium percentage. All these behaviors and values are shown in Table (3.2) and (3.3). Our results are in agreement with Gheorghiu et al.[54].

Table (3.2) D.c. conductivity parameters for $Ga_{0.5}Sb_{0.5}$ films at different substrates temperatures and thickness 400nm.

x	T_s (K)	$\sigma_{d.c.R.T}$ ($\Omega.cm$)⁻¹	E_{a2} (eV)	Temp. Range (K)	n_H (cm⁻³)	μ (cm²/V.s)
0.5	348	1.5X10 ⁻³	0.195	400-473	3.98x10 ¹⁶	0.24
	448	2.5X10 ⁻³	0.26	400-473	3.68x10 ¹⁴	42.5
	473	5.3X10 ⁻³	0.38	400-473	1.21x10 ¹³	2729.5

Table (3.3) D.C. conductivity parameters for $\text{Ga}_x\text{Sb}_{1-x}$ films at substrates temperature 348K, different gallium percentages and thickness 200nm.

T_s (K)	x	$\sigma_{d.c.R.T}$ ($\Omega.\text{cm}$) ⁻¹	E_a (eV)	Temp. Range (K)	n_H (cm^{-3})	μ ($\text{cm}^2/\text{V.s}$)
348	0.4	6.9×10^{-5}	0.22	400-473	1.78×10^{15}	0.245
	0.5	1.5×10^{-3}	0.20	400-473	1.25×10^{14}	75
	0.6	8.7×10^{-2}	0.12	400-473	2.60×10^{15}	209

3.4 Hall Effect

The type of charge carriers, concentration (n_H), Hall mobility (μ_H) were measured using Hall measurement set up. We found that most of $\text{Ga}_{0.4}\text{Sb}_{0.6}$ films exhibits a negative Hall coefficient (n-type) while most of $\text{Ga}_{0.6}\text{Sb}_{0.4}$ films exhibits positive Hall coefficient (p-type). Undoped GaSb is always p-type, caused by the presence of unusually large native acceptor background as explained by Messias and Marega [69]. Dutta et. al.[70] have shown that the conductivity arise from a doubly ionizable native defect. At higher temperatures the mobility depends basically on the concentration of native defects, which are related with the growth conditions. So we think that the p-type conductivity of vacuum-deposited $\text{Ga}_{0.6}\text{Sb}_{0.4}$ films is normally attributed to the existence of excess Ga in the condensed films. The n_H and p_H were calculated by the equations (1.13-1.14). For films with 200 nm thickness we observed that the carries concentration increases with increase of substrate temperature due to improving the crystallization while for films with 400 nm thickness they decrease due to the defects and dislocations.

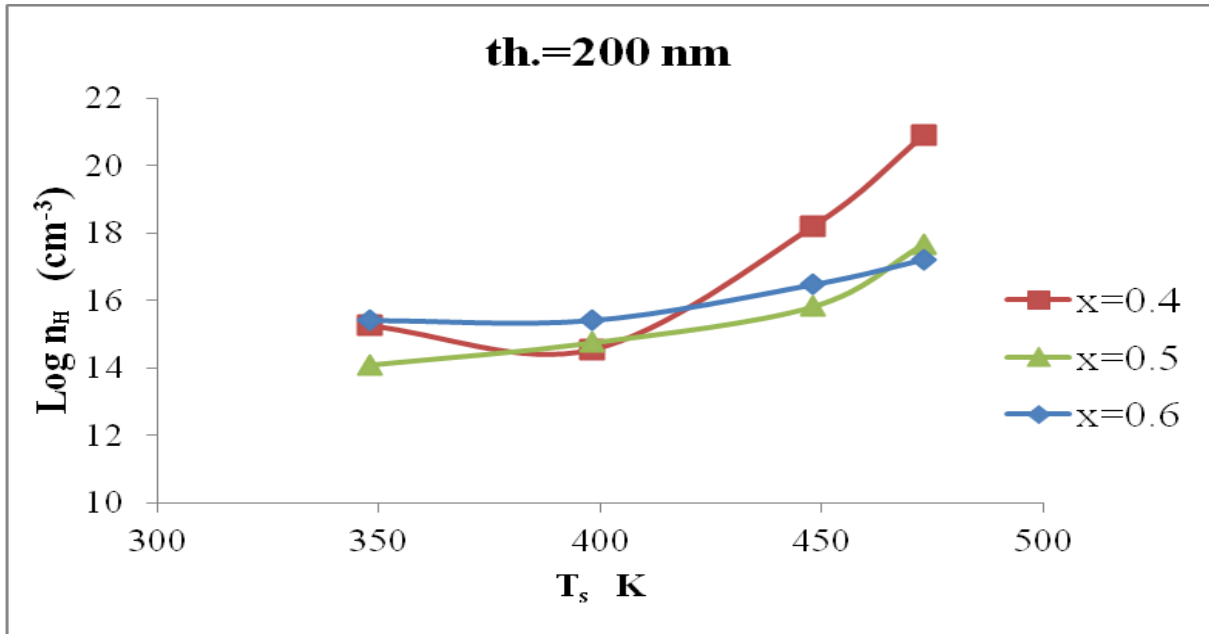


Fig.(3.28) Dependence of carriers concentration on substrate temperature for $\text{Ga}_x\text{Sb}_{1-x}$ film thickness 200nm.

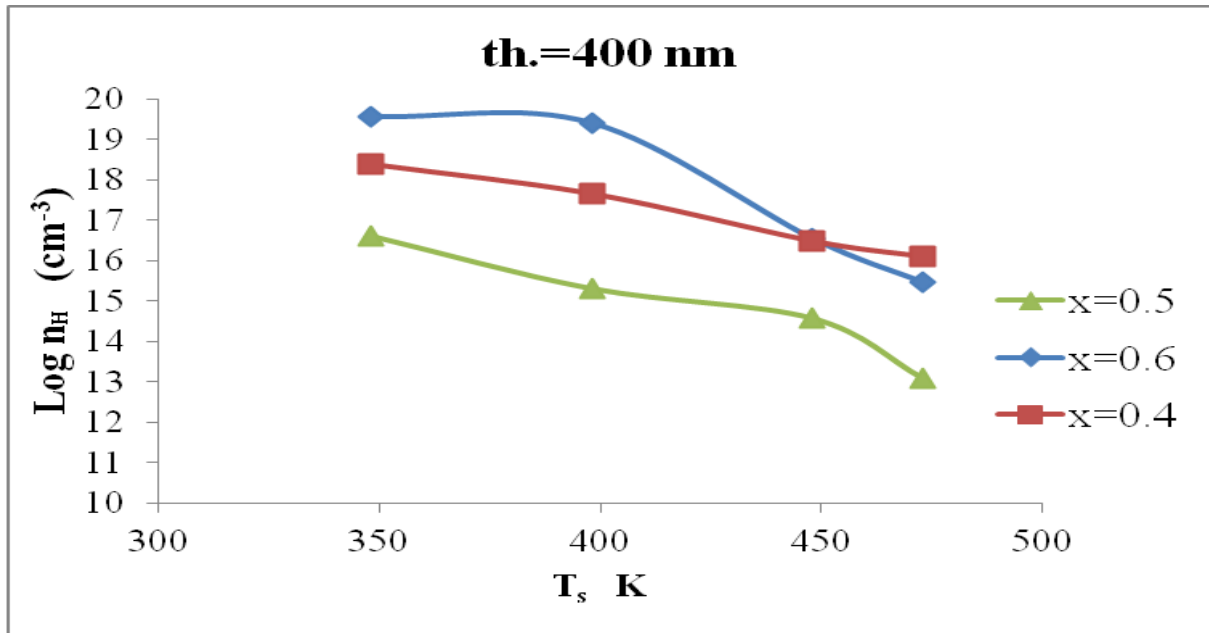


Fig.(3.29) Dependence of carriers concentration on substrate temperatures for $\text{Ga}_x\text{Sb}_{1-x}$ films thickness 400nm.

Also we notice that the mobility increases with increase of gallium percentage but it decreased with increasing of film thickness which attributed to increasing of cracks dislocations and defects as shown in Fig.(3.31).

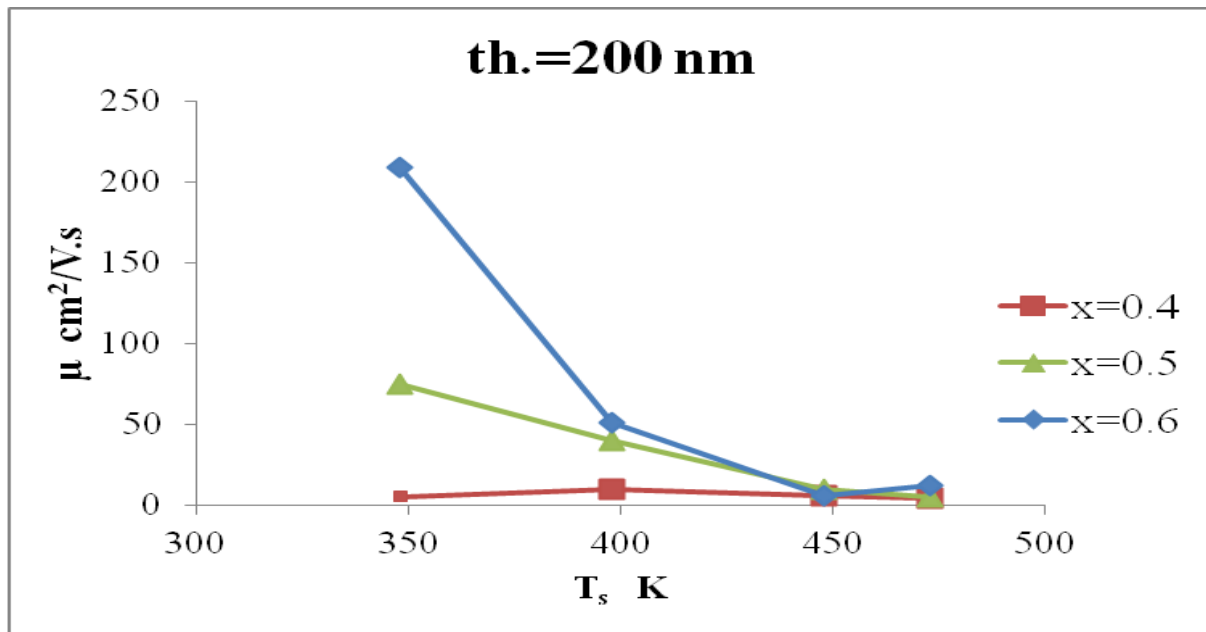


Fig.(3.30) Dependence of mobility on gallium content for different Ga_xSb_{1-x} films.

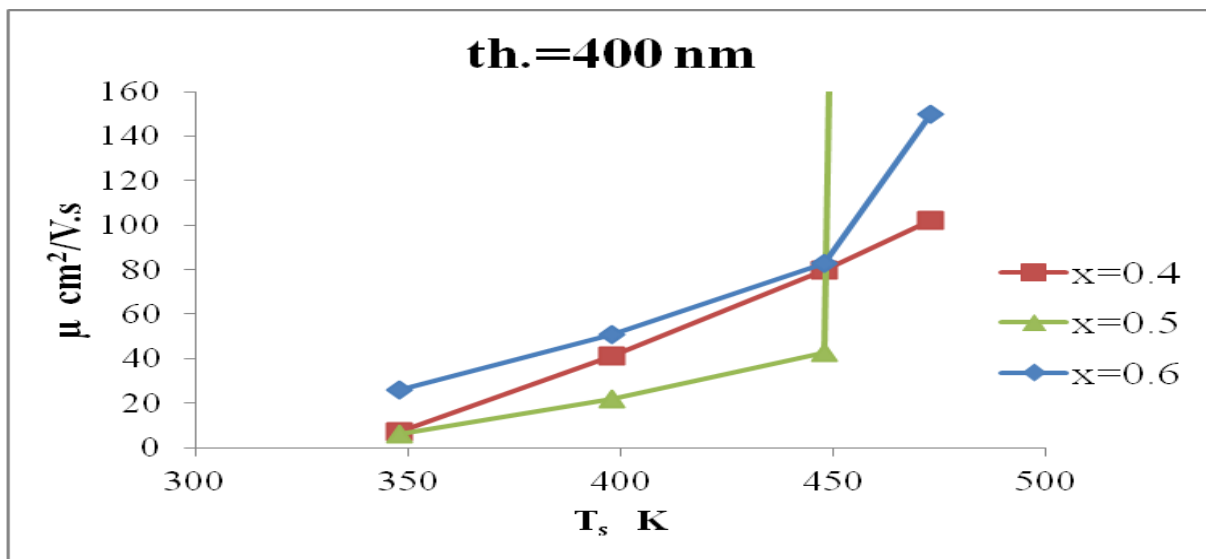


Fig.(3.31) Dependence of mobility on gallium content for Ga_xSb_{1-x} films at $T_s=348$ K.

The conductivity of most $\text{Ga}_x\text{Sb}_{1-x}$ films deposited at substrate temperature 348 K was n-type while it convert to p-type at $T_s=473$ K which is confirmed by Hall effect measurements.

The carriers concentration for $\text{Ga}_x\text{Sb}_{1-x}$ films increased with increasing of substrate temperatures and Ga percentage for films with thickness 200 nm as shown in Fig.(3.28) but it decreased for films had thickness 400 nm as shown in Fig.(3.29). This may be due to increase the defects with increasing of thickness, so that the carriers will decrease.

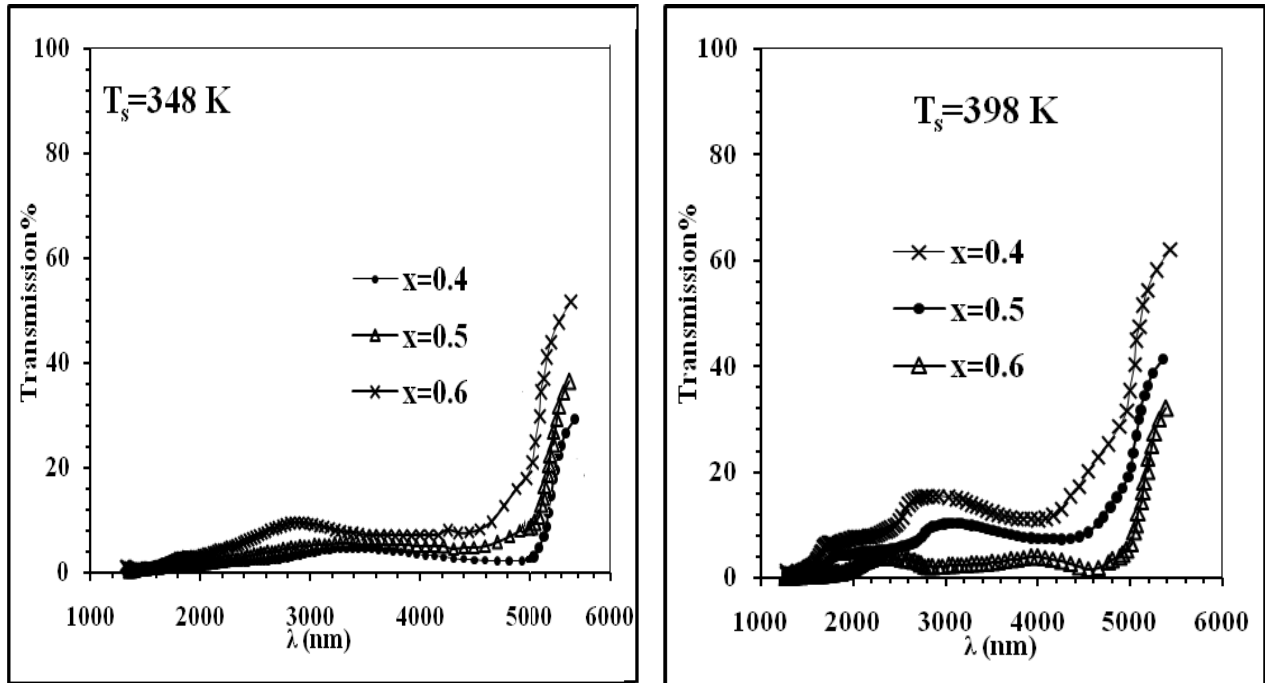
Hall mobility decreased with increasing T_s for films with 200 nm thickness, whereas it increased for films with thickness 400 nm which is due to the reasons mentioned above as shown in Figs. (3.30 and 3.31).

3.6 The Optical Properties

The optical properties of $\text{Ga}_x\text{Sb}_{1-x}$ films deposited on glass substrate at R.T. The samples with different substrate temperatures, gallium content and thicknesses have been investigated by using Fourier Transform Infrared (FTIR) transmittance spectrum in the region (1.25-5.0) μm . The transmittance and absorption coefficient spectrum have been studied. The optical energy gap E_g and the optical constants, which involves refractive index (n), extinction coefficient (k), real dielectric constant (ϵ_r) and imaginary dielectric constant (ϵ_i) also have been determined.

3.6.1 Transmittance Spectrum

The transmittance spectrum for $\text{Ga}_x\text{Sb}_{1-x}$ films prepared at different substrate temperatures (348,398,448 and 473 K), gallium content (0.4,0.5 and 0.6) and thicknesses 400 nm are shown in Fig. (3.32). It is obvious that the transmittance increases with increasing of substrate temperatures as shown in Table (3.4). This may be due to improving the crystallite size and decreasing the absorbance. The transmittance not systemically decreases with the increasing of film thickness because in the case of thicker film, more atoms are present in the film so more states will be available for the photons to be absorbed.



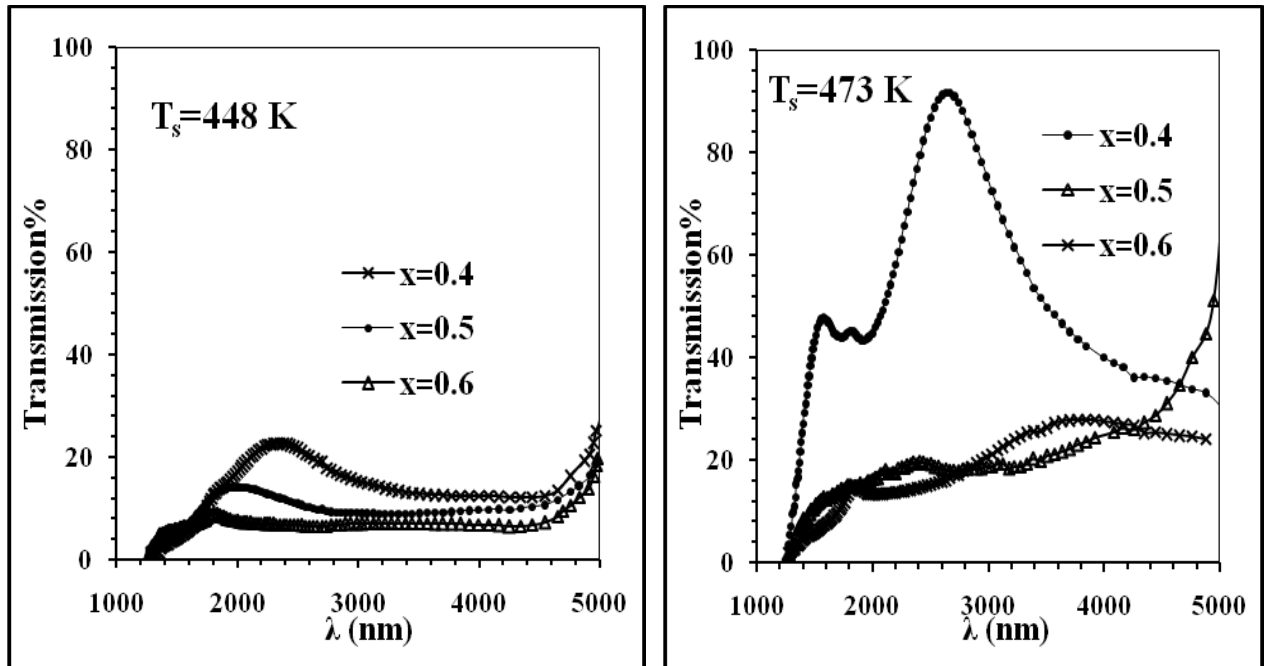


Figure (3.32) Transmittance spectra as a function of wavelength for $Ga_x Sb_{1-x}$ films at different x and T_s , $t=400$ nm.

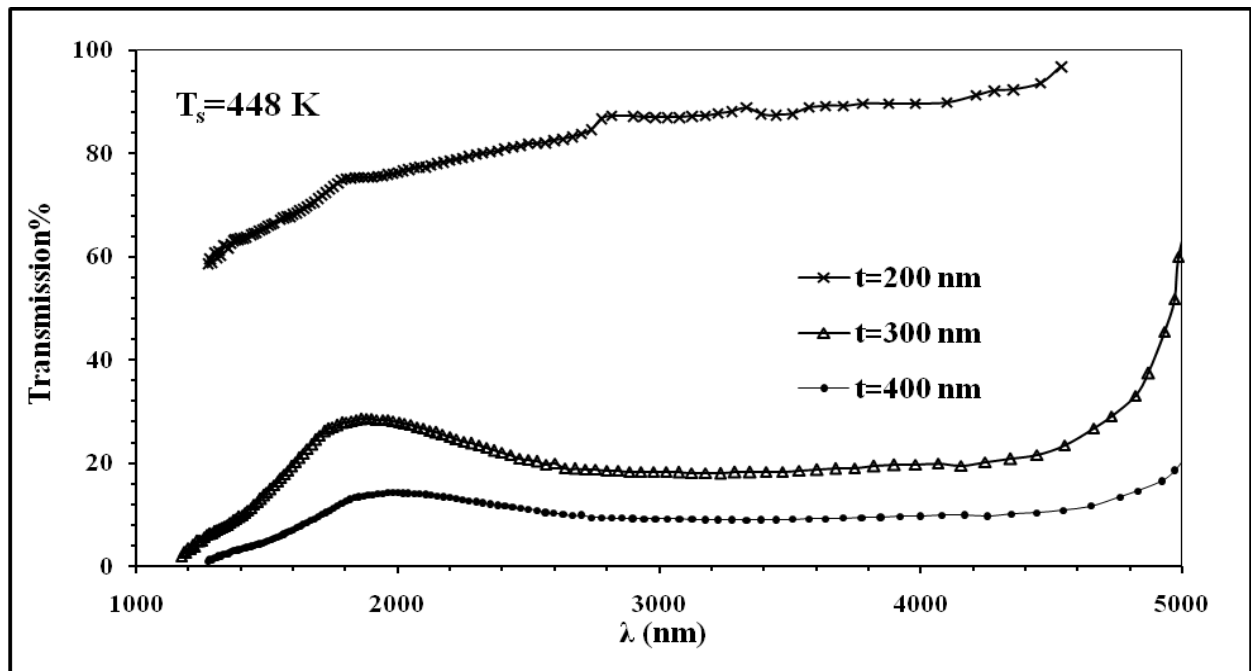
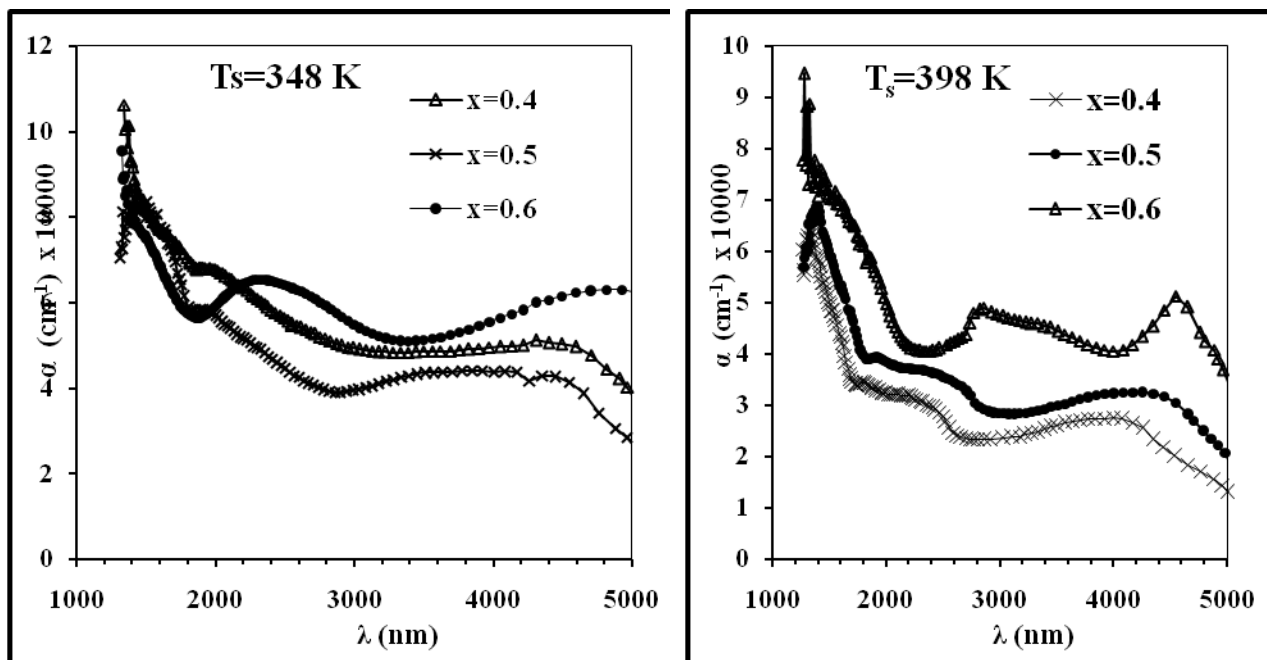


Figure (3-33) Transmittance spectrum as a function of wavelength for $Ga_{0.5} Sb_{0.5}$ films at different thicknesses.

3.6.2 The Absorption Coefficient

The absorption coefficient (α) was determined from the region of high absorption at the fundamental absorption edge of the film. The variation of the absorption coefficient versus the wavelength for different substrate temperatures (T_s) and different Ga percentages of the $\text{Ga}_x\text{Sb}_{1-x}$ films is shown in Figs. (3.34 and 3.35). If one compares between the graphs of samples deposited at 348- 473 K he can notice that α in general decreases with increasing T_s for all percentages.

The variation of absorption coefficient as a function of films thickness is systematic, and this may be attributed to the enhancement in crystal structure of the films. In general α has increased with the increase of film thickness as shown in Fig. (3.35). α has the same behavior of the absorbance, since they were calculated according to equation (1.24). The absorbance has increased with the increase of film thickness because in the case of thicker film, a dense atoms are present in the film so more states will be available for the photons to be absorbed as we mentioned before.



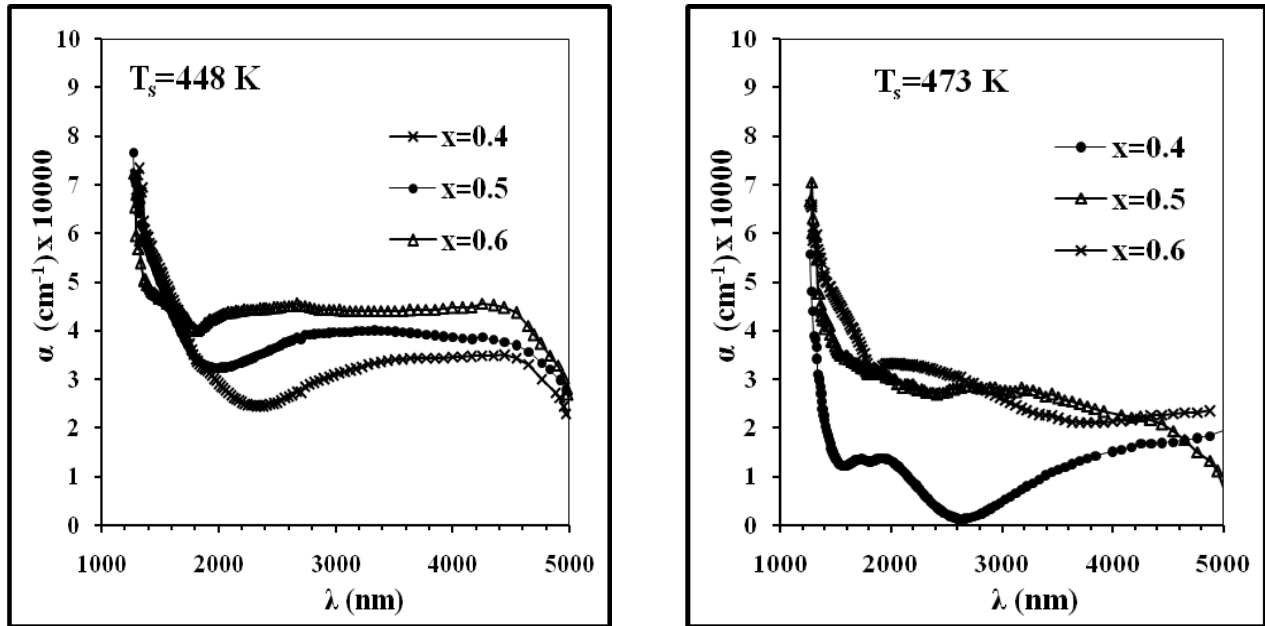


Figure (3.34): Variation of absorption coefficient as a function wavelength for $\text{Ga}_x \text{Sb}_{1-x}$ films with $t=400$ nm deposited at different x and T_s

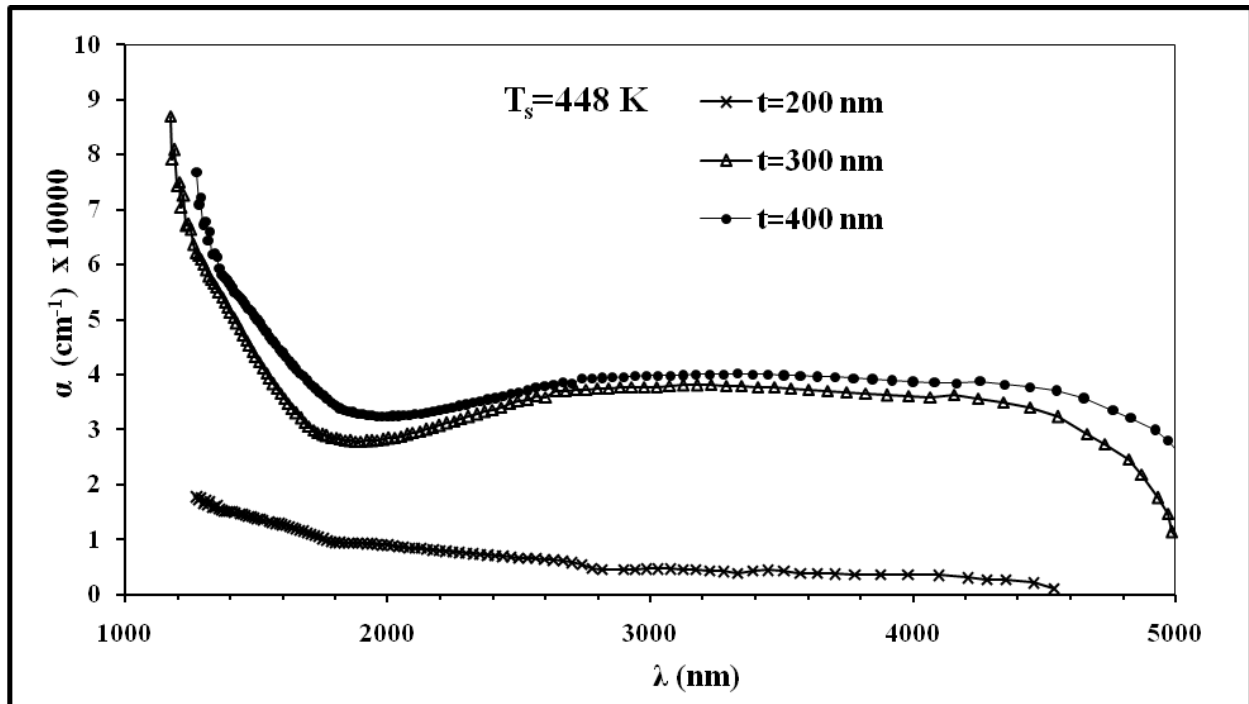


Figure (3.35): Variation of absorption coefficient as a function of wavelength for $\text{Ga}_{0.5} \text{Sb}_{0.5}$ films at different thicknesses.

3.6.3 The Optical Energy Gap

To determine the type of optical transmission we have examined $(\alpha h\nu)^{1/r}$ with $r=1/2, 1/3, 3/2$ and 2 versus $h\nu$ and found that the relation yielded a linear dependence for $r = 1/2$ which describes allowed direct transition. From Fig.(3.36) the energy gap is determined by plotting the Tauc equation (1.20) of the function $(\alpha h\nu)^2$ vs. $h\nu$ curve. Extrapolation of the line to the $h\nu$ axis gives the bandgap. The direct energy gap value was extrapolated and listed in Table (3.4), which is in agreement with values of other researchers [54,66]. The value of the optical energy gap increases with increasing of T_s for most samples due to the growth of the crystallites and also increase with increase of Ga percentage (ie. It decrease with increase of Sb percentage) as shown in Table (3.4) and Fig. (3.36). Gheorghiu et al.[54] referred to the optical energy gap decreases with access of Sb percentage. The optical energy gap decreased from 0.80 to 0.67 eV. with increasing thickness from (200-400) as shown in Fig. (3.37) and given in Table (3.5). This may be due to the increase of the density of localized states in the E_g , which cause a shift to lower values.

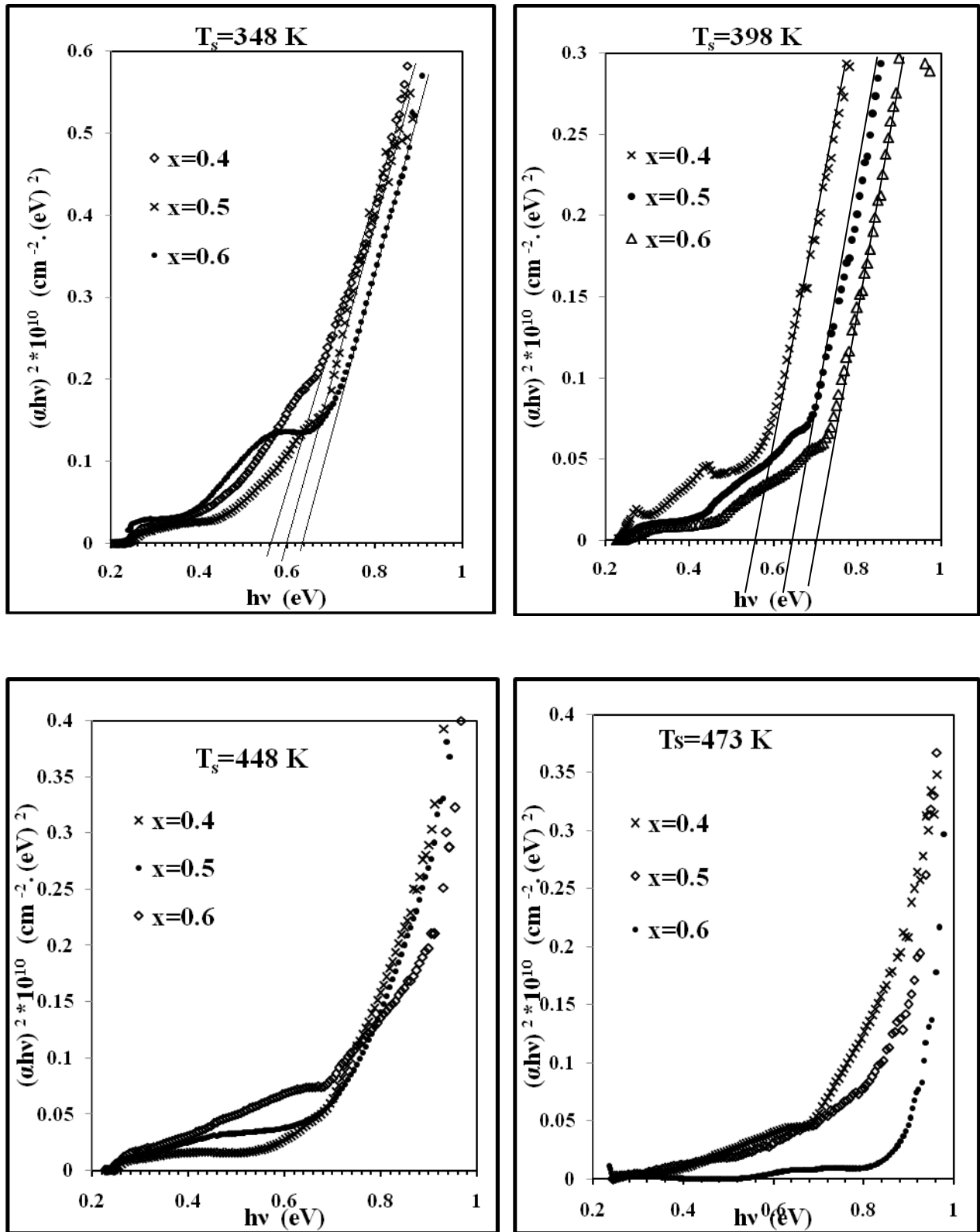


Figure (3.36) $(\alpha hv)^2$ as a function of $h\nu$ for $\text{Ga}_x\text{Sb}_{1-x}$ films with $t=400 \text{ nm}$ at different x and T_s .

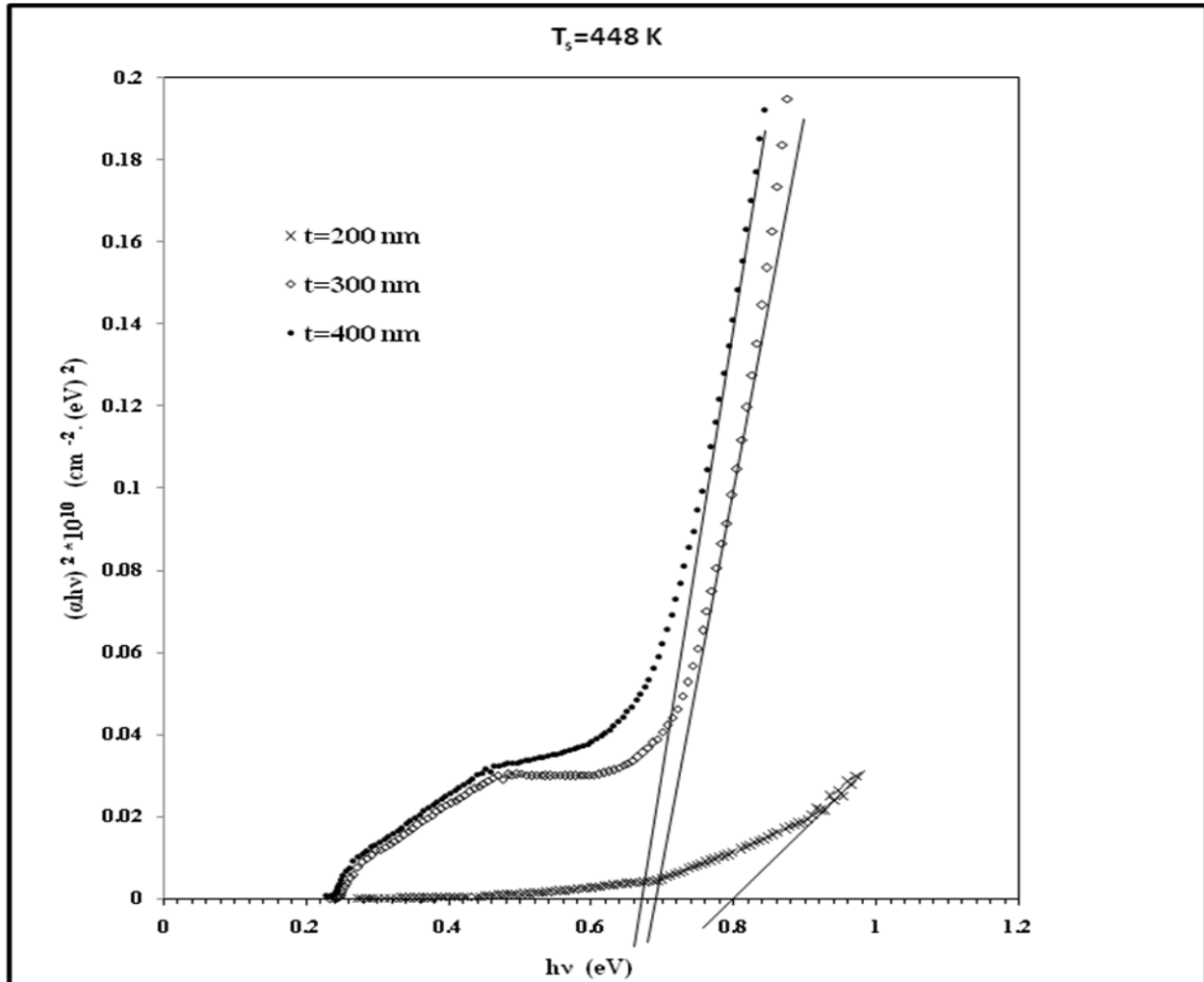


Figure (3.37): $(\alpha h\nu)^2$ as a function of $h\nu$ for $\text{Ga}_{0.5}\text{Sb}_{0.5}$ films at different thicknesses.

3.6.4 Extinction Coefficient

The extinction coefficient (k) calculated according to the equation (1.23), it decreases with increasing of substrates temperatures for all prepared $\text{Ga}_x\text{Sb}_{1-x}$ films, and it increases by increasing of thickness in the range as shown in Figs. (3.38),(3.39) and Table (3.4). The decrease of k with increase of T_s is attributed to the enhancement in crystal structure as it clear in x-ray patrons. The variation of k versus films thickness is systematic as shown in Fig. (3.39).

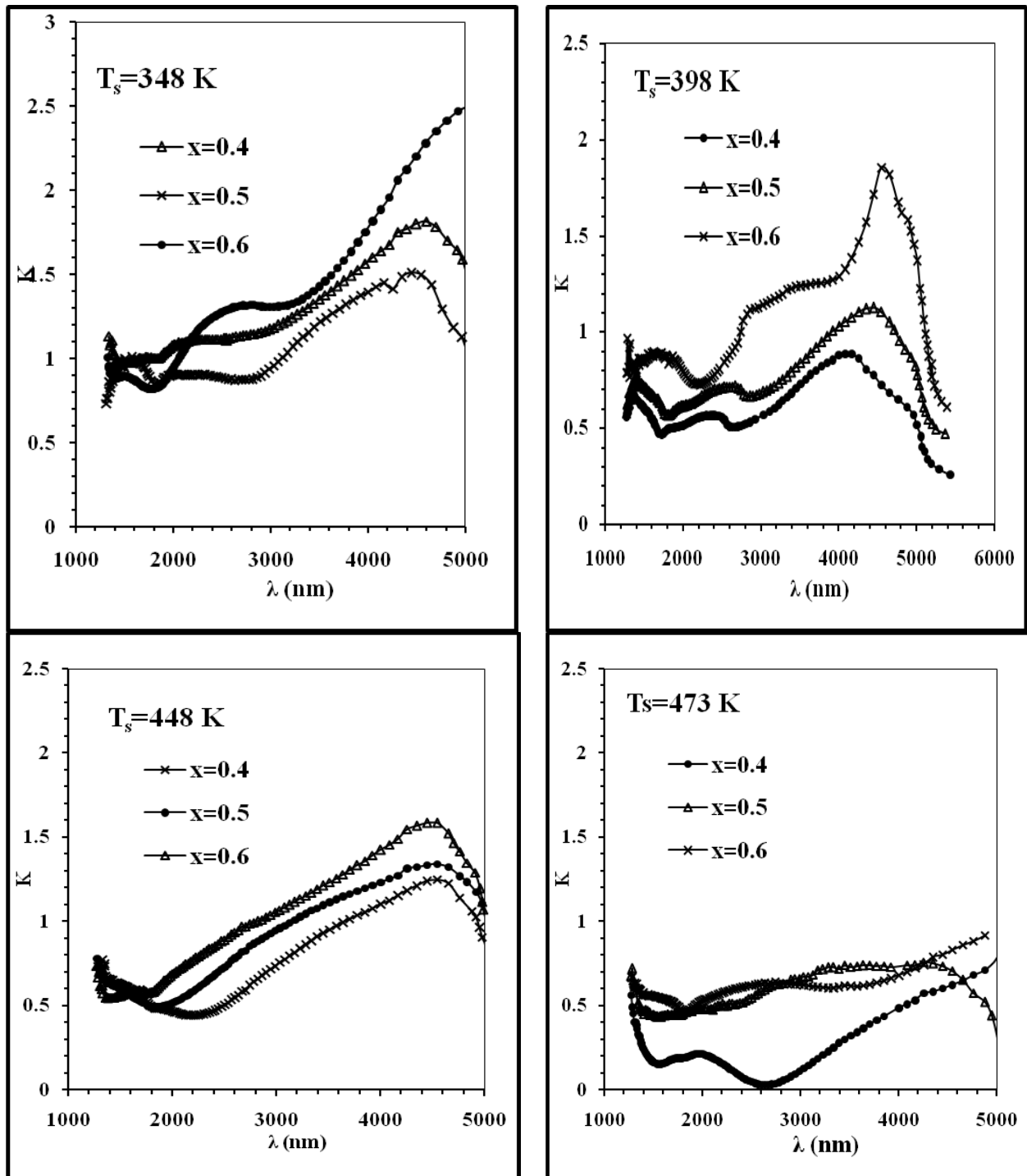


Figure (3.38): Extinction coefficient as a function of wavelength for $\text{Ga}_x\text{Sb}_{1-x}$ films with $t=400$ nm at different x and T_s .

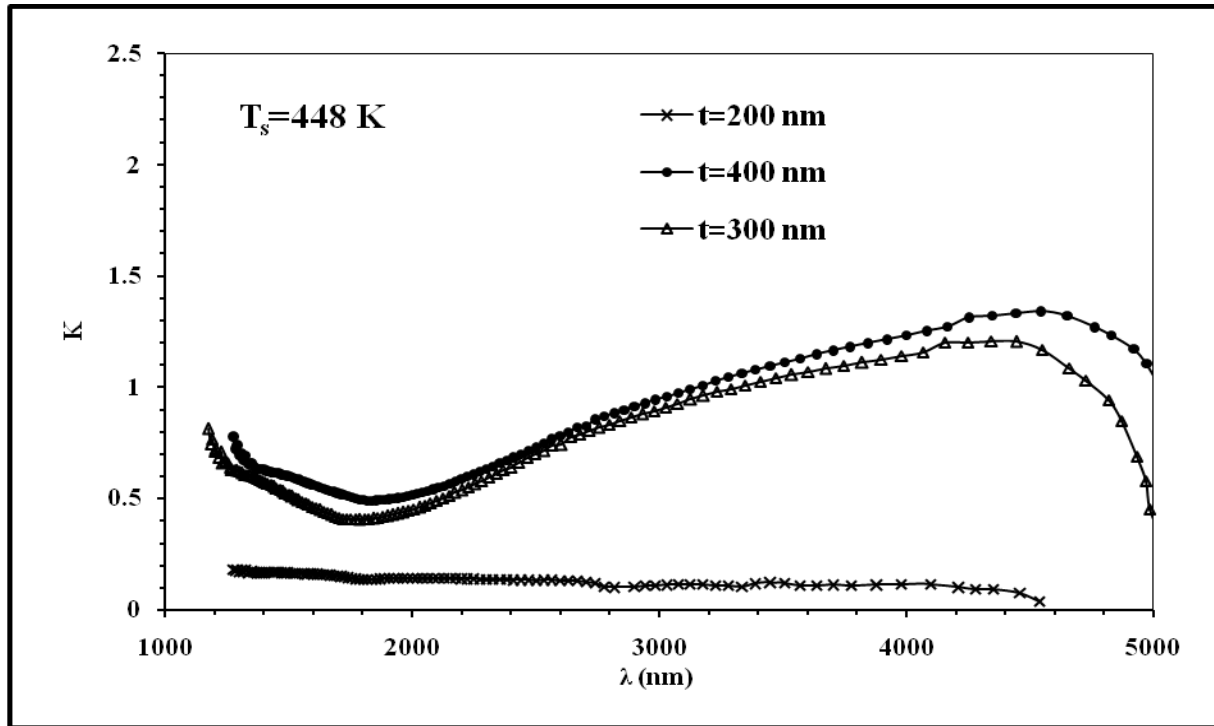


Figure (3.39): Extinction coefficient as a function of wavelength for $\text{Ga}_{0.5}\text{Sb}_{0.5}$ films at different thicknesses.

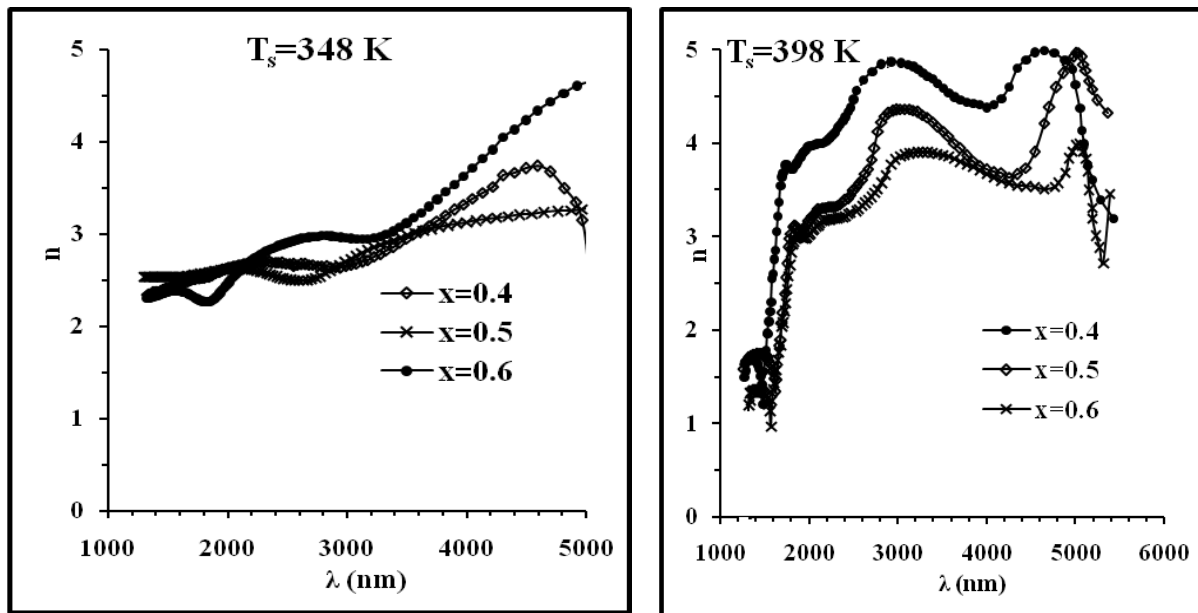
3.6.5 Refractive Index

The optical behavior of materials is generally utilized to determine its optical constants such as refractive index (n), it calculated according to equation 1.21. The variation of the refractive index as a function of the wavelength for $\text{Ga}_x\text{Sb}_{1-x}$ thin films for different x value and substrate temperatures is shown in Fig. (3.40) and Table (3.4), which indicate that the refractive index for films deposited at 348 K increasing with the increasing of Ga percentage (x) and with increase of energy gap is non-systematic since they are amorphous but for films deposited at 398,448,473 K the refractive index decreases with the increasing of Ga percentage (x) and with increase of energy gap due to the increase of the crystallite size.

In general for films deposited at 398,448,473 K the value of n decreased with decreasing λ_c . This behavior may be due to increase in energy gape which

causes to expand the lattice and grow the grain size and decreases the defects. That means decreasing the absorption and increasing the reflection which then depend on it. The value of n at $\lambda_{\text{cut of}}$ decrease with increasing x may be due to decrease in the packing density and increase in the degree of amorphousity [71].

Our results are in close agreement with other researchers [55,56]. The variation of n with thickness is not systematic as shown in Fig. (3.41) and Table (3.4). This may be due to different effective thickness of the films, and to the variation in crystal structure of the films.



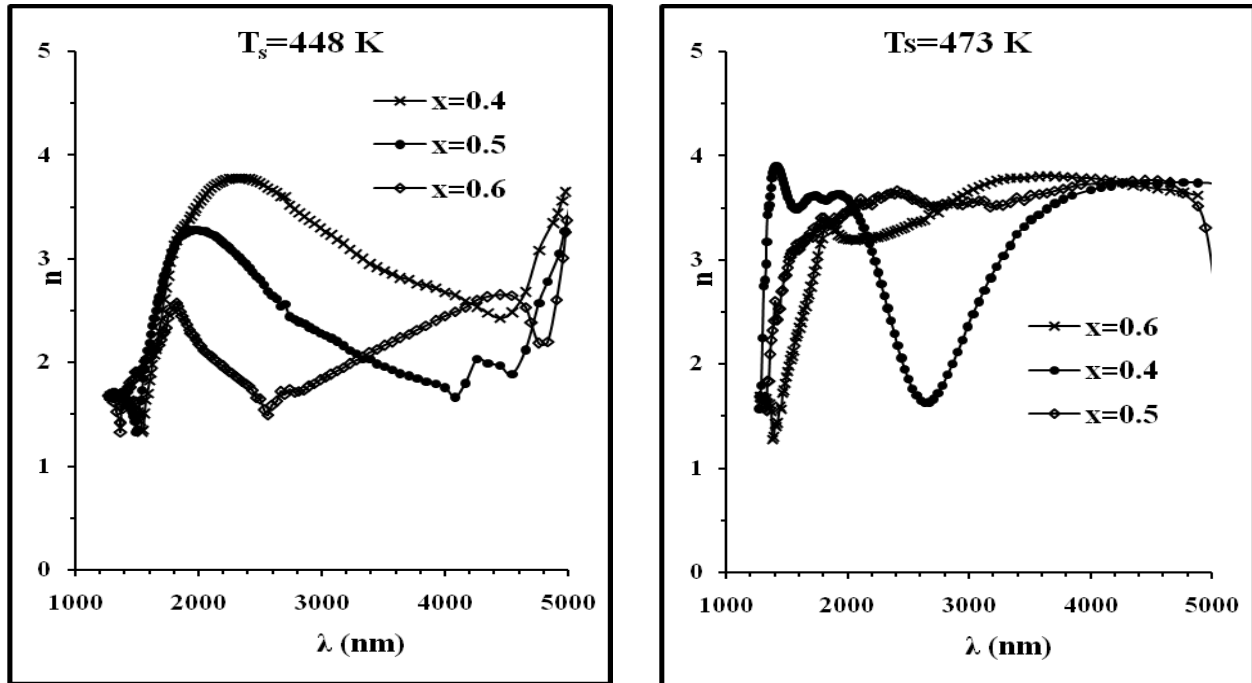


Figure (3.40): Refractive index as a function of wavelength for for $\text{Ga}_x \text{Sb}_{1-x}$ films at different x and T_s with $t = 400$ nm.

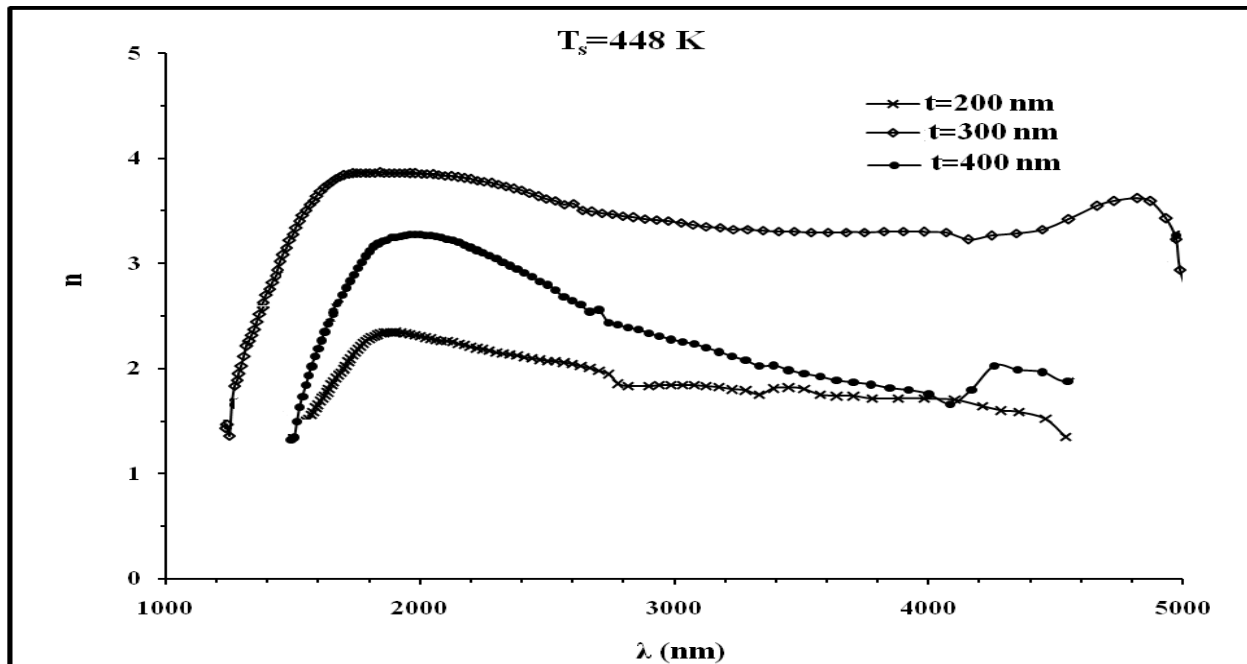


Figure (3.41): Refractive index as a function of wavelength for $\text{Ga}_{0.5} \text{Sb}_{0.5}$ films at different thicknesses.

3.6.6 The Dielectric Constant

The dielectric constant (ϵ) consists of real part (ϵ_r) and imaginary part (ϵ_i) depend on the frequency of the electromagnetic wave, they were calculated from equations 1.25 and 1.26 respectively. The variation of ϵ_r and ϵ_i versus wavelength in the range (1000-5000) nm at different substrate temperatures, x values and thicknesses as shown in Figs.(3.42), (3.44) and Tables (3.4),(3.5). The variation of ϵ_r and ϵ_i with the increase of the wavelength of the incident radiation is due to the change of reflectance and absorbance [72]. The behavior of ϵ_r is similar to that of the refractive index because of the smaller value of k^2 compared with n^2 , ϵ_i mainly depends on the k value, which are related to the variation of absorption coefficient. ϵ_i represents the absorption of radiation by free carriers [73]. It is observed that ϵ_r variation is non-systematic with increasing of substrate temperatures and it decrease with decrease of transmittance and with increase of x except the films deposited at 348 K . This is attributed to the same reason mentioned previously for the refractive index, while ϵ_i decreases with increasing of substrate temperatures. This is due to the similar interpretation discussed previously for the extinction coefficient.

The variation of ϵ_r and ϵ_i versus film thickness are shown in Figs. (3.43) and (3.45), respectively.

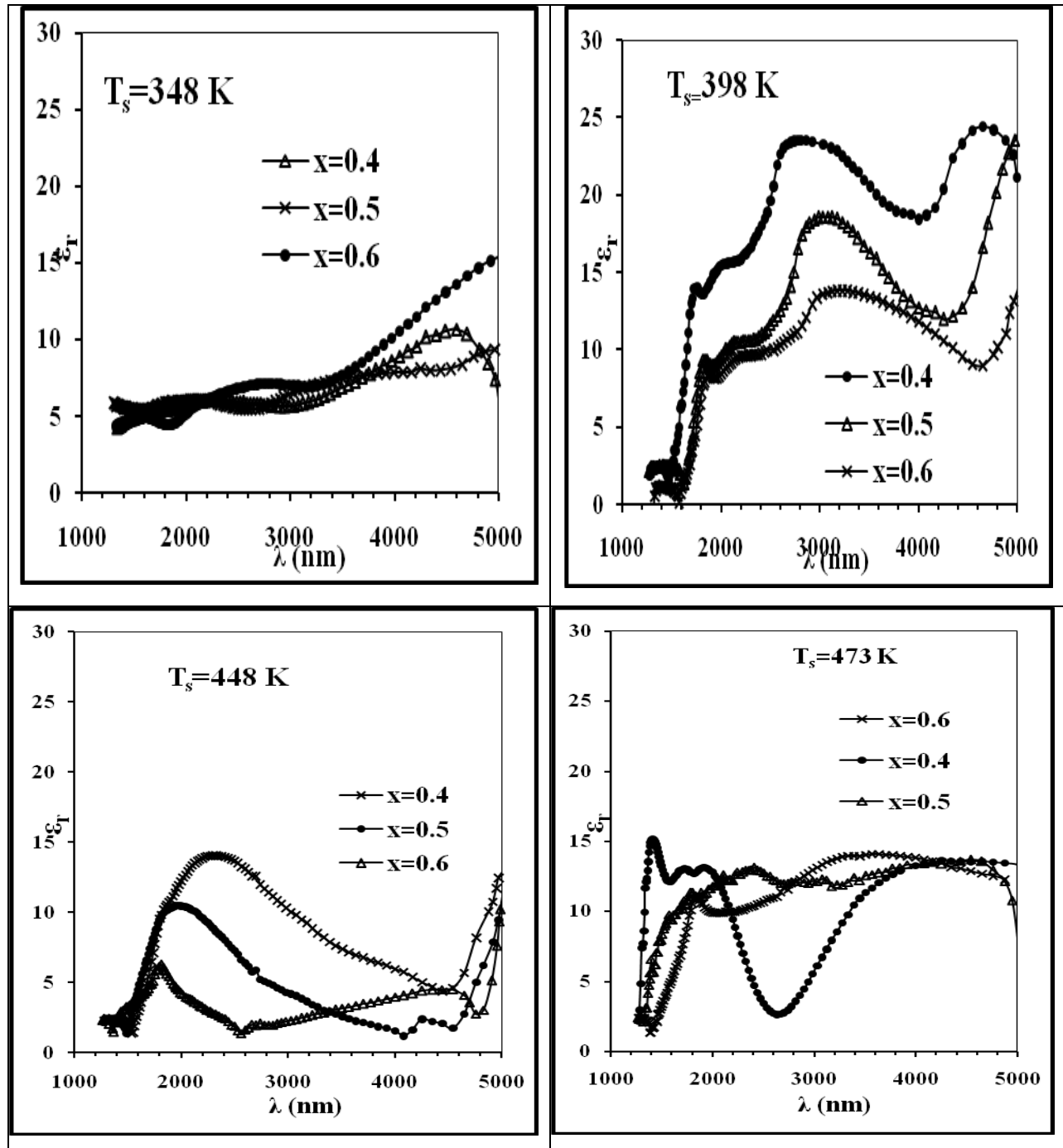


Figure (3.42): Real part of dielectric constant as a function of wavelength for $\text{Ga}_x\text{Sb}_{1-x}$ films at different x and T_s with $t=400$ nm.

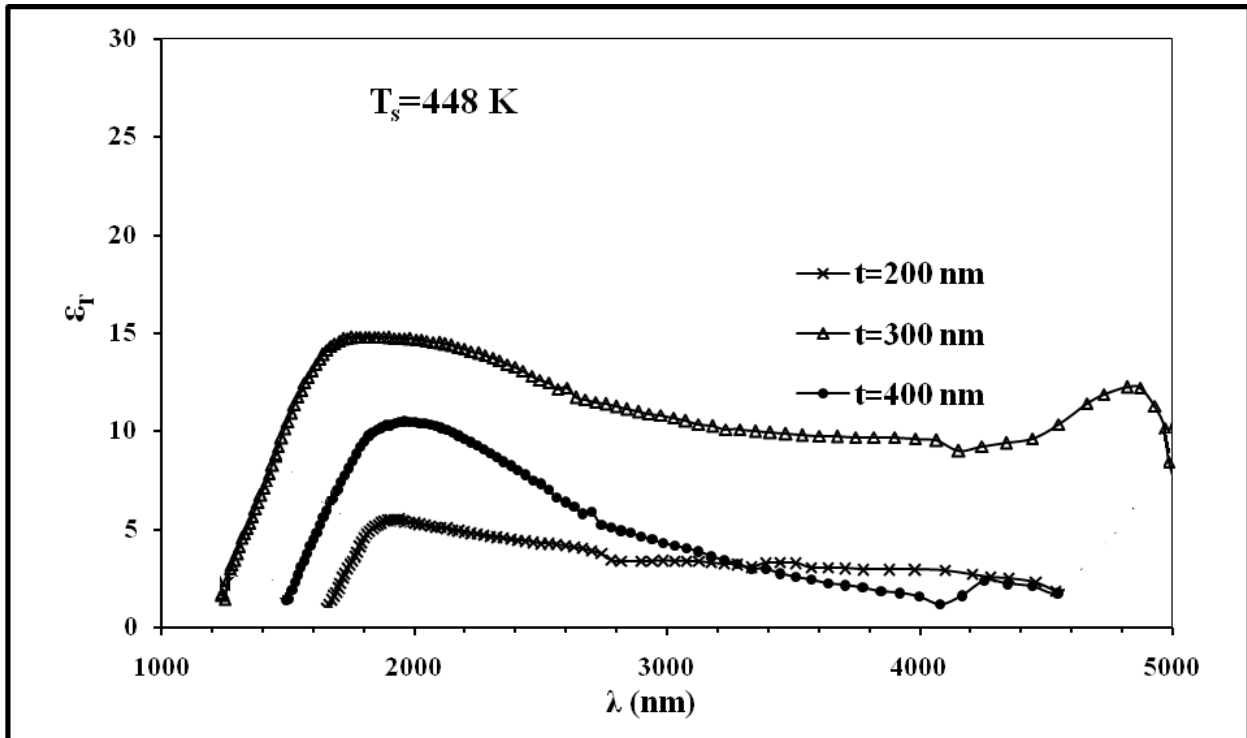


Figure (3.43): Real part of dielectric constant as a function of wavelength for $\text{Ga}_{0.5}\text{Sb}_{0.5}$ films at different conditions.

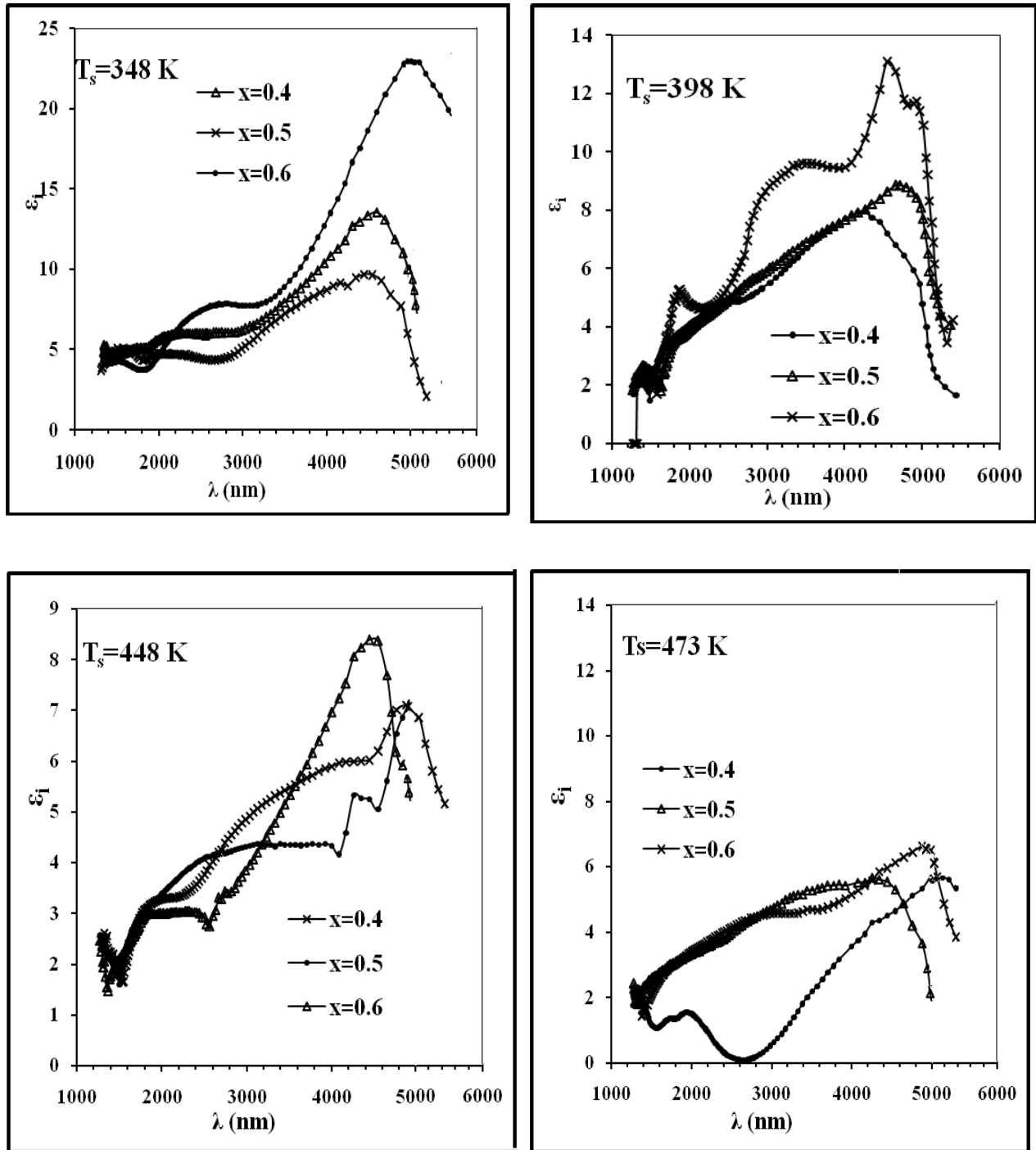


Figure (3.44): Imaginary part of dielectric constant as a function of wave length for $\text{Ga}_x\text{Sb}_{1-x}$ films at different x and T_s with $t=400$ nm.

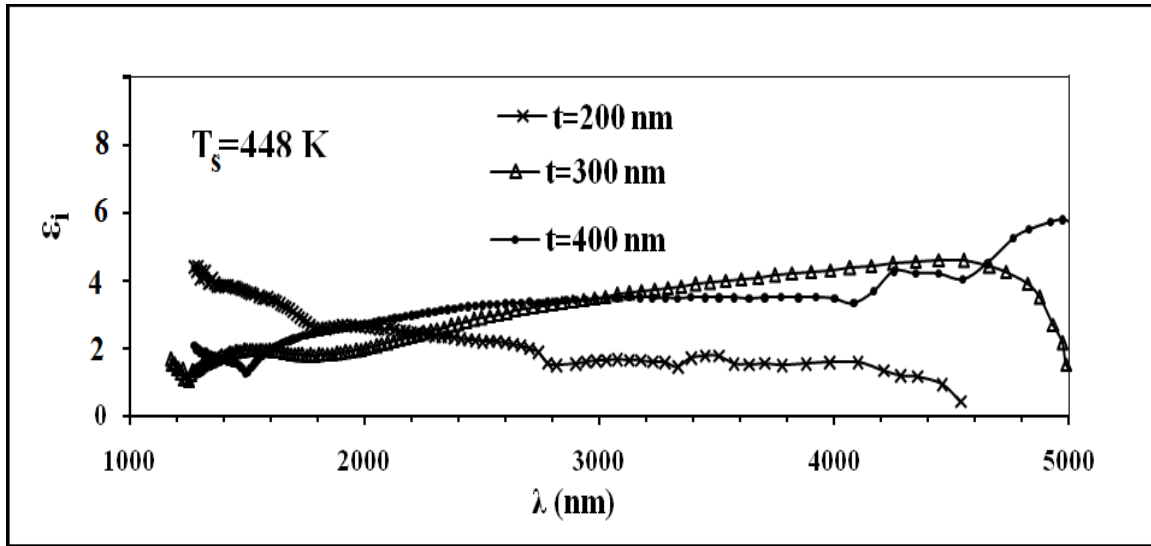


Figure (3.45): Imaginary part of dielectric constant as a function of wavelength for $\text{Ga}_{0.5}\text{Sb}_{0.5}$ films at different thicknesses.

Table (3.4): Optical properties parameters for $\text{Ga}_x\text{Sb}_{1-x}$ films at different x and T_s at λ_c .

$T_s(\text{K})$	x	$E_g(\text{eV})$	λ_c (nm)	T%	$\alpha (\text{cm}^{-1})$ $\times 10^4$	K	n	ϵ_r	ϵ_i
348	0.4	0.56	2214	5.5	6.05	0.83	2.32	4.70	3.84
	0.5	0.60	2066	3.7	4.83	1.30	2.85	6.46	7.41
	0.6	0.64	1937	2.64	5.49	0.90	2.62	6.09	4.74
398	0.4	0.52	2380	9.16	2.98	0.56	4.23	17.65	4.80
	0.5	0.65	1907	4.28	3.98	0.59	3.06	9.01	3.65
	0.6	0.71	1746	0.64	6.30	0.87	2.28	4.46	3.98
448	0.4	0.68	1823	13.7	3.31	0.48	3.23	10.20	3.10
	0.5	0.73	1698	9.67	3.89	0.52	2.70	7.02	2.80
	0.6	0.80	1550	6.28	4.61	0.57	1.95	3.48	2.22
473	0.4	0.82	1512	13.6	3.32	0.40	3.25	10.42	2.60
	0.5	0.84	1476	10.7	3.72	0.41	2.91	8.29	2.37
	0.6	0.90	1377	7.13	4.40	0.48	2.23	4.72	2.15

Table (3.5): Optical properties parameters for Ga_{0.5}Sb_{0.5} films at different thicknesses at
T_s= 448K.

t (nm)	E _g (eV)	λ _c (nm)	T%	α (cm ⁻¹) *10 ⁴	K	n	ε _r	ε _i
200	0.80	1550	67.2	1.3	0.27	2.29	5.27	1.2
300	0.69	1797	27.8	2.8	0.30	3.80	14.44	2.28
400	0.73	1698	9.67.5	3.89	0.52	2.70	7.30	2.80

3.7 Electrical characteristics of Heterojunction

The electrical characteristics involve I-V and C-V measurements for Ga_xSb_{1-x}/GaAs heterojunction.

3.7.1 Current-Voltage Characteristics Measurements at Dark and Illumination.

The current-voltage characteristic at dark is an important parameter of diode measurements; indicates the behavior of the current with the applied forward and reverse bias voltage. Fig. (3.46) show I-V characteristics of Ga_xSb_{1-x}/GaAs heterojunction having different thicknesses, substrate temperature 348 and 473 K, gallium percentage 0.6 respectively, forward and reverse bias voltages in the dark as well as under the illumination.

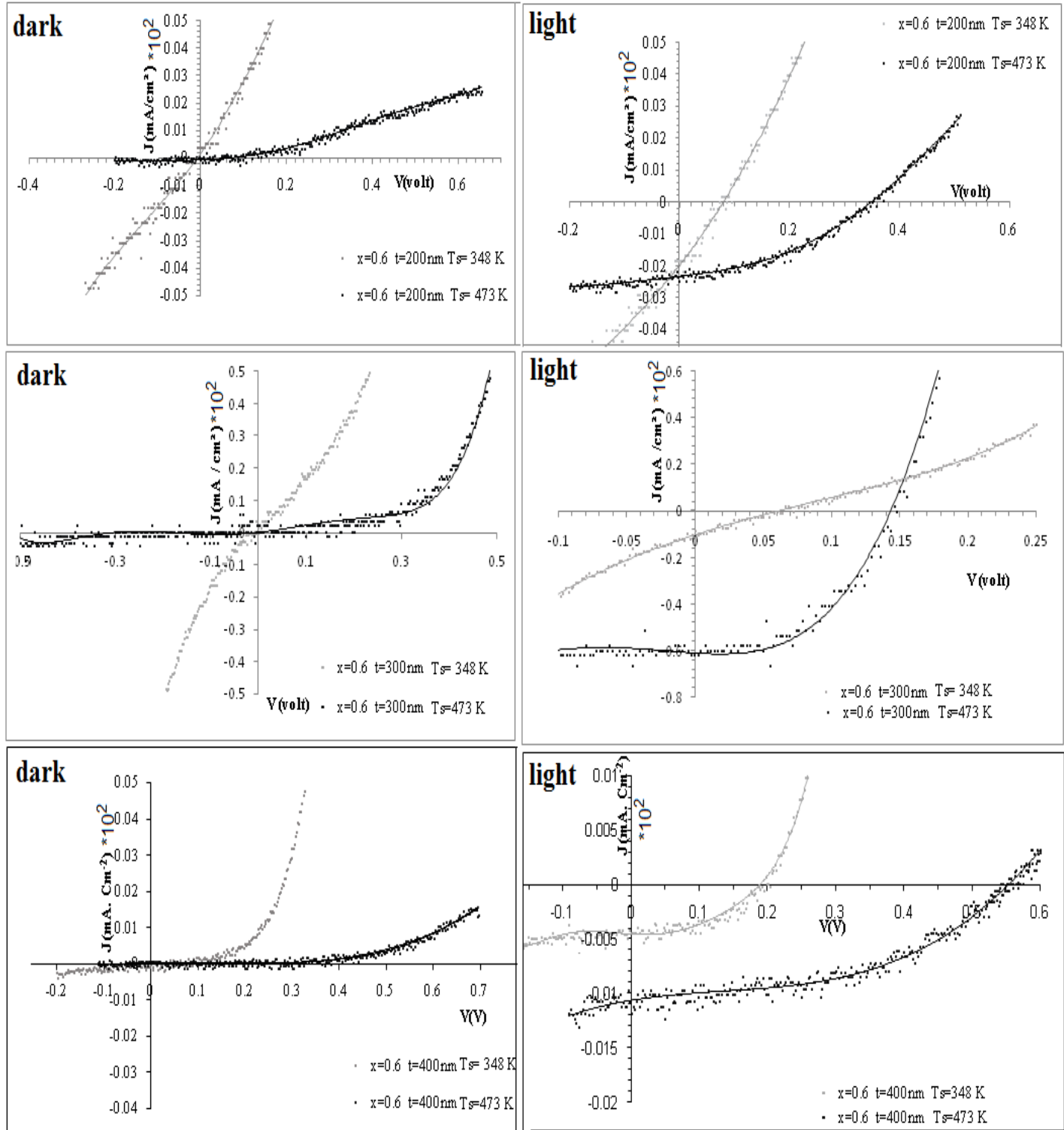


Fig.(3.46) J-V characteristics of $Ga_{0.6}Sb_{0.4}/GaAs$ at dark and under illumination at substrate temperatures 348 and 473 K, thicknesses 200,300 and 400 nm .

Table (3.6): Figure of merit for $\text{Ga}_{0.6}\text{Sb}_{0.4}$ films at different T_s and thicknesses.

t.(nm)	T_s (K)	V_{oc} (V)	J_{sc} (mA/cm ²)	V_{max} (V)	J_{max} (mA/cm ²)	F.F	$\eta\%$
200	348	0.08	2	0.05	0.8	0.250	0.04
	473	0.35	2.3	0.2	1.8	0.447	0.36
300	348	0.06	9	0.03	7.5	0.417	0.23
	473	0.14	61	0.09	46	0.485	4.14
400	348	0.19	0.5	0.12	0.3	0.379	0.04
	473	0.55	1.2	0.35	0.8	0.424	0.28

Fig. (3.46 Light) and Table (3.6) show the photocurrent of $\text{Ga}_{0.6}\text{Sb}_{0.4}/\text{GaAs}$ heterojunction under illumination with different thicknesses and substrates temperatures, with incident light power density 100 mW/cm^2 .

The area in fourth region increases with the increasing of substrates temperature and it decrease with increasing of thickness this is meaning the efficiency is increased with increasing of T_s due to enhancement of structure , and it increased with increasing of thickness from 200 to 300 nm for film deposited at 348 and 473 K but it decreased with increasing of thickness from 300 to 400 nm for which is due to increasing of structural defects induced by lattice mismatch , which provides electron-hole recombination centers. The created electron hole pairs may recombine before separate by the junction. For this reason $\text{Ga}_x\text{Sb}_{1-x}/\text{GaAs}$ heterojunction efficiency that we synthesized is very low.

3.7.2 Capacitance-Voltage Measurement

The capacitance versus reverse bias voltage at the range (0-2) volt with 1kHz frequency for $\text{Ga}_x\text{Sb}_{1-x}/\text{GaAs}$ heterojunction, with different T_S , gallium content and thicknesses respectively. It is obvious that the capacitance decreases with increasing of the reverse bias voltage, and this result is in agreement with equation (2.8). Such behavior is attributed to the increasing in the depletion region width, which leads to increase the value of built-in potential (V_{bi}). The capacitance decreases with increasing of GaSb thickness due to the increasing of the depletion region. Carriers concentration (N_A) of these junctions have been deduced as listed in Tables (3.12 and 3.13) from the slope of the straight line in Figs. (3.47a, b and c) by using equation (2.8).

The inverse capacitance squared was plotted against applied reverse bias voltage as shown in Figs. (47.a, b, c, d). The plots reveal a straight-line relationship, which means that the junction is an abrupt-type. The intersection of the straight line with the voltage axis at ($1/C^2=0$), represent (V_{bi}) [74, 75], as given in Tables (3.7-3.10). We notice from these Tables increased in V_{bi} value with increasing substrates temperature and Ga percentage of the film due to the increasing of crystallite of films, V_{bi} value decrease with increasing thickness of films due increasing of defects concentration as a result of mismatch between the two materials, these defects act as recombination centers extinguish charge carriers, which leads to decreasing the depletion region width [76]. Tables (3.12-3.13) shows the depletion region value increased with increasing of substrates temperature and Ga percentage of the film but the junction carriers decreased with increasing of substrates temperature and Ga percentage of the film due to the increasing of crystallite of films.

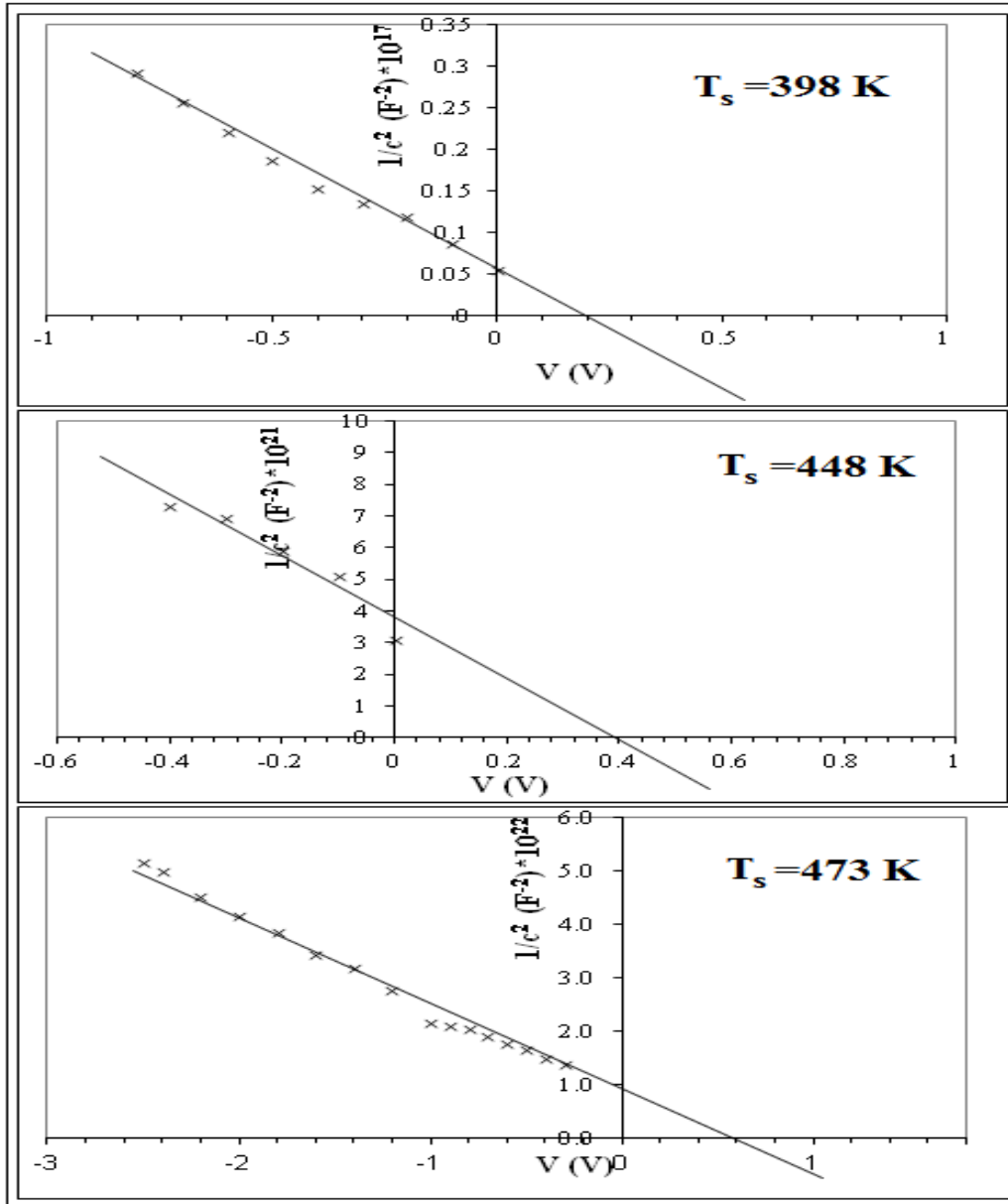


Fig.(3.47.A) C-V characteristic of Ga_{0.6}Sb_{0.4} thickness =200 nm, at frequency 1kHz.

Table (3.7) V_{bi} values at different T_s of Ga_{0.6}Sb_{0.4} thickness =200 nm, at frequency 1kHz.

$T_s \text{ (K)}$	398	448	473
$V_{bi} \text{ (V)}$	0.2	0.4	0.6

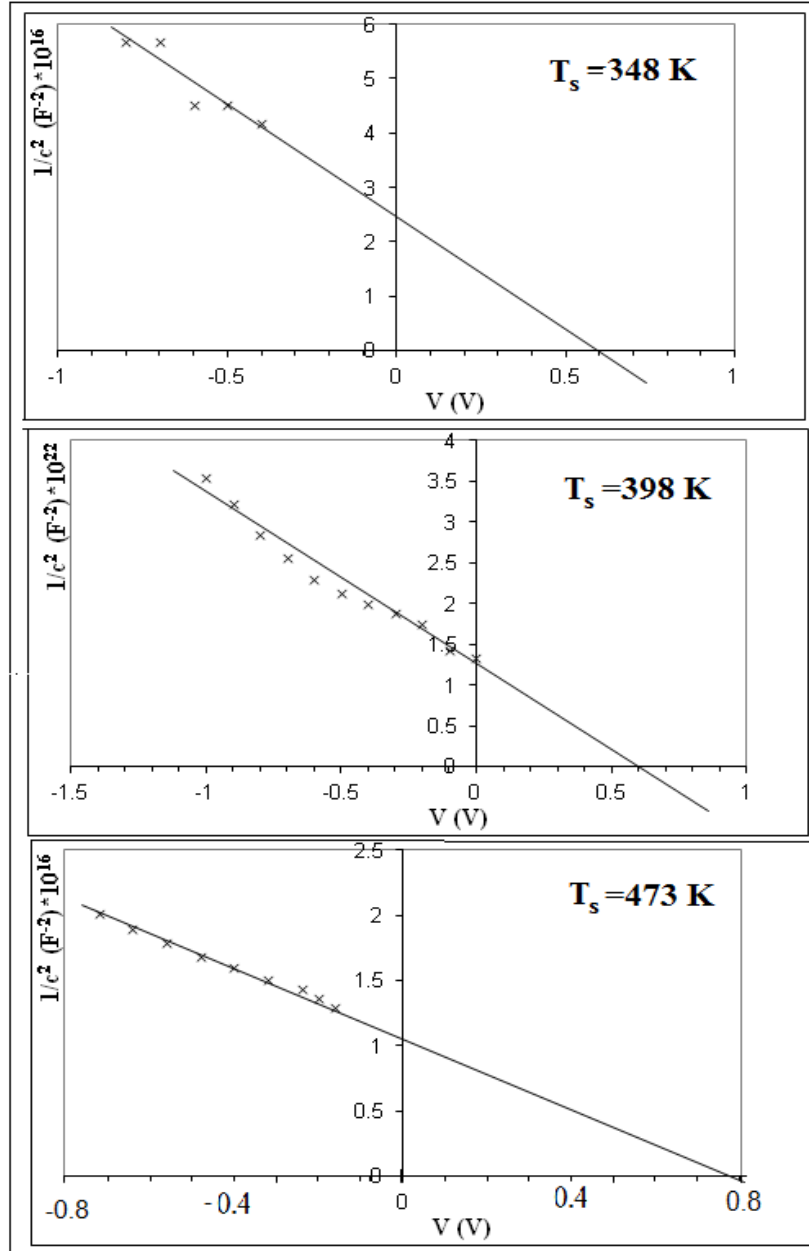


Fig.(3.47.B) C-V characteristic of $\text{Ga}_{0.6}\text{Sb}_{0.4}$ thickness =400 nm.

Table (3.8) V_{bi} values at different T_s of $\text{Ga}_{0.6}\text{Sb}_{0.4}$ thickness =400 nm.

T_s (K)	348	448	473
V_{bi} (V)	0.58	0.63	0.8

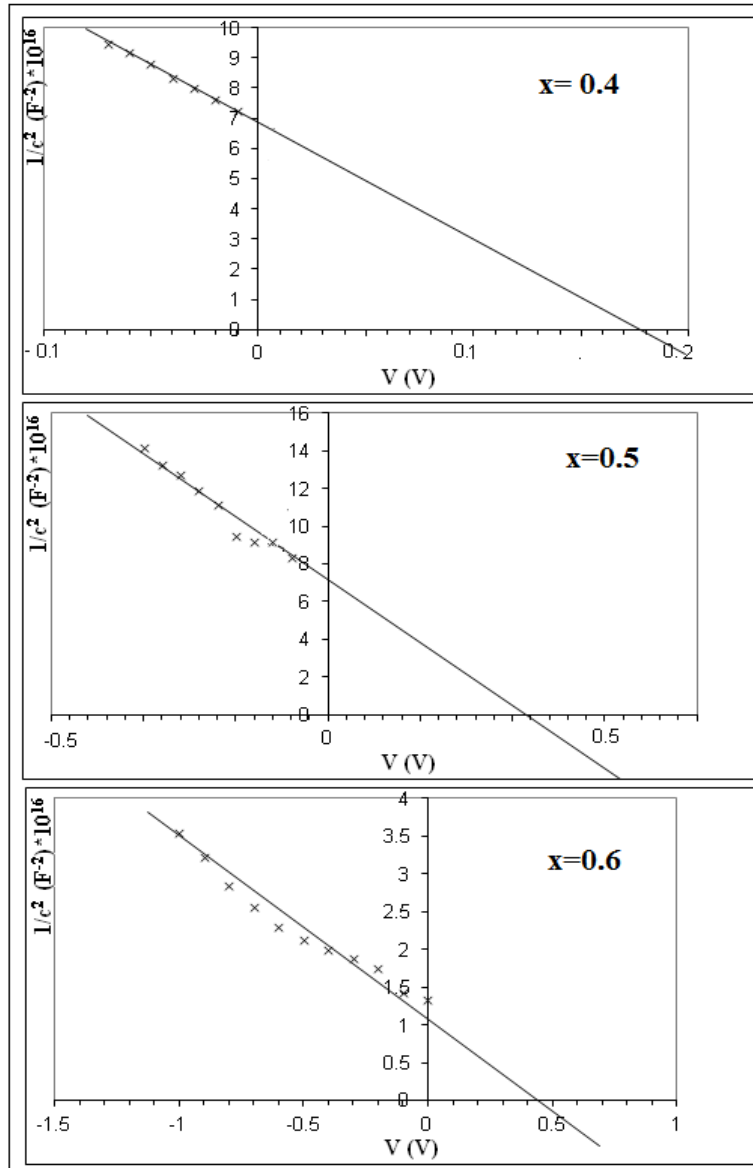


Fig.(3.47.C) C-V characteristic of $\text{Ga}_x\text{Sb}_{1-x}$ thickness =400,substrate temperature 398 K.

Table (3.9) V_{bi} values at different Ga percentage of $\text{Ga}_x\text{Sb}_{1-x}$ films thickness =400 nm at substrate temperature 398 K.

x	0.4	0.5	0.6
V_{bi} (V)	0.18	0.37	0.45

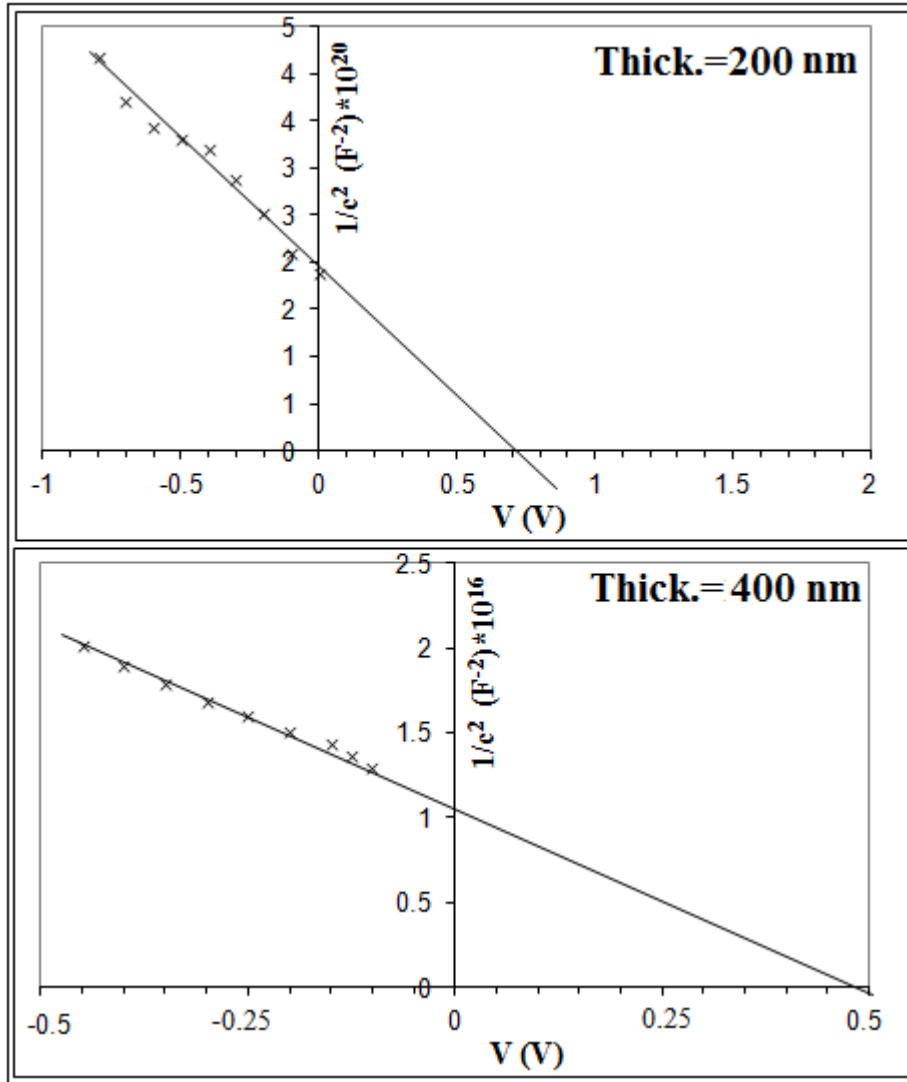


Fig.(3.47.D) C-V characteristic of $Ga_{0.6}Sb_{0.4}$, substrate temperature 473 K .

Table (3.10) V_{bi} values at different film thickness of $Ga_{0.6}Sb_{0.4}$, substrate temperature 473 K .

Thick. (nm)	200	400
V_{bi} (V)	0.7	0.5

The effects of thickness on ideality factor is shown in Table (3.11) We observe that the it decrease with increasing of GaSb thickness from 200 to 300 nm but it increase with increase the thickness from 300 to 400 nm due to that dislocations increasing with thickness increasing so that the dislocations can act as electron trapping centers and as hole-electron recombination centers and states at the interface can produce internal depletion layers and consequent bending of the valence and conduction levels and can increase the recombination probability for minority carriers passing across the junction which leads to an increase in the depletion region width.

Table (3.11) Values of ideality factor (β) with different thicknesses of $\text{Ga}_{0.6}\text{Sb}_{0.4}$ at $T_s=348$ K.

t (nm)	200	300	400
β	4.32	1.68	3.8

Table (3.12) Values of depletion layer width and carriers concentration for $\text{Ga}_{0.4}\text{Sb}_{0.6}/\text{GaAs}$ Heterojunction with thickness 200 nm.

T_s K	Junction Type	C_o/A (F.cm ⁻²)	W μm	V_{bi} (V)	N_A (cm ⁻³)
398	n-n	13×10^{-9}	0.05	0.2	7×10^{18}
448	n-n	1.62×10^{-11}	2.4	0.4	5.1×10^{11}
473	p-n	1.01×10^{-11}	12	0.6	3.25×10^{11}

Table (3.13) Values of depletion layer width and carriers concentration for $\text{Ga}_x\text{Sb}_{1-x}/\text{GaAs}$ Heterojunction with thickness 400 nm .

X	Junction Type	C_o/A (F.cm ⁻²)	W μm	V _{bi} V	N _A cm ⁻³
0.4	n-n	3.77×10^{-10}	0.08	0.18	2.5×10^{16}
0.5	n-n	3.7×10^{-10}	1.95	0.37	8.11×10^{13}
0.6	p-n	9.53×10^{-12}	15.6	0.45	1.5×10^{12}

C h a p t e r F o u r

Conclusions and Suggestions

4.1 Conclusions

The following conclusions can be deduced from this work:

4.2 Composition and Structure

- The EDXS analysis results are almost coincidence with theoretical percentages value of Ga and Sb in $\text{Ga}_x\text{Sb}_{1-x}$ alloys and films.
- XRD analysis confirms that the structure of $\text{Ga}_x\text{Sb}_{1-x}$ alloys are polycrystalline.
- XRD analysis confirms that most of $\text{Ga}_x\text{Sb}_{1-x}$ films are amorphous for $T_s = 348$ K and poly crystalline with a cubic zincblend structure for $T_s = 473$ K.
- The preferred orientation is (111) for $T_s = 473$ K, for different thicknesses and gallium percentage.
- The morphology of prepared $\text{Ga}_x\text{Sb}_{1-x}$ films are homogenous.
- The grain size increases with increasing substrate temperatures, thicknesses and gallium percentage.
- The grain boundary decreases with increasing substrate temperatures for films of $\text{Ga}_{0.4}\text{Sb}_{0.6}$ and it increases for $\text{Ga}_{0.6}\text{Sb}_{0.4}$.

4.3 Electrical Properties

- The D.C conductivity for $\text{Ga}_x\text{Sb}_{1-x}$ films increases as gallium percentage and substrates temperatures increase.
- There are two transport mechanisms of the charge carriers in the range of (300-473) K.
- The activation energies increase as gallium percentage increases and substrates temperatures increase.
- Hall measurements show that $\text{Ga}_{0.4}\text{Sb}_{0.6}$ films are n-type and $\text{Ga}_{0.6}\text{Sb}_{0.4}$ films are p-type.
- The charge carriers concentration increases with increasing the substrates temperatures and thickness.
- Hall mobility increases with increasing the gallium percentage and thickness.

4.4 Optical Properties

- The optical transitions in $\text{Ga}_x\text{Sb}_{1-x}$ film is direct transition.
- The value of optical energy gap increases with increasing of substrates temperatures, gallium percentage whereas it decreases with increasing thickness.

4.5 Heterojunction Properties

4.5.1 I-V and C-V Measurements

- The efficiency of $\text{Ga}_x\text{Sb}_{1-x}$ /GaAs solar cell increases with increasing of substrate temperatures while it decreased with increasing of film thickness.
- The dark current decreases with increasing of substrate temperatures.
- The built in voltage increase with increasing of substrate temperature, gallium percentage whereas it decreases with increasing of film thickness.
- The junction is an abrupt type.

4.6 Suggestions for Future Work

- Fabricate a-GaSb / a-Si solar cell and study their characteristics and figure of merits.
- Fabricate Photovoltaic detector for IR of a-GaSb /a-Ge .
- Prepare hydrogenation of a-GaSb films to reduce the density of localized states and study the junction characteristics.



References

- 1- J. Chu , A. Sher “**Device Physics of Narrow Gap Semiconductors**” Springer, New York, P.5 (2010).
- 2- E. F. Schubert “**Physical Foundations of Solid State Devices**”, Troy, New York, Chapter 17(**2009 Edition**).
- 3- Farseem M. Mohammedy & M. Jamal Deen, J. Mater Sci. Mater Electron, **20**, pp. 1039–1058 (2009).
- 4- L. Broman, Prog. Photovolt. Res. Appl. **3**, pp. 65-74 (1995).
- 5-T.J. Coutts, Renew and Sustain En. **3**, pp. 77-184 (1999).
- 6-H.H. Kolm, Quaterly Progress Report, Solid State Research, Group 35, MIT-Lincoln Laboratory, Lexington, MA (USA), p. 13,(May **1956**).
- 7- R.E. Nelson, 5th Conference on TPV Generation of Electricity, AIP Conference Proceedings 653, pp. 3-17(2003).
- 8- B.D. Wedlock, Proc. IEEE **51**, p. 694-698(1963).
- 9- D. C. White, B.D. Wedlock y J. Blair, Proc. **15th** Power Sources Conf., pp. 125-132 (1961).
- 10- R.N. Bracewelly R.M. Swanson, Report ER-633, Electric Power Research Institute, p.84 (1978).
- 11- F. Demichelis y E. Minetti-Mezzetti, Solar Cells **1**, pp. 395-403 (1979).
- 12- R.M. Swanson, Proc. Int. electron. Devices Meeting (Washington DC, USA), pp. 186-189 (1980).
- 13-P. Wurfel y W. Ruppel, IEEE Trans. on Electron Devices **27**, pp. 745-750 (1980).
- 14- A. Luque, P.A. Davies, A. Marti, C. Algora, J. Alonso, J.C. Maroto, J. Olivan, I. Tobías, J.C. Zamorano, J.C. Miñano, G.L. Araujo, G. Sala, C.

- Flores, L. Mayet, M. Gavand y A. Laugier, Proc. 11th European PVSC, pp. 150-154 (1992).
- 15- J.M. Gee y G.F. Virshup, Proc. of the 20th IEEE PVSC, (Las Vegas, Nevada), pp. 754-758 (1988).
- 16- L.M. Fraas, J.E. Avery, P.E. Gruenbaum, V.S. Sundaram, A.G. Thomson and J.M. Gee, J. Appl. Phys. 66, p. 3866 (1989).
- 17- C. J. Nuese, Journal of Electronic Materials, Vol. 6, No. 3 (1977).
- 18- T. Ikoma ,“**Recent Compound Semiconductor Handbook**” Science Forum, Tokyo(1982).
- 19- Kiyotaka Wasa,MakotoKitabatake,Hideaki Adachi. “**THIN FILM MATERIALS TECHNOLOGY, Sputtering of Compound Materials**” William Andrew publishing, springer.pp17-20,33-34 (2004).
- 20- N. N. Ledentsov “ **Growth Processes and Surface Phase Equilibria in Molecular Beam Epitaxy**” Springer, Berlin (1999).
- 21- Minghua Sun “**Optical and Crystal Structure Characterizations of Nanowires for Infrared Applications**” Ph.D. thesis, arizona state university (2011).
- 22- Abuduwayiti Aierken “**Passivation of GaAs Surfaces and Fabrication of Self-assembled In(Ga)As/GaAs Quantum Ring Structures**” Ph.D. thesis, Helsinki University of Technology (2008).
- 23- Hansen M . “**Constitution of binary alloys**” Second Edition , Mc Graw-Hill book company USA. p.755 (1958).
- 24- Neil W. Ashcroft, N. David Mermin, “**Solid State Physics**” New York Orlando Austin London, (1976).
- 25- Ming-Cheng Lo, Shyh-Jer Huang, Chien-Ping Lee, Sheng-Di Lin, and Shun-Tung Yen, Applied Physics Letters **90**, 243102 (2007).

- 26- J.J.J. Yang, P.D. Dapkus, R.D. Dupuis, R.D. Yingling, J. Appl. Phys. **51**, 3794(1980).
- 27- J.YW. Seto, J. Appl. Phys. **12**, 5247 (1975).
- 28- Yingda Dong, Dennis W. Scott, Yun Wei, Arthur C. Gossard, Mark J. Rodwell, Journal of Crystal Growth **256**,pp. 223–229 (2003).
- 29- L.L. Kazmerski ,Academic Press, P.87(1980).
- 30- J.Volger, Phys.Rev. **9**, 1023 (1950).
- 31-Shay J. L., Wagner S., and Phillips J. C. Applied Physics Letters, **28**, 31 (1976).
- 32- W. R. Runyan, "**Semiconductor Measurements and Instrumentation**", Texas Instruments Incorporated, 2nd ed., McGraw-Hill, Kogakusha, Tokyo, (1975).
- 33- N. F. Mott and E. A. Davis, "**Electronic Process in Non-Crystalline Materials**", 2nd ed., Clarendon Press, Oxford, (1979).
- 34- D. A. Neaman "**Semiconductor Physics and Devices**", Richard D. Irwin, Inc., Boston, (1992).
- 35- J. S. Blakemore "**Solid State Physics**", 2nd ed., W. B. Saunders Company, Philadelphia, (1974).
- 36- C. Kittel "**Introduction to Solid State Physics**", 8th ed., John Wiley and Sons, Inc., New York, (2005).
- 37- S. M. Sze "**Physics of Semiconductor Devices**", 2nd ed., John Wiley and Sons, Inc., New York, (1981).
- 38-J. Millaman "**Microelectronics**", Murray-Hill, Book Company Kogakusha, (1979).
- 39-F. Jenkins and H. White "**Fundamentals of Optics**", 3rd ed., McGraw-Hill Book Company, New York, (1957).
- 40- R. A. Smith, "**Semiconductors**", 2nd ed., Cambridge University Press, London, (1979).
- 41- D. P. Padiyan, A. Marikani, and K. R. Murali, Material Chemistry and Physics, **78**, pp.51-58, (2002).

- 42- I. Mills, T. Cvitas, K. Homann, N. Kallay, and K. Kuchitsu, **"Quantities, Units and Symbols in Physical Chemistry"**, 2nd ed., Blackwell Scientific Publications, Oxford, (1993).
- 43- J. Millaman, **"Microelectronics"**, Murray-Hill, Book Company Kogakusha, (1979).
- 44- J. E. Bertie, **"Handbook of Vibrational Spectroscopy"**, John Wiley and Sons, Ltd. (2001).
- 45- R. J. Elliot and A. I. Gibson **"An Introduction to Solid State Physics and Application"**, 1st ed., Macillian Inc. (1974).
- 46- C. Baban, G. I. Rusu, and P. Prepelita, Journal of Optoelectronics and Advanced Materials, Vol. 7, No. 2, pp. 817 – 821, (2005).
- 47- J. I. Pankove **"Optical Processes in Semicoductors"**, Prentice – Hall, Inc., Englewoodcliffs, New Jersey (1971).
- 48- J. C. Mainfacier, J. Gasiot and J. P. Fillard, J. Phys. E. Sci. Instrum. **9**, (1989).
- 49- K. L. Chopra **"Thin Film Phenomena"**, McGraw-Hill, Inc., New York, (1969).
- 50- J. I. Pankove **"Optical Processes in Semicoductors"**, Prentice – Hall, Inc., Englewoodcliffs, New Jersey (1971).
- 51- R. A. Grenier **"Semiconductor Device"**, Electronic Energy Series, McGraw-Hill, Book Co. Inc. (1961).
- 52- A. H. Clark **"Polycrystalline and Amorphous Thin Films and Devices"**, Academic Press, New York, (1980).
- 53- L. Fraas, R. Ballantyne, J. Samaras y M. Seal, 1st NREL Conference on TPV Generation of Electricity, AIP Conference Proceedings 321, pp. 44-53 (1994).
- 54- A. Gheorghiu, T. Rappeneau, J.P. DUPIN and M.L. Theye. Journal De Physique, **10**, 42, (1982).
- 55- M. Munoz Urbi, C.E.M de olivera, J.H. Clerice, R.S. Miranda, M.B. Zakia, M.M.G. de Carvalho and N.B. Patel, Electronics Litters, Vol.32,No.3(1996).

- 56- Munoz Urbi, R.S. Miranda, M.B. Zakia, C.F. de Souza, C.A. Ribeiro, J.H. Clerice, and N.B. Patel, *Materials Science and Engineering* **B38**, 259-262(1996).
- 57- Lilik Hasanah, Euis Sustini, Sukirno, Maman Budiman, *Jurnal Matematika dan Sains* Vol. **8** No. 2, hal 107-109 (2003).
- 58- Yingda Dong, Dennis W. Scott, Yun Wei, Arthur C. Gossard, Mark J. Rodwell, *Journal of Crystal Growth*, **256**, pp. 223–229 (2003).
- 59- Z. Y. Liu, D. A. Saulys, and T. F. Kuech, *Appl. Phys. Lett.*, Vol. **85**, No. 19, (8 November 2004).
- 60- Y. N. Guo , J. Zou, Q. Gao, H. H. Tan, and C. Jagadish, *Applied Physics Letters*, **89**, 231917 (2006).
- 61- V. P. Khvostikov, M. G. Rastegaeva, O. A. Khvostikova, S. V. Sorokina, A. V. Malevskaya, *J. of Semiconductors*, Vol. **40**, No. 10, pp. 1242-1246(2006).
- 62- Shenghong Huang “**Microscopy study of Extreme Lattice Mismatched Heteroepitaxy Using Interfacial Misfit Arrays**”, Ph.D. thesis, The University of New Mexico Albuquerque, New Mexico (2007).
- 63- N.A. Sobolev , M.A. Oliveira , R.M. Rubinger, A.J. Neves , M.C. Carmo , V.P. Lesnikov , V.V. Podolskii , Y.A. Danilov , E.S. Demidov, G.N. Kakazei, *J. Supercond. Nov. Magn.* **20**, pp. 399-403(2007).
- 64- I.S. Nerbo, M. Kildemo, S. Leroy, I. Simonsen, E. Sondergard, L. Holt and J.C. Walmsley, *physics optics*, **1**, 1111(2008).
- 65- A. Jallipalli , G. Balakrishnan , S. H. Huang , T. J. Rotter , K. Nunna, B. L. Liang , L. R. Dawson , D. L. Huffaker, *Nanoscale Res. Lett.* **4**, pp. 1458-1462(2009).
- 66- Qiao Zaixiang, Sun Yun, He Weiyu, He Qing, and Li Changjian, *Journal of Semiconductors* Vol. **30**, No. 3 March (2009).
- 67- L. Zheng, S.K. Haywood, N.J. Mason and G. Verschoor, *IEE Proc. Optoelectron.* 147 205-208 (2000).
- 68- A.A. Al-Douri , A.A. Alnajjar , M.F. Alias and F.Y. Al-shakily, *Int. J. Nanoelectronics and Materials* **5**, 67-75 (2012).
- 69- L.G.O. Messias and E. Marega, *Brazilian Journal of physics*, Vol. **32**, no. 2A, June, (2002).

- 70- P. S. Dutta, V. Prasad, and H. L. Bhat, Journal Appl.Phys. **80**, 2847 (1996).
- 71- M.F.A. Alias, E.M. Al-Fawade and S.K. Al-Ani, “ International Journal of Nanoelectronics and Materials”, Vol.4, No.2, 101-114, (2011)
- 72- P. Burrows and S. Forrest, “J. Appl. Phys.”, 79, 10, 7991, (1996).
- 73- M. Farrokh and Sivothman, “J. Vacuum Science and Technology”, Vol. **24**, Issue 3, P. 821, (2006).
- 74- H. Okimura and R. Kondo, “Japan. J. Appl. Phys.”, Vol. **9**, No. 3, P. 274, March, (1970).
- 75- G. Isella and H. Kanel, “Semicond. Sci. Technol.”, Vol.22, P. 526, (2007).
- 76- B. L. Sharma, R. K. Purohit and S.N. Mukerjee, "Infrared Physics", Vol. **10**, PP. 225 – 231, (1970).

إلى 473 كلفن للأغشية $Ga_{0.5}Sb_{0.5}$ ذات السمك 400 نانومتر و كذلك ازدادت من (6.9×10^{-5}) إلى $(8.7 \times 10^{-2}) \Omega \cdot cm$ بزيادة نسبة الكاليوم من 0.4 إلى 0.6 عند درجة حرارة الترسيب للأرضيات 348 K للأغشية Ga_xSb_{1-x} ($x=0.4, 0.5, 0.6$) ذات السمك 400 nm. أوضحت النتائج أن لهذه الأغشية طاقتي تنشيط خلال مدى درجات الحرارة (300-400 K). ازدادت طاقة التنشيط (0.195-0.38 eV) بزيادة درجة حرارة الترسيب للأرضيات (348-473 K) للأغشية $Ga_{0.5}Sb_{0.5}$ ذات السمك 400 nm ولكنها قلت ($0.22-0.12$ eV) كلفن بزيادة نسبة عنصر الكاليوم من 0.4 إلى 0.6 للأغشية Ga_xSb_{1-x} ($x=0.4, 0.5, 0.6$) ذات السمك 200 nm. أظهرت قياسات I-V أن أقطاب الألمنيوم المرسبة على أغشية Ga_xSb_{1-x} ذات توصيل اومي.

تم معرفة نوع وتركيز حاملات الشحنات من خلال قياسات تأثير هول وتم حساب تحركية هول في درجة حرارة الغرفة حيث كانت معظم الأغشية $Ga_{0.4}Sb_{0.6}$ ذات توصيلية من نوع-n بينما كانت معظم الأغشية $Ga_{0.6}Sb_{0.4}$ ذات توصيلية من نوع-p. لوحظ أن تركيز حاملات الشحنات ازداد بزيادة درجة حرارة الأرضيات للأغشية Ga_xSb_{1-x} ذات السمك 200 nm بينما قل للأغشية ذات السمك 400 nm بينما التحركية كانت على عكس ذلك ويعزى ذلك إلى أن العيوب تزداد بزيادة سمك الغشاء.

أظهرت القياسات البصرية للأغشية المركب Ga_xSb_{1-x} بأن الإنتقالات الإلكترونية عبر فجوة الطاقة كانت مباشرة وأن فجوة الطاقة البصرية قد زادت بزيادة درجة حرارة الترسيب بسبب تحسن التركيب و ميله نحو زيادة التبلور بينما قلت فجوة الطاقة بزيادة سمك الأغشية لكل نسب الكاليوم. كذلك قلت مع زيادة سمك الأغشية الذي تؤدي زيادته إلى زيادة العيوب. ودرست الثوابت البصرية وهي معامل الإنكسار ومعامل الخمود وثابت العزل بجزئيه الحقيقي والخيالي كدالة لظروف التحضير من درجة حرارة الترسيب ونسبة الكاليوم والسمك.

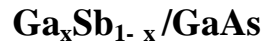
أوضحت خصائص تيار – فولتية للمفرق الهجين $Ga_{0.6}Sb_{0.4}/GaAs$ بأن تيار الظلام الأمامي يتغير تقريباً أسياً مع فولتية الإنحياز. ازدادت الكفاءة بزيادة درجة حرارة الأرضيات (348-473 K) و ازدادت أيضاً بزيادة السمك (200-300 nm) لكنها قلت عند زيادة السمك (300-400 nm) بسبب العيوب التركيبية الناتجة من عدم التطابق الشبكي (Lattice mismatch) لطرفي المفرق.

أظهرت نتائج دراسة خصائص سعة- فولتية للمفرق الهجين $Ga_xSb_{1-x}/GaAs$ عند التردد 1kHz والمحضر عند درجة حرارة 348 كلفن وكان المفرق من النوع الحاد. ازدادت قيم جهد البناء الداخلي V_{bi} بزيادة درجة حرارة الأرضيات T_s ونسب الكاليوم x لكنها قلت بزيادة سمك الأغشية t . قلت قيمة عامل المثالية للمفرق الهجين $Ga_{0.6}Sb_{0.4}/GaAs$ بزيادة سمك الغشاء (200-300 nm) لكنها ازدادت بزيادة السمك (300-400 nm).



جامعة بغداد
كلية العلوم
قسم الفيزياء

الأسم: علي حسين عبد الرزاق جلوخان
عنوان الأطروحة : الخصائص الكهرو بصرية و الميكرو تركيبية للمفرق الهجين



تاريخ المناقشة: 2012/ 11/ 23

اسم المشرف لأول: أ.د. ميسون فيصل أحمد ألياس
التوقيع:

اسم المشرف الثاني: أ.م.د. حسين خزعل رشيد
التوقيع:

الخلاصة

تم تحضير سبيكة ($\text{Ga}_x\text{Sb}_{1-x}$) بمزج أوزان ذرية مناسبة من عنصري Ga و Sb في أنبوبة كوارتز محكمة الغلق بضغط (5×10^{-2} mbar). بعد ان انصهر الخليط تماما بقيت انبوبة الكوارتز لمدة ساعة واحدة وبدرجة حرارة 1173 كلفن مع رجّها بين حين وآخر وذلك لمزج الخليط تماما. تم تحديد نسب مكونات السبيكة باستخدام مطياف تشتت الطاقة (EDXS) وتم التأكد من تركيبها بفحصها بالأشعة السينية (X-ray) وأظهرت تحليلات نماذج الحيود بأن هذه السبيكة ذات تركيب (Zinc blend).

حضرت أغشية ($\text{Ga}_x\text{Sb}_{1-x}$) الرقيقة من السبيكة المحضرة أعلاه بطريقة التبخير الوميضي على أرضيات من الزجاج ورقائق من مركب (GaAs) باتجاهية (111) بمعدل ترسيب (100 nm /min) و بدرجات حرارة ترسيب مختلفة للأرضيات تراوحت بين (348 - 473) كلفن تحت ضغط أكثر من (10^{-5} mbar) و بسمك مختلف يتراوح بين 200 - 400 نانومتر وبنسب مئوية لعنصر الكاليوم (0.4, 0.5, 0.6) و قد أظهر تحليل نماذج حيود الأشعة السينية لهذه الأغشية أنها ذات تركيب (Zinc blend). تم قياس نسب عنصري الكاليوم والأنتيمون للسبيكة وللأغشية الرقيقة باستخدام مطياف تشتت الأشعة (EDXS). تم قياس الحجم الحبيبي و عرض الحدود الحبيبية و كذلك سمك الأغشية بواسطة المجهر الإلكتروني الماسح (SEM) وتبين بأن الحجم الحبيبي يزداد بزيادة درجة حرارة الترسيب للأرضيات وسمك الأغشية وكذلك بزيادة نسب الكاليوم. قلّ عرض الحدود الحبيبية بزيادة درجة حرارة الأرضيات للأغشية $\text{Ga}_{0.4}\text{Sb}_{0.6}$ ذات السمك 200nm بينما ازداد عرض الحدود الحبيبية للأغشية $\text{Ga}_{0.6}\text{Sb}_{0.4}$ ذات السمك 400 nm نانومتر عزي سبب ذلك لزيادة الطور السائل للكاليوم بزيادة نسبته في الخليط.

أظهرت نتائج القياسات الكهربائية أن التوصيلية الكهربائية للتيار المستمر عند درجة حرارة الغرفة تزداد من (1.5×10^{-3}) إلى (5.3×10^{-3}) ($\Omega \cdot \text{cm}$)⁻¹ بزيادة درجة حرارة الترسيب للأرضيات من 348



جمهورية العراق
وزارة التعليم العالي والبحث العلمي
جامعة بغداد
كلية العلوم

الخصائص الكهروبصرية و الميكروتركييبية للمفرق الهجين $Ga_xSb_{1-x}/GaAs$

اطروحة مقدمة إلى

كلية العلوم / جامعة بغداد وهي جزء من متطلبات

نيل درجة دكتوراه فلسفة في الفيزياء

من قبل

علي حسين عبد الرزاق جلوخان
ماجستير علوم في الفيزياء 1991

إشراف

أ.م.د. حسين خزعل رشيد

أ.د. ميسون فيصل أحمد الياس

1433

2012